

UNDERSTANDING PHYSICAL CONDITIONS IN HIGH REDSHIFT GALAXIES THROUGH C I FINE STRUCTURE LINES: DATA AND METHODOLOGY¹

REGINA A. JORGENSEN^{2, 3}, ARTHUR M. WOLFE³, J. XAVIER PROCHASKA⁴

Draft version July 22, 2018

ABSTRACT

We probe the physical conditions in high redshift galaxies, specifically, the Damped Lyman-alpha Systems (DLAs) using neutral carbon (C I) fine structure lines and molecular hydrogen (H₂). We report five new detections of C I and analyze the C I in an additional 2 DLAs with previously published data. We also present one new detection of H₂ in a DLA. We present a new method of analysis that simultaneously constrains *both* the volume density and the temperature of the gas, as opposed to previous studies that a priori assumed a gas temperature. We use only the column density of C I measured in the fine structure states and the assumption of ionization equilibrium in order to constrain the physical conditions in the gas. We present a sample of 11 C I velocity components in 6 DLAs and compare their properties to those derived by the global C II* technique. The resulting median values for this sample are: $\langle n(\text{H I}) \rangle = 69 \text{ cm}^{-3}$, $\langle T \rangle = 50 \text{ K}$, and $\langle \log(P/k) \rangle = 3.86 \text{ cm}^{-3} \text{ K}$, with standard deviations, $\sigma_{n(\text{H I})} = 134 \text{ cm}^{-3}$, $\sigma_T = 52 \text{ K}$, and $\sigma_{\log(P/k)} = 3.68 \text{ cm}^{-3} \text{ K}$. This can be compared with the integrated median values for the same DLAs: $\langle n(\text{H I}) \rangle = 2.8 \text{ cm}^{-3}$, $\langle T \rangle = 139 \text{ K}$, and $\langle \log(P/k) \rangle = 2.57 \text{ cm}^{-3} \text{ K}$, with standard deviations $\sigma_{n(\text{H I})} = 3.0 \text{ cm}^{-3}$, $\sigma_T = 43 \text{ K}$, and $\sigma_{\log(P/k)} = 0.22 \text{ cm}^{-3} \text{ K}$. Interestingly, the pressures measured in these high redshift C I-clouds are similar to those found in the Milky Way. We conclude that the C I gas is tracing a higher-density, higher-pressure region, possibly indicative of post-shock gas or a photodissociation region on the edge of a molecular cloud. We speculate that these clouds may be direct probes of the precursor sites of star formation in normal galaxies at high redshift.

Subject headings: Galaxies: Evolution, Galaxies: Intergalactic Medium, Galaxies: Quasars: Absorption Lines

1. INTRODUCTION

The high redshift neutral gas layers known as the Damped Lyman- α Systems (DLAs) are simultaneously well-understood and mysterious. On the one hand, the large SDSS survey has identified nearly 1,000 DLAs and produced a statistically significant description of the H I column density distribution function, the line density, and the contribution to the neutral gas mass density of the Universe, out to redshifts of $z \sim 4$ (Prochaska et al. 2005; Prochaska & Wolfe 2009). On the other hand, the precise nature of DLAs is still not well understood and basic physical properties such as the volume densities, temperatures, physical sizes, and masses are difficult to constrain due to the nature of their detection as absorption imprints on background quasar spectra.

As the dominant source of neutral gas in the Universe between $z=[0, 5]$, the DLAs represent a key link in the history of galaxy formation, as they likely provide the source of neutral gas to fuel star formation at

high- z (Wolfe, Gawiser, & Prochaska (2003), hereafter WGP03). The purpose of this paper is to constrain the physical conditions in DLAs by taking advantage of a relatively simple three-level system, the neutral carbon (C I) fine structure states.

The ground electronic state of C I, $2s^2 2p^2 \ ^3P_J$, is split into three fine structure levels denoted as 3P_0 , 3P_1 and 3P_2 . Following convention, we will refer to these fine structure states as C I, C I*, and C I**. The excited fine structure states are only 23.6 K and 62.4 K above the ground state, which makes them sensitive probes of conditions in cold gas. The advantage of using the fine structure states of C I is that rather than determining only a line of sight column density, the relative excitation of the C I fine structure states allows for a determination of local physical conditions such as volume density, temperature and pressure.

For almost two decades, the utility of C I fine structure transitions in probing cold gas has been recognized and applied to the high redshift Universe. The C I fine structure levels are populated by collisional excitation and de-excitation, radiative decay, UV pumping and direct excitation by the Cosmic Microwave Background (CMB) radiation. Because of this sensitivity to the CMB, C I fine structure lines in DLAs were first used to determine the temperature of the CMB at high redshifts as a test of Big Bang Cosmology (i.e. Songalia et al. (1994)). However, because the ionization potential (IP) of neutral carbon is below a Rydberg ($\text{IP}_{\text{C I}} = 11.3 \text{ eV} < \text{IP}_{\text{H I}} = 13.6 \text{ eV}$), singly ionized carbon, C II, is the dominant state of carbon in the ISM, and C I is not commonly found in DLAs.

¹ Some of the data presented herein were obtained at the W.M. Keck Observatory, which is operated as a scientific partnership among the California Institute of Technology, the University of California and the National Aeronautics and Space Administration. The Observatory was made possible by the generous financial support of the W.M. Keck Foundation.

² Institute of Astronomy, University of Cambridge, Madingley Road, Cambridge, CB3 0HA, UK; raj@ast.cam.ac.uk

³ Department of Physics, and Center for Astrophysics and Space Sciences, University of California, San Diego, 9500 Gilman Dr., La Jolla, CA 92093-0424

⁴ Department of Astronomy and Astrophysics, UCO/Lick Observatory; University of California, 1156 High Street, Santa Cruz, CA 95064

Additionally, because the CI fine structure transitions are generally weak and suffer significant blending, it is only recently with modern high-resolution echelle spectrographs that detailed measurements of the lines have been possible.

CI has been detected in several high- z DLAs, often as a byproduct of a search for molecular hydrogen (H_2), i.e. Srianand et al. (2005); Noterdaeme et al. (2007b). Because they are photo-ionized and photo-dissociated, respectively, by photons of similar energy, the two species tend to be found together. Previous analyses of CI fine structure states in high- z DLAs have generally assumed a gas temperature in order to calculate the gas volume density and have generally found that for reasonable assumptions of the gas temperature, CI detections require relatively high densities. In this paper, we introduce a technique in which we make no a priori assumptions about the gas temperature.

Inspired by the work of Jenkins & Shaya (1979) and Jenkins & Tripp (2001) who used CI fine structure absorption to probe pressures in the local Milky Way ISM, we implement their technique on high redshift DLAs. Most recently, Jenkins & Tripp (2007) find that most of the CI in the Milky Way is in gas at pressures between $3 < \log(P/k) < 4 \text{ cm}^{-3} \text{ K}$, with the distribution centered at $P/k = 2700 \text{ cm}^{-3} \text{ K}$. We will show that, interestingly, our results for the high redshift DLAs are similar to those of Jenkins & Tripp (2007) for the Milky Way ISM. In addition, by invoking the sensible assumption of ionization equilibrium, we can use the population of the CI fine structure levels to constrain the total radiation field in some cases. This in turn acts as a check on the radiation field as determined by the ‘CII* technique’ (WPG03; WGP03) – a way of measuring the radiation field due to star formation in a DLA by equating the cooling rate measured via the CII* fine structure transition with the heating rate.

This is the first in a series of two papers focused on deriving the physical conditions in DLAs via the analysis of CI fine structure lines. In this first paper, we report the detection of CI in five high redshift DLAs, and analyze an additional 2 DLAs with previously published CI data. We derive limits on density, temperature, and pressure as well as the radiation field contained in the CI-bearing gas of each DLA. In the systems for which we have coverage of H_2 , we compare the CI fine structure results to those derived by an analysis of the H_2 rotational J level populations. In the second paper of this series we will extend our analysis to the CI-bearing DLAs already published in the literature, analyze the broader physical implications of the CI data and finally, propose a physical picture of CI-bearing DLAs.

This paper is organized as follows: We discuss our data and data analysis techniques in § 2. We present our procedure for analyzing the CI data through the specific example of DLA 0812+32 at $z_{\text{abs}} = 2.626$ in § 3. We then summarize the results for each of the CI-bearing DLAs in § 4. § 5 contains discussion of the DLAs presented here and we conclude in § 6. Throughout this paper we make the standard assumption that the ratio of column density of element X is equal to the ratio of volume density, $\frac{N(X^a)}{N(X^b)} = \frac{n(X^a)}{n(X^b)}$, i.e. we are analyzing average conditions along the line of sight.

2. DATA AND METHODOLOGY

The CI sample presented here represent serendipitous discoveries made during the course of an on-going campaign to obtain high resolution spectra of DLA targets for detailed study. Data for this paper was taken primarily with the HIRES spectrograph (Vogt et al. 1994) on the Keck I telescope, with a typical decker that resulted in an instrumental resolution $\text{FWHM} = 6.25 \text{ km s}^{-1}$. Details of specific observations are given in Table 1. Data were reduced and continuum fit using the standard XIDL⁵ packages. Because of the complex blending of many close fine structure transitions that typically exhibit several velocity components, we were not able to successfully apply the apparent optical depth technique (Savage & Sembach 1991) for a measurement of the column densities. We also did not have the high signal to noise ratio and resolution of the Jenkins & Tripp (2001) study of interstellar CI, in which they developed a modified AODM technique (Jenkins & Tripp 2001). Instead we used the VPFIT package, version 9.5⁶ to measure the CI fine structure column densities, $N(\text{CI})$, $N(\text{CI}^*)$, and $N(\text{CI}^{**})$, redshifts, and Doppler parameters (b), where $b = \sqrt{2}\sigma$, and σ is the velocity dispersion in km s^{-1} . Wavelengths and f-values were taken from Morton (2003)⁷.

In general, we simultaneously fit as many CI multiplets as possible. In all cases, we included all multiplets that fell redward of the $\text{Ly}\alpha$ forest, which generally included the strongest multiplets at 1656\AA and 1560\AA , and usually the multiplet at 1328\AA . In cases where a multiplet fell within the Lyman α forest, yet did not contain any obvious blending with a forest line, we included that multiplet in our analysis. We rejected sections of spectra that contained obvious blending.

To determine upper limits for non-detected fine structure states, generally for $N(\text{CI}^{**})$, we used VPFIT, which allows for an estimation of the 1σ upper limit by inputting a “reasonable guess” of the column density and re-running the fit to give linear errors. The error is then taken as the 1σ upper limit. For a conservative reasonable guess we used the measured column density of the line with the smallest measured column density, usually $N(\text{CI}^*)$, since it is almost always the case that $N(\text{CI}^{**}) < N(\text{CI}^*)$. This results in a conservative upper limit to the $N(\text{CI}^{**})$ value.

We present one new detection of H_2 in DLA 2340–00, and we analyze the H_2 in DLA 0812+32. While it is likely that the other systems contain measurable H_2 as well, we lack the spectral coverage to confirm this speculation.

All other information about each DLA, including metallicity, dust-to-gas ratio, and $\log N(\text{C II})$ was determined using the Apparent Optical Depth Method, AODM (Savage & Sembach 1991), unless otherwise stated (i.e. in the cases where we performed a full com-

⁵ <http://www.ucolick.org/~xavier/IDL/>

⁶ <http://www.ast.cam.ac.uk/~rfc/vpfit.html>

⁷ Note, however, that there is some confusion over the correct f-values for the CI transitions given a more recent set determined by E. B. Jenkins (2006, private communication). Since we cannot determine which set of f-values is more correct, in this paper we use the Morton (2003) values to be consistent with what has previously been used in the literature.

ponent by component analysis). To measure the $\log \frac{CII}{CI}$ we must employ the conventional method of measuring $N(CII)$ by proxy using $N(Si II)$, because the C II $\lambda 1334$ transition is saturated in every DLA presented in this paper. As in Wolfe et al. (2004) we let $[C/H]^8 = [Si/H] + [Fe/Si]_{int}$ where $[Fe/Si]_{int} = -0.2$ for a minimal depletion model or $[Fe/Si]_{int} = 0.0$ for a maximal depletion model. While Wolfe et al. (2004) estimate the error in the measurement of $\frac{CII}{CI}$ to be 0.1 dex, we use the more conservative estimate of 0.2 dex.

Details of the observations are given in Table 1, while the details of the CI measurements are summarized in Table 2. In the following we provide a brief summary of the data analysis of each DLA in our sample:

• **DLA 0812 + 32, $z_{abs} = 2.62633$** : DLA 0812+32 at $z_{abs} = 2.62633$ has been studied extensively (see Prochaska et al. (2003)), and boasts one of the highest known DLA metallicities and H I column densities. Prochaska et al. (2003) used the many available transitions to show that the relative elemental abundance pattern is similar to that of the Milky Way. Jorgenson et al. (2009) presented the first direct evidence of cold ($T_{thermal} \leq 78$ K, (115 K, 2σ)) gas at high redshift using a curve of growth analysis of a sub-resolution, narrow velocity CI component in this DLA, and recently, Tumlinson et al. (2010) presented the detection of HD.

In this work we simultaneously fit data from three Keck HIRES runs with details given in Table 1. Eight multiplets were used to fit the CI fine structure lines; $\lambda 1656$, $\lambda 1560$, $\lambda 1328$, $\lambda 1280$, $\lambda 1279$, $\lambda 1277$, $\lambda 1276$, and $\lambda 1270$. The $\lambda 1276 - \lambda 1280$ multiplets were blended with a C IV doublet at $z_{abs} = 1.992$. Figure 1 contains the spectral data of DLA 0812+32, in black, overlaid with our fit, in red, and the CI fine structure lines marked. Each velocity component is denoted by a different linestyle (solid, dashed, dotted, etc.) while each fine structure state is denoted by a different color (CI= red, CI*= green, CI**= blue). It is apparent from this figure that 1) in some cases the CI fine structure transitions fall so close to each other that they are blended, and 2) the multi-component velocity structure found in most DLAs further complicates the analysis. As denoted in Figure 1, three CI velocity components are required to fit this DLA. Component 1 at $z_{abs} = 2.625808$, or $v \sim -43$ km s⁻¹, with Doppler parameter of $b = 3.25$ km s⁻¹, is the weakest component and contains the largest errors. Component 2 at $z_{abs} = 2.6263247$ with $b = 2.57$ km s⁻¹, is located at $v = 0$ km s⁻¹, and has an upper limit on $N(CI^{**})$. Component 3 at $v \sim +14$ km s⁻¹, or $z_{abs} = 2.626491$, is the narrow component reported in Jorgenson et al. (2009) with $b = 0.33$ km s⁻¹.

While the velocity structure of CI in DLA 0812+32 is well constrained by the fitting of many multiplets, our confidence in the fit is increased by the similar velocity structure seen in neutral chlorine, CII $\lambda 1347$. Because of their similar ionization potentials, both below a Rydberg, CI and CII $\lambda 1347$ are often observed to have the same velocity structure (Jura 1974a). This is seen in Figure 2 along with several other sub-Rydberg and low-ion transitions that trace the velocity structure of CI, namely, Ge II $\lambda 1237$, Mg I $\lambda 1827$, Si I $\lambda 1845$ and Zn II

$\lambda 2062$.

This DLA also contains relatively strong H₂, with a total $\log N(H_2) = 19.90$ cm⁻², giving a molecular fraction of $f = 0.067$, where f is defined as $f = \frac{2N(H_2)}{N(HI)+2N(H_2)}$. The H₂ velocity components are consistent with those of CI.

• **DLA 0812 + 32, $z_{abs} = 2.066780$** : Data for this DLA is the same as that for DLA 0812+32, $z_{abs} = 2.62633$ discussed above. There is one CI velocity component in this DLA. To fit CI, we used only the $\lambda 1656$ and $\lambda 1560$ multiplets because of heavy blending with the Lyman α forest blueward of restframe $\sim \lambda 1467$ Å, see Figure 3. This DLA also contains CII, however it is interesting to note that the centroid of the CII profile is displaced by $\approx +5$ km s⁻¹ with respect to $v = 0$ km s⁻¹ at the CI centroid of $z_{abs} = 2.066780$. While this is unexpected, it is also true of all of the low-ions, see Figure 4. However, Si I and Mg I appear to align more closely with CI.

• **DLA 1331 + 17**: Wolfe & Davis (1979) discovered 21 cm absorption towards QSO1331+17 at $z_{abs} = 1.77642$, a similar redshift at which a DLA had previously been discovered at optical wavelengths (Carswell et al. 1975). They deduced a spin temperature of $T_s \approx 770 - 980$ K by combining the 21 cm line equivalent width with the $N(H I)$ obtained from Lyman α absorption.

One of the first attempts to measure the CMB temperature at high redshift using CI was made by Meyer et al. (1986) using DLA 1331+17. They measured CI and put an upper limit on the ratio $n(CI^*)/n(CI)$ that allowed them put an upper limit on the temperature of the CMB, $T_{CMB} < 16$ K at $z_{abs} = 1.776$. Later, Songalia et al. (1994) used the Keck telescope to make more precise measurements. They succeeded in measuring the CI* transition and derived a CMB temperature of $T = 7.4$ K that agreed well with the theoretical prediction. More recently, Cui et al. (2005) discovered an unusually high level of molecular hydrogen (H₂) in DLA 1331+17 using Hubble Space Telescope. They detect a molecular fraction of $5.6\% \pm 0.7\%$ in a component at $z_{abs} = 1.776553$. They derive an excitation temperature of the H₂- bearing component of $T_{ex} = 152$ K. Recently Carswell et al. (2010) discovered a narrow velocity component of CI at $z_{abs} = 1.776525$, that requires gas with $T_{thermal} \leq 218$ K (1σ).

To maximize the UV coverage for DLA 1331+17, we used a Keck HIRES spectrum with instrumental resolution FWHM = 6.25 km s⁻¹ in combination with a bluer UVES spectrum of resolution FWHM = 7.0 km s⁻¹ kindly provided by R. F. Carswell. This provided coverage of the maximum number of CI multiplets, down to the restframe CI $\lambda 1277$ multiplet at observed wavelength $\lambda_{obs} \approx 3546$ Å. We included in the fit the following multiplets: $\lambda 1656$, $\lambda 1560$, $\lambda 1328$, $\lambda 1280$, and $\lambda 1277$.

As shown in Figure 5, DLA 1331+17 requires three CI velocity components. Component 1, at $v \sim 0$ km s⁻¹, is the strongest component in terms of column density (see Table 2) with $b = 5.08 \pm 0.24$ km s⁻¹. Component 2, at $v \sim 17$ km s⁻¹, has a narrow velocity structure ($b = 0.55 \pm 0.13$ km s⁻¹), and is discussed in detail in Carswell et al. (2010). The third component, at $v \sim 20$ km s⁻¹, with $b = 24.45 \pm 6.2$ km s⁻¹, does not exhibit measurable CI* or CI** absorption. Lending con-

⁸ The abundance ratio with respect to solar is defined as $[X/Y] = \log(X/Y) - \log(X/Y)_\odot$

fidence to the fit is the presence of ClI, shown in Figure 6 along with several other sub-Rydberg and low-ion transitions that trace the velocity structure of CI, namely, P II $\lambda 1152$, S II $\lambda 1250$, Mn II $\lambda 2576$, and Mg I $\lambda 2852$.

We can compare our results to another recent measurement of CI absorption in this system. Dessauges-Zavadsky et al. (2004) used VLT and Keck data to measure CI in two components, $\log N(\text{CI}) = 13.12 \pm 0.02 \text{ cm}^{-2}$ at $z_{abs} = 1.776365$ and $\log N(\text{CI}) = 12.72 \pm 0.02 \text{ cm}^{-2}$ at $z_{abs} = 1.776523$. While in the latter case, what we call component 2, their measurements agree with ours to within 1σ errors, the component 1 is in disagreement, with small errors, by 0.12 dex. However this difference is reasonable considering continuum placement uncertainties and the fact that they did not include fitting of the CI fine structure states which involve considerable blending with the resonance line.

•**DLA 1755 + 578** : DLA 1755+578, at $z_{abs} = 1.9692$, contains 8 CI components, making it one of the more complex CI systems. It is interesting in its own right because we have discovered the presence of Si II* absorption in this DLA. While Si II* has been observed in GRB-DLAs pumped by the UV radiation field of the GRB afterglow (Savaglio & Fall 2004; Prochaska et al. 2006), this is the first known case of Si II* observed in a high redshift QSO-DLA. Because Si II* is generally thought to arise in warm gas – its excitation energy is 413K – this system is not only unique but also extremely interesting since it appears that several velocity components contain *both* CI and Si II* absorption, indicating that this is one of the rare DLAs exhibiting both CNM *and* WNM gas at high- z . We discuss this object in greater detail in a future paper.

•**DLA 2100 – 06** : While this DLA, at $z_{abs} = 3.09237$, exhibits measurable CI, our data are not of sufficiently high quality to obtain good measurements of the CI fine structure states. This is in part because the CI lines are not strong, and in part because the strongest multiplet, $\lambda 1656$, falls close to an order gap and as a result is contained in a lower signal to noise region.

All CI multiplets $\lambda 1277$ and redwards are included in the fit. The fit requires three CI velocity components, only one of which has measurable $N(\text{CI}^{**})$, albeit with large enough errors that it might best be considered as an upper limit. We present spectral coverage of the multiplets used in Figure 7.

•**DLA 2231 – 00** : DLA 2231–00 at $z_{abs} = 2.066$ was analyzed by Prochaska & Wolfe (1999), who reported the detection of titanium, and Prochaska (1999) analyzed a Lyman-limit system at $z_{abs}=2.652$ in this sightline. With an absorption redshift of $z_{abs} = 2.066$ in the line of sight to a quasar with emission redshift of $z_{em} = 3.02$, both the $\lambda 1328$ and the $\lambda 1560$ CI multiplets of this DLA fall in the Lyman- α forest. While most of the $\lambda 1560$ multiplet is unblended, the $\lambda 1328$ multiplet contains a blend with a large Lyman-alpha forest line. Our analysis includes only the $\lambda 1656$ and $\lambda 1560$ multiplets, which are shown in Figure 8. The best fit required two CI velocity components: component 1 at $v = -77 \text{ km s}^{-1}$, or $z_{abs} = 2.06534$, with no measurable fine structure lines, and component 2 at $v = 0 \text{ km s}^{-1}$, or $z_{abs} = 2.066122$, with detected CI fine structure lines. These two CI components trace the two strongest components of the other

low ions, as seen in Figure 9. While ClI is located in a region of low S/N, the detection of Mg I $\lambda 2026$ lends confidence to the CI detection. We note that while the large error of the $N(\text{CI}^{**})$ measurement of component 2 indicates that it should probably be considered an upper limit, for the purposes of the present analysis we will treat the value as a detection.

•**DLA 2340 – 00, $z_{abs} = 2.054924$** : The complex multi-component nature of the CI in this $z_{abs} = 2.054924$ DLA made it difficult to fit despite the fact that seven CI multiplets ($\lambda 1270$, $\lambda 1276$, $\lambda 1277$, $\lambda 1279$, $\lambda 1328$, $\lambda 1560$ and $\lambda 1656$) have been included in the fit. The $\lambda 1279$ multiplet was only partially used due to blending with interlopers. Nine CI components were required in the fit, see Figure 10. The components are labeled 1 – 9 and located at the following velocities relative to an arbitrarily chosen $z_{abs} = 2.054151$ for $v = 0 \text{ km s}^{-1}$: $v \sim 13 \text{ km s}^{-1}$, 37 km s^{-1} , 44 km s^{-1} , 52 km s^{-1} , 55 km s^{-1} , 57 km s^{-1} , 83 km s^{-1} , and 96 km s^{-1} .

DLA 2340–00 also contains a relatively high total column density of molecular hydrogen, $\log N(\text{H}_2) = 18.20 \text{ cm}^{-2}$, giving an H_2 fraction $f = 0.014$, making it one of the few relatively H_2 - rich DLAs.

•**ABSL 2340 – 00, $z_{abs} = 1.36$** : The sightline towards J2340–00 contains a second set of CI absorption lines that require 4 CI velocity components to fit. Only the $\lambda 1656$ and $\lambda 1560$ CI multiplets were available to constrain the fit because of the low redshift. Because of blending, in the case of $\lambda 1656$ multiplet with the CI $\lambda 1279/\lambda 1280$ multiplet of the high- z absorber, and in the case of $\lambda 1560$ multiplet with the Lyman α forest, the CI lines were fit by tying them to their associated Mg I transitions. The results are given in Table 2.

3. APPLYING THE CI FINE STRUCTURE TECHNIQUE

In this section we detail the processes by which we determined the constraints on the physical conditions in each DLA.

3.1. The Steady State Equation

We developed an in-house code based on POPRATIO (Silva & Viegas 2001) to calculate the theoretical CI fine structure level populations by making the standard assumption of steady state. Following Silva & Viegas (2001) we considered spontaneous radiative decay, direct excitation by the CMB, UV pumping, and collisional excitation and de-excitation. As in POPRATIO, the rate equations leading to steady state populations of state i is given by

$$\sum_j n_j (A_{ji} + B_{ji}u_{ji} + \Gamma_{ji} + \sum_k n^k q_{ji}^k) = n_i \sum_j (A_{ij} + B_{ij}u_{ij} + \Gamma_{ij} + \sum_k n^k q_{ij}^k) \quad (1)$$

where A_{ij} are the spontaneous decay transition probabilities, B_{ij} are the Einstein coefficients, u_{ij} is the spectral energy density of the radiation field, Γ_{ij} is the indirect excitation rate due to fluorescence and is defined by Silva & Viegas (2001). The quantity n^k is the volume density of the collision partner k , where $k = (\text{H}^0, n_e, n_p)$ and $q_{ij}^k = \langle \sigma v \rangle$, is the collision rate coefficient. The reverse rates are calculated using the assumption of detailed balance. All coefficients were taken to be the

same as those used in POPRATIO, with the exception of collisions with neutral hydrogen, for which we used the more recent rate coefficients calculated using the analytical formula by Abrahamsson et al. (2007) extended to the temperature range of $T = 10,000$ K. For the sake of simplicity, we did not consider excitation by collisions with either molecular hydrogen (H_2) or helium (He I). In the case of the former, the paucity of H_2 found in DLAs, at typical fractions of less than $\approx 10^{-5}$ renders the effect of collisions with H_2 so small as to be negligible. However, even in DLAs in which the H_2 fraction is relatively large (for DLA 1331+17, the molecular fraction was determined by Cui et al. (2005) to be $f = 0.056$ or $5.6\% \pm 0.7\%$), H_2 does not have a large effect on the collisional excitation of CI.⁹ In the latter case of He I, collision rates are significantly lower than those of other partners. Additionally, the density of He I compared with that of H I is typically $n(\text{He I}) = 0.0975 n(\text{H I})$ (Anders & Grevesse 1989), making collisions with He I relatively unimportant.

Direct excitation by the CMB is calculated assuming the standard cosmology and a CMB temperature of $T = T_0(1+z)$ where $T_0 = 2.725$ K (Mather et al. 1999). At high redshift, the CMB radiation generally has the strongest effect on the CI fine structure level populations because of the small temperature difference between the ground and first fine structure states. However, depending on the physical circumstances, other mechanisms such as UV pumping or collisions can dominate.

We included UV pumping due to a radiation field consisting of two components that we will call J_ν^{Bkd} , and J_ν^{local} , and let $J_\nu^{total} = J_\nu^{local} + J_\nu^{Bkd}$. J_ν^{Bkd} is the background radiation due to the integrated contribution from high z galaxies and quasars, known as the Haardt-Madau background (Haardt & Madau (1996); and more recently using CUBA¹⁰). In all cases, the minimum value of the total radiation field is determined by J_ν^{Bkd} . In each case the value of J_ν^{Bkd} is calculated based on the redshift of the DLA, and these values are summarized in Table 4. For an explanation of these values, see Figure 1 of Wolfe et al. (2004). Because each CI-bearing DLA also contains strong C II* $\lambda 1335.7$ absorption, we used the C II* technique (see WPG03 and Wolfe et al. (2004)) to estimate the local radiation field due to star formation, $J_\nu^{local, C II^*}$, and included this contribution in the UV pumping. The $J_\nu^{local, C II^*}$ is calculated at $\lambda = 1500\text{\AA}$, or 8.27 eV, and in § 5.1.2 we explain the estimated error on this value, $\sim \pm 50\%$. Note that in general, $J_\nu^{local, C II^*} = J_\nu^{local}$. We introduce the notation $J_\nu^{local, C II^*}$ to specify how the local radiation field is measured, i.e. in this case it is the local star formation rate per unit area measured via the C II* technique.

To quantitatively determine the effects of the radiation field on the CI fine structure level populations, we plot

⁹ I.e. the rate of excitation due to collisions with neutral hydrogen at $T = 100$ K is $n^{HI} q_{01}^{HI} = 2.976 \times 10^{-10} n(\text{H I}) \text{ s}^{-1}$, where we use the conventional notation of representing CI, CI*, CI** by the indices 0, 1, 2 respectively. If we take the fraction of H_2 to be 5.6% of H I, the rate for collisions with H_2 is $n^{H_2} q_{01}^{H_2} = 6.7 \times 10^{-11} (0.056) n(\text{H I}) = 3.75 \times 10^{-12} n(\text{H I}) \text{ s}^{-1}$, which is roughly two orders of magnitude smaller than q_{01}^{HI} .

¹⁰ CUBA (Haardt & Madau, 2003) is available at: <http://pitto.mib.infn.it/~haardt/cosmology.html>

the $\frac{n(CI^*)}{n(CI)}$ and $\frac{n(CI^{**})}{n(CI)}$ versus neutral hydrogen density for excitation by a wide range of radiation fields in Figure 11. In this example we have considered collisions with neutral hydrogen at $T = 100$ K, spontaneous radiative decay, and the excitation by the CMB at $z = 2$, in addition to a radiation field of varying strengths as denoted in Figure 11. At low density, excitation by the CMB is dominant, unless the input UV radiation field is strong, in which case, the UV dominates. At higher densities, i.e. $n(\text{H I}) > 10 \text{ cm}^{-3}$, collisional excitation becomes important and finally at $n(\text{H I}) \gtrsim 1000 \text{ cm}^{-3}$ the levels thermalize. In other words, at low densities the CMB sets the floor of $\frac{n(CI^*)}{n(CI)}$. Only when the radiation field exceeds a total strength of approximately $J_\nu^{total} \gtrsim 10^{-18.5} \text{ ergs cm}^{-2} \text{ s}^{-1} \text{ Hz}^{-1} \text{ sr}^{-1}$, does $\frac{n(CI^*)}{n(CI)}$ begin to significantly exceed that caused by the CMB alone. Since J_ν^{Bkd} rarely exceeds $10^{-19} \text{ ergs cm}^{-2} \text{ s}^{-1} \text{ Hz}^{-1} \text{ sr}^{-1}$, the Haardt-Madau background alone at a redshift of $z \sim 2$, has essentially no effect on the CI fine structure excitation.

3.2. Steady State Solution

The steady state densities in each of the CI fine structure states are found by solving three homogeneous equations with three unknowns. To solve the three homogeneous equations, we solve for the ratio of each excited state relative to the ground state. We denote all terms involving CMB excitation, UV pumping and collisions by the shorthand, $R_{ij} = B_{ij} u_{ij} + \Gamma_{ij} + \sum_k n^k q_{ij}^k$ which is summed over the k different collision partners, where all terms were defined in the previous subsection. Reverse reaction rates are calculated through the principle of detailed balance. Following Jenkins & Tripp (2001) (see their equations 10 and 11), we find:

$$\frac{n(CI^*)}{n(CI)} = \frac{(R_{0,1})(A_{2,1} + A_{2,0} + R_{2,1} + R_{2,0}) + (R_{0,2})(A_{2,1} + R_{2,1})}{(R_{1,2})(A_{2,0} + R_{2,0}) + (A_{1,0} + R_{1,0})(A_{2,1} + A_{2,0} + R_{2,1} + R_{2,0})} \quad (2)$$

and

$$\frac{n(CI^{**})}{n(CI)} = \frac{(R_{0,2})(A_{2,0} + R_{1,0} + R_{1,2}) + (R_{0,1})(R_{1,2})}{(R_{1,2})(A_{2,0} + R_{2,0}) + (A_{1,0} + R_{1,0})(A_{2,1} + A_{2,0} + R_{2,1} + R_{2,0})} \quad (3)$$

where the states CI, CI*, CI** are denoted by the indices 0, 1, 2 respectively. The resulting theoretical solutions are functions of the density of neutral hydrogen, $n(\text{H I})$, and the temperature. Following Jenkins & Shaya (1979) we define,

$$f1 \equiv \frac{n(CI^*)}{n(CI)_{tot}} = \frac{\frac{n(CI^*)}{n(CI)}}{1.0 + \frac{n(CI^*)}{n(CI)} + \frac{n(CI^{**})}{n(CI)}} \quad (4)$$

and

$$f2 \equiv \frac{n(CI^{**})}{n(CI)_{tot}} = \frac{\frac{n(CI^{**})}{n(CI)}}{1.0 + \frac{n(CI^*)}{n(CI)} + \frac{n(CI^{**})}{n(CI)}} \quad (5)$$

where $n(CI)_{tot} = n(CI) + n(CI^*) + n(CI^{**})$. We give the values of $(f1, f2)$ for each component of each DLA in

Table 2.

In Figure 12 we plot the theoretical solutions in the (f1, f2) plane for the example case of component 3 of DLA 0812+32. In this case, J_ν^{total, CII^*} as derived from the CII* technique, is $J_\nu^{total, CII^*} = 7.4 \times 10^{-19}$ ergs cm⁻² s⁻¹ Hz⁻¹ sr⁻¹. The solutions follow tracks, one for each temperature from T = 10 K – 10,000 K increasing in steps of 0.1 dex. Along each track, n(H I) increases from 10^{-3.5} cm⁻³ to 10^{4.1} cm⁻³ in steps of 0.02 dex, each density being represented by an individual point. We chose the ranges of temperatures and densities to ensure that we had broad coverage of the entire plane of possible solutions. While the CI data may allow higher T values, these would imply a primarily ionized gas which is highly unlikely for this material. The data point at (f1, f2) \approx (0.31, 0.09) is determined by our curve of growth analysis (in the case of the resonance line CI) and VPFIT fits to the data for component 3 (see Table 2). 1 σ (2 σ) errors are determined by calculating the values of f1 and f2 using the upper and lower allowed values as determined by the 1 σ (2 σ) error bars for each column density measurement. The resulting red (blue) polygon defines a region of space in the f1 versus f2 plane that contains the acceptable 1 σ (2 σ) solutions. In Figure 13 we plot the predicted theoretical solutions that fall within the 1 σ (in red) and 2 σ (in blue) error polygons of the data, on a graph of density versus temperature. These are the allowed density and temperature combinations derived from the CI data under the assumption of a single phase absorber.

3.3. Ionization Equilibrium

To further constrain the CI solutions we introduce the assumption of ionization equilibrium and utilize the measured $\frac{CII}{CI}$ ratio, which we assume is equal to $\frac{n(CII)}{n(CI)} = \frac{N(CII)}{N(CI)}$. Ionization equilibrium is a reasonable assumption because the densities in these clouds are generally relatively high, thereby ensuring that the recombination times are shorter than the typical dynamical timescales. In basic form, ionization equilibrium can be written: $n_e n(X^+) \alpha = n(X) \Gamma$, where α is the case A recombination coefficient of element X⁺ to X and Γ represents the ionization rate. From this equation we get, $\frac{n(CII)}{n(CI)} = \frac{\Gamma}{n_e \alpha}$, i.e. the ratio $\frac{CII}{CI}$ is a function of Γ (where Γ is proportional to the radiation intensity), n_e , the electron density, and α , which is a function of temperature. Therefore, for a given radiation field and temperature, we determine $\frac{CII}{CI}$ for a range of possible electron densities, n_e (Details of the ionization equilibrium are given in WPG03, and we discuss the sensitivity to the radiation field in section 3.3.1). We then use the measured $\frac{CII}{CI}$ of each DLA to constrain our allowed solutions. While we measure N(CI) directly, we must employ the conventional method of measuring N(CII) by proxy using N(Si II), because the available CII λ 1334 transition is saturated in all the DLAs considered here. We generally measure the Si II or S II and Fe II using the standard AODM, which is well suited for cases such as these in which we have more than one transition of an ion. As in Wolfe et al. (2004) we let $[C/H] = [Si/H] + [Fe/Si]_{int}$ where the intrinsic (nucleosynthetic) ratio $[Fe/Si]_{int} = -0.2$ for a minimal

depletion model or $[Fe/Si]_{int} = 0.0$ for a maximal depletion model. We follow Murphy & Liske (2004) and adopt the minimal depletion model in this work, and analyze the implications of the minimal versus maximal depletion model in section 5.1.1. While Wolfe et al. (2004) estimate the error in the measurement of $\frac{CII}{CI}$ to be 0.1 dex, we use the more conservative estimate of 0.2 dex. We also note that, assuming there is no hidden saturation of metals, this is the maximum N(CII) that could be associated with the CI gas, and we discuss the implications of this assumption further in section 5.1.3.

To demonstrate the constraints imposed by ionization equilibrium, in Figure 14 we plot the CI solutions in terms of n(H I) versus $\log(\frac{CII}{CI})$ for the example case of component 3 in DLA 0812+32. The measured $\log(\frac{CII}{CI}) = 3.10$ is indicated by the red dashed line with a range of ± 0.2 dex indicated by green dashed lines. It is obvious that the region of allowed CI fine structure solutions is further constrained by invoking ionization equilibrium. For clarification, in Figure 15 we re-plot the density versus temperature diagram, however now we denote the final solutions, those constrained by the $\frac{CII}{CI}$ ratio, in black (1 σ) and yellow (2 σ). As a result, invoking ionization equilibrium results in even tighter constraints on the densities and temperatures of the CI-bearing cloud without making any assumptions about the gas temperature. In this example case we constrain the density to be $72 \lesssim n(H I) \lesssim 549$ cm⁻³ while the temperature is constrained to be $25 K \lesssim T \lesssim 251 K$, and the pressure $3.54 \lesssim \log(P/k) \lesssim 4.80$ cm⁻³ K. χ^2 minimization finds the best-fitting solution: $n(H I) = 100$ cm⁻³, $T = 79$ K, and $\log(P/k) = 3.90$ cm⁻³ K.

3.3.1. Using Ionization Equilibrium to Constrain the Radiation Field

Until now we have assumed the UV radiation field due to star formation, J_ν^{local} , is determined by the CII* technique. We will now relax this constraint and allow the input local radiation field to vary, repeat the above analysis for each case, and examine the results as a function of radiation field. We show that for some CI-bearing clouds we can place upper and lower limits on the allowed radiation field utilizing only the CI fine structure data and the assumption of ionization equilibrium.

We use a grid of J_ν^{local} values from $J_\nu^{local} \approx 10^{-21} - 10^{-16}$ ergs cm⁻² s⁻¹ Hz⁻¹ sr⁻¹. To differentiate these radiation fields from those predicted by the CII* technique, we will call them $J_\nu^{local, CI}$. For each $J_\nu^{local, CI}$ we first add the J_ν^{Bkd} to obtain a $J_\nu^{total, CI}$, and then rerun the above analysis, calculating the f1 versus f2 tracks for each $J_\nu^{total, CI}$, followed by the ionization equilibrium analysis.

In Figure 16 we plot the 1 σ CI results for the example case of DLA 1331+17 on a graph of $\frac{CII}{CI}$ versus n(H I) where for clarity we show only a sub-sample of the entire $J_\nu^{total, CI}$ grid results. Solutions corresponding to each $J_\nu^{total, CI}$ are represented by different colors. Again, we use the $\frac{CII}{CI}$ data to constrain the allowed solutions, and it is apparent that for $J_\nu^{total, CI} \gtrsim 1 \times 10^{-19}$ ergs cm⁻² s⁻¹ Hz⁻¹ sr⁻¹, there are no acceptable solutions. This limit on $J_\nu^{total, CI}$ is actually quite strict considering that the Haardt-Madau background is only ~ 1 order of mag-

nitude lower than this value.

This technique places an upper limit on the local radiation field, and hence the star formation rate, using only CI fine structure absorption and the assumption of ionization equilibrium, without invoking any assumptions about star formation from the CII* technique. We note in this example, of DLA 1331+17, component 3, that the strength of the radiation field as determined by the CII* technique ($J_\nu^{total, CII^*} = 3.3 \times 10^{-19}$ ergs cm $^{-2}$ s $^{-1}$ Hz $^{-1}$ sr $^{-1}$) is just slightly higher than the 1σ upper limit derived independently from the CI data. However, in the case of DLA 1331+17, the CII* transition is likely blended with a Lyman- α forest line, forcing us to estimate the true N(CII*) by assuming it traces the velocity structure of other low ions and fitting it together with the forest line as explained in section 4.3.

A byproduct of this analysis places limits on the density, temperature and pressure of the cloud. In this example case of DLA 1331+17, at the 1σ level the density is limited to the range, $11 \lesssim n(\text{H I}) \lesssim 44$ cm $^{-3}$ while the temperature is constrained to be $79 \lesssim T \lesssim 794$ K, and the pressure $3.50 \lesssim \log(P/k) \lesssim 4.04$ cm $^{-3}$ K. Again, we stress that these limits are derived independently of the results of the CII* technique, using *only* the CI fine structure data and the assumption of ionization equilibrium for a range of possible radiation fields.

4. RESULTS

A summary of the details of each DLA are presented in the following tables: Table 2: a summary of the CI data, Table 3: a summary of general DLA information, Table 4: the resultant radiation fields derived from the CII* technique, and in Table 5: the final CI fine structure solutions giving allowed ranges of densities, temperatures and pressures. Finally, in Table 6, we give the results of lifting the CII* constraint on the local radiation field.

We now briefly describe the results for each CI-bearing DLA. The casual reader may wish to skip directly to the more general discussion of the results in § 5.

4.1. FJ0812+32, $z_{abs} = 2.62633$

This DLA contains three distinct CI velocity components whose CI fine structure levels we will analyse individually. In measuring the metallicity, N(C II) and N(CII*) we will take two approaches; The first, discussed here, and the second, the individual component analysis, discussed in section 4.1.1. Heavy blending of line profiles and the uncertainty/degeneracy of line profile fitting techniques have led to the customary use of the AODM technique to measure the amount of metals over the entire, blended DLA profile. Additionally, this avoids any question about the distribution of the N(H I), which by definition is damped and therefore kinematically unknowable. Because we are measuring the metals over the entire (blended) DLA, we refer to these measurements as 'global', and we apply them to each CI component, which we consider reasonable given that the low-ions such as S II and Si II track the velocity components of CI, see Figure 2.

We measure $\log N(\text{CII}^*) = 14.30 \pm 0.01$ cm $^{-2}$ which along with the CII* technique determines that the radiation due to stars $J_\nu^{local, CII^*} = 7.17 \times 10^{-19}$ ergs cm $^{-2}$

s $^{-1}$ Hz $^{-1}$ sr $^{-1}$. Adding in the contribution from the background, $J_\nu^{Bkd} = 2.45 \times 10^{-20}$ ergs cm $^{-2}$ s $^{-1}$ Hz $^{-1}$ sr $^{-1}$, gives $J_\nu^{total, CII^*} \sim 7.4 \times 10^{-19}$ ergs cm $^{-2}$ s $^{-1}$ Hz $^{-1}$ sr $^{-1}$. The excitation rates due to the local star formation alone are $\Gamma_{01} = 3.17 \times 10^{-9}$ s $^{-1}$, $\Gamma_{02} = 2.40 \times 10^{-9}$ s $^{-1}$, and $\Gamma_{12} = 3.12 \times 10^{-9}$ s $^{-1}$. These can be compared with those of the Haardt-Madau background at the redshift of this DLA that produces excitation rates $\Gamma_{01} = 1.09 \times 10^{-10}$ s $^{-1}$, $\Gamma_{02} = 8.23 \times 10^{-11}$ s $^{-1}$, $\Gamma_{12} = 1.07 \times 10^{-10}$ s $^{-1}$. We used the total radiation field and the assumption of ionization equilibrium to determine solutions for the three CI components that are labeled 0812+32 $_{global}$ in Table 5. We are unable to perform an analysis of component 2 given that the upper limit of $N(\text{CI}^{**}) \leq 12.39$ cm $^{-2}$ is relatively large, resulting in a (f1, f2) combination with no limitation on n and T.

We can use the constraints on the volume density to estimate the physical size of the cloud. Using the neutral hydrogen column density $\log N(\text{H I}) = 21.35$ cm $^{-2}$ and, for example, the best-fit volume density for component 3, $n(\text{H I}) \approx 100$ cm $^{-3}$, we can estimate the size of the CI-bearing cloud to be $\ell = N(\text{H I})/n(\text{H I}) \approx 2.24 \times 10^{19}$ cm, or ≈ 7 pc. This estimation is technically an upper limit to the size of the cloud that assumes that all of the H I is associated with the CI component.

When we relax the constraint of J_ν^{total, CII^*} as derived from N(CII*), as discussed in the previous section, at the 2σ level we constrain the density to $n \geq 0.1$ cm $^{-3}$ and $n \geq 7$ cm $^{-3}$ for components 1 and 3 respectively. In both cases we place a not-so-strict upper limit on the allowed radiation field of $J_\nu^{total} \leq 773 \times 10^{-19}$ ergs cm $^{-2}$ s $^{-1}$ Hz $^{-1}$ sr $^{-1}$.

4.1.1. DLA 0812+32: Individual Component Analysis

While the initial modeling was completed using the radiation field and metallicity as measured over the entire profile, it is clear upon careful inspection of the spectrum (see Figure 2 and Figure 7 of Jorgenson et al. (2009)), that the depletion, and hence, dust-to-gas ratio, is not constant over the three components. This motivates our attempt to analyze each velocity component individually. Specifically, component 3, the narrow component, contains obvious Zn II, CII* and CI, while it exhibits no evidence for Cr II. A natural explanation is that Cr II is heavily depleted onto dust grains in component 3. However, as discussed in Jorgenson et al. (2009), blending precludes a straightforward measurement of the equivalent width, and profile fitting using VPFIT, produces a Zn II column density in component 3 that is unrealistically high and ruled out by an upper limit on N(O I) assuming solar relative abundances. We explain this by assuming the presence of another weak, broad component (for details see Jorgenson et al. (2009)), and model the log N(Zn II) in component 3.

Because Zn II and Cr II are not saturated and appear to trace the velocity structure of CI quite well, we use these ions to determine the metal distribution, the dust-to-gas ratio, and the N(C II) in each component separately. To do this we first tie the redshifts and b values of each ion together and then use VPFIT to determine the column densities in each component. It is expected that Zn II and Cr II be tied together because

they are metal-line transitions arising in singly ionized species with similar ionization potentials, and thus are likely to show the same physical/velocity structure. However, they will not necessarily exactly trace the CI, given that CI is affected by the incident J_ν^{total} and n_e , and if there is a gradient in J_ν^{total} or n_e , this could cause a difference between the structure of CI and the other low ions. We give the results of this fitting in Table 7. In light of the work of Jorgenson et al. (2009) we include an additional broad weak component, in order to achieve a realistic N(Zn II) in component 3.

Due to the nature of damped lines, we cannot use Lyman- α to determine the distribution of the neutral hydrogen among these components. Therefore, we assume that the N(H I) traces the low-ion metals, in this case Zn II, and that the neutral hydrogen is distributed proportionally to the metals. This results in each component having the same metallicity, $[Zn/H] = -0.58$. We note, that in theory, this metallicity should be the same as that determined for the global case, $[Zn/H] = -0.81$. However, the individual component analysis reveals the presence of the narrow component 3, for which we have estimated the N(Zn II) based upon an upper limit on N(O I). While the exact metallicity of this component remains a mystery without higher resolution data, it is apparent that component 3 lacks significant Cr II, indicating a high level of depletion, and consequently a higher dust-to-gas ratio than components 1 and 2. Following WPG03 (their equation 7) we define the dust-to-gas ratio relative to the Milky Way as follows,

$$\kappa = 10^{[Zn/H]_{int}} (10^{[Cr/Zn]_{int}} - 10^{[Cr/Zn]_{gas}}), \quad (6)$$

where "gas" is the abundance ratio in the gas phase and "int" is the intrinsic nucleosynthetic abundance. We calculate the dust-to-gas ratio in component 3 to be $\sim 17\%$ of the Milky Way ($\log \kappa = -0.78$). For comparison, Prochaska et al. (2003) measure $\kappa \sim 6\%$ ($\log \kappa = -1.24$) over the entire profile of this DLA, and the typical dust-to-gas ratio in DLAs is $\sim 1/30$ solar. We summarize information about each component in Table 7.

As we might expect, given that the column densities of all low ions with the exception of Cr II, but including C II*, are much higher in component 3 (due to the fixed small Doppler parameter), the $J_\nu^{local, C II^*}$ of component 3 deduced from the C II* technique is more than 1 order of magnitude larger than that determined for components 1 and 2. The results of the CI models for each component are presented in Table 5 where they are denoted by the subscript 'div'. Note that the radiation field for component 3 predicted by the C II* technique is quite large, at 260×10^{-19} ergs $\text{cm}^{-2} \text{s}^{-1} \text{Hz}^{-1} \text{sr}^{-1}$. The solutions require low temperatures ($T \leq 32$ K) and densities in excess of 10^3 cm^{-3} , which imply an upper limit on the cloud size of $\ell \leq 0.1$ pc. This small size may be in conflict with the evidence against partial covering provided by the H₂, see section 4.1.2. It is possible that we have over-estimated the amount of N(C II*) associated with the narrow component 3, and that more of the N(C II*) is associated with the broader component 4, but we would require a higher resolution spectrum to confirm this scenario.

Relaxing the constraint of J_ν^{local} determined by the

C II* technique, gives no limits on temperature, and a large range of allowed densities for component 1 ($n(\text{H I}) = 0.002 - 4166 \text{ cm}^{-3}$), with a lower limit of $n(\text{H I}) \geq 6 \text{ cm}^{-3}$ for component 3. Constraints on the allowed radiation fields are consistent with that determined by the C II* technique.

4.1.2. DLA 0812+32 Molecular Hydrogen

This DLA also shows evidence of relatively strong molecular hydrogen (H₂), see Figure 17. As shown in Jorgenson et al. (2009), there is no evidence for partial coverage, as the H₂ lines are black at line center. We used VPFIT to fit the H₂, which required three components whose redshifts roughly agree with those of the three CI components. While the Doppler parameters do not agree with those of the CI— they are roughly similar to or smaller, whereas we would expect them to be larger by a factor of $(6)^{1/2}$ — we will refer to these H₂ components as components 1, 2, and 3, and assume that they are co-spatial with the CI components. This is not the first report of such differences in the b -values between H₂ and CI components in DLAs (Noterdaeme et al. 2007a,b). Because of the close match in redshift space and the likelihood that CI and H₂ are co-spatial, we fixed the well-determined Doppler parameter of component 3 to that of the CI ($b^{CI} = 0.33 \text{ km s}^{-1}$), scaled by the relative atomic weights as done in Jorgenson et al. (2009)¹¹. We list the parameters of the H₂ fits in Table 8.

It is interesting to note that like the CI, the majority of the H₂ resides in component 3, the narrow velocity component. The fraction of H₂ in component 3, $f \geq 0.06$, or $\geq 6\%$, with the upper limit representing the uncertainty in N(H I) distribution, is among the highest found in DLAs. While we have tied the Doppler parameter to that of the CI, we note that because of heavy saturation of the $J = 0$ and $J = 1$ lines in this component, $\log N$ is determined by the damping wings of the profile and is therefore insensitive to the choice of b . We have verified this by artificially fixing the Doppler parameter to a range of values from $b = 0.2 - 6 \text{ km s}^{-1}$ as well as by raising the continuum by 5%. None of these tests change the resultant N(H₂, $J=0$) and N(H₂, $J=1$) by more than ~ 0.03 dex. While the $J = 0$ and $J = 1$ lines are completely insensitive to the Doppler parameter, the higher level J states are sensitive to the choice of Doppler parameter. Therefore, we also report a model in which we have allowed the Doppler parameter of component 3 to be determined by the $J = 3$ state and we report the results, called model 2, in Table 8.

We can estimate the kinetic temperature of the clouds using the column densities of H₂ in the $J=0$ and $J=1$ rotational states and assuming the states are thermalized according to the Boltzmann distribution (see equation 8 in Levshakov et al. (2002)). The excitation temperature, T_{ex} , is defined by,

$$\frac{N(J)}{N(0)} = \frac{g(J)}{g(0)} \exp\left[-\frac{B_v J(J+1)}{T_{ex}}\right] \quad (7)$$

where $B_v = 85.36$ K for the vibrational ground state and $g(J)$ is the degeneracy of level J . In Figure 18 we show

¹¹ $b^{H_2} = (6)^{1/2} b^{CI} = 0.81 \text{ km s}^{-1}$.

the standard H₂ excitation diagram, log(N/g) versus energy, for the J=0 to J=5 levels for each component. As explained in Appendix 1 (on molecular hydrogen), the kinetic temperature of the gas is proportional to the negative inverse of the slope determined by the J=0 and J=1 levels, assuming that the levels are thermalized (a good assumption given the densities of these clouds), i.e. T_{ex} equals the kinetic temperature. For components 1, 2, and 3 we determine the following temperatures, $T_{ex}^{01} = 102$ K, $T_{ex}^{01} = 73$ K, $T_{ex}^{01} = 47$ K, respectively. These are consistent with the temperatures derived from the CI data, which leads us to believe there is good correspondence between the CI and H₂ data and that the gas probed here is a CNM. Also, the $T_{ex}^{01} = 47$ K derived for the narrow component 3 is consistent with the upper limit on the thermal temperature of $T_{thermal} \leq 78$ K required by the curve of growth determined Doppler parameter.

We can also use the H₂ data to determine the ambient/incident radiation (UV flux) field on the cloud, J_{ν}^{total, H_2} , using the J=0 and J=4 states (see Appendix 1 for details). The level populations above J = 1 are unlikely to be thermalized since their larger Einstein A coefficients implies that these states are depopulated by spontaneous emission more rapidly than by collisional de-excitation; this rules out the condition of detailed balance required to establish thermal equilibrium. Instead, these states are likely to be populated by UV pumping, which is what we shall assume. Following Hirashita & Ferrara (2005) we call this radiation field J_{ν}^{LW} , as determined by absorption in the Lyman-Werner H₂ bands. Since the H₂ measurement should reflect the total incident radiation field, $J_{\nu}^{local} + J_{\nu}^{Bkd} = J_{\nu}^{LW} = J_{\nu}^{total, H_2}$. Results for the photoabsorption rate, β , and for the shielding terms, both self-shielding by H₂ and shielding due to dust, are given in Table 7. Note that β_0 is derived from the J = 4 population, while β_1 is derived from the J = 5 population. Using the J = 4 population, we obtained the following radiation fields for components 1, 2, and 3 respectively: $J_{\nu}^{total, H_2} = < 3.7 \times 10^{-20}, 1.7 \times 10^{-20}, 3.6 \times 10^{-20}$ ergs cm⁻² s⁻¹ Hz⁻¹ sr⁻¹. Note, that for component 1, N(H₂, J = 4) is an upper limit, and hence, this is technically an upper limit on the radiation field. Also notice that these radiation fields are only slightly larger, or smaller in the case of component 2, than J_{ν}^{Bkd} . This places a rather strict limit on additional radiation from local star formation.

Interestingly, the radiation field as calculated from the H₂ is rather independent of the choice of global versus individual component parameters. In the above we gave the results of the individual component analysis, where we assumed that the N(H I) tracks the metals, in this case the N(Zn II), and used the individual component metallicity, N(H I) and dust-to-gas ratio to calculate the radiation field. If we instead use the 'global' model, the N(H I) increases to the global value, here log N(H I) = 21.35 cm⁻², while κ decreases in each component to the global value, here $\kappa = 0.07$. These two effects essentially cancel each other out in the calculation of shielding (see equation 20 in Appendix A) and we obtain very similar radiation fields in each case (i.e. for component 1, $J_{\nu}^{total, H_2, global} < 4.2 \times 10^{-20}$ ergs cm⁻² s⁻¹ Hz⁻¹ sr⁻¹, compared with $J_{\nu}^{total, H_2, indiv} < 3.7 \times 10^{-20}$ ergs cm⁻² s⁻¹ Hz⁻¹ sr⁻¹).

We do not understand why the radiation field derived from the H₂ data is ≈ 20 times smaller than that derived by the C II* technique, $J_{\nu}^{total} = 7.4 \times 10^{-19}$ ergs cm⁻² s⁻¹ Hz⁻¹ sr⁻¹. Additionally, the radiation field predicted by the H₂ levels for component 2 is low enough that it is excluded by the CI data and the Haardt-Madau background (however, we note that the difference is not large and it could be within the errors – i.e. for component 2, if we consider the errors on the J = 0 and J = 4 levels we derive $J_{\nu}^{total, H_2} = 3.1 \times 10^{-20}$ ergs cm⁻² s⁻¹ Hz⁻¹ sr⁻¹, consistent with the Haardt-Madau background, but still ≈ 20 times smaller than the C II* prediction). This conflict could potentially be resolved if either 1) we are underestimating the population in the N(H₂, J=4) level – which could be caused by hidden saturation of narrow components as was demonstrated for the narrow component in DLA 1331+17 (Carswell et al. 2010), where the N(H₂, J = 4) is likely underestimated because of the presence of the small Doppler component which contains the majority of the molecular gas (see further discussion in section 4.3 and Carswell et al. (2010)), or 2) the C II* prediction is overestimating the radiation field. In the latter case, the radiation field is dependent upon the assumption of the equilibrium pressure existing at the geometric mean (see Section 5.1.1 for details). If instead the equilibrium pressure is located at P_{max} or P_{min} , the resultant radiation field can change by up to a factor of 10 (for example, see Table 12). In the former case, we estimate that if the radiation field as predicted by the C II* technique is accurate and the H₂ feels this entire radiation field, we require the amount of H₂ in the J=4 level to increase by a factor of 20, to N(H₂, J=4) ~ 15.3 cm⁻². This large amount of H₂ is ruled out by the data unless it exists in a very narrow component with $b \lesssim 0.2$ km s⁻¹.

We also derive densities from the H₂ data (see Appendix 1), assuming the temperature is equal to the kinetic temperature derived from the J = 0 and J = 1 states. The resultant densities, n(H I) = 21, 11, and 37 cm⁻³ for components 1, 2, and 3 respectively, are nearly consistent with the CI results (where for components 1 and 3 we derived n(H I) = 23 - 417 cm⁻³ and 72 - 549 cm⁻³, respectively). Again, since the radiation fields were not consistent and they are involved in this calculation, we may expect some of the discrepancy. We note however, that the densities are consistent with the lower limits derived from the CI data alone (n(H I) ≥ 0.1 and ≥ 7 cm⁻³ respectively).

Additionally, we can use the J = 2 rotational state to place an upper limit on the density if the excitation temperature, T_{ex}^{02} is not equal to that of T_{ex}^{01} , indicating that the J = 2 state is not thermalized, and that the density is below n_{crit} , the critical density needed for thermalization. We plot critical density as a function of temperature for the H₂ J states in Figure 19. In component 1 of DLA0812+32, $T_{ex}^{02} = 132$ K is greater than $T_{01} = 102$ K, indicating that the density must be less than n_{crit} . In this case we derive a upper limit on the density of component 1 of $n \lesssim 200$ cm⁻³, consistent with the derived densities for this component. In component 3, $T_{ex}^{02} = 57$ K is greater than $T_{01} = 47$ K, also indicating an upper limit on the density of component 3 of $n \lesssim 700$ cm⁻³. For component 2, T_{02} is slightly less than

T_{01} – indicating either that it is thermalized, or that this is within the errors. In either case, the upper limit derived from the next higher state, T_{03} , would not be that restrictive as $n_{crit} \sim 10^3 \text{ cm}^{-3}$.

4.2. *FJ0812+32*, $z_{abs} = 2.066780$

The C II* transition of this DLA falls in the Ly α forest, and because the profile is quite different from that of the other low low ions (see Figure 4), it is difficult to make a definitive estimate of the true C II* column density. Instead, we attempt to estimate the star formation rate by assuming three models motivated by the bimodality of DLA cooling rates (Wolfe et al. 2008). In the first case, case (a), we assume this is a ‘low cool’ DLA and use the average low-cool $\ell_c = 10^{-27.4} \text{ ergs s}^{-1} \text{ H}^{-1}$. This assumption is likely the closest to the truth given that several physical traits of this DLA match those of the low-cool population of DLAs, i.e. the small value of the low-ion velocity, $\Delta v = 26 \text{ km s}^{-1}$ is more likely to be drawn from the low-cool sample, with median $\Delta v = 46 \text{ km s}^{-1}$, than from the high cool sample with median $\Delta v = 104 \text{ km s}^{-1}$. The Si II 1526 rest-frame equivalent width is also small at, $W_{1526} = 0.22 \pm 0.01 \text{ \AA}$, compared with the low-cool median $W_{1526} = 0.26 \pm 0.09 \text{ \AA}$, while the metallicity, $[\text{M}/\text{H}] = -1.38 \pm 0.01$, is slightly higher than the median metallicity for the low-cool population $[\text{M}/\text{H}] = -1.74 \pm 0.19$. This discrepancy in metallicity may simply be the result of metallicity increasing with decreasing redshift, as the $z_{abs} = 2.06$ of this DLA is lower than the median $z_{abs} = 2.85$ of the ℓ_c sample (Wolfe et al. 2008). Finally, the dust-to-gas ratio $\log_{10}\kappa = -2.74$ is similar to the median low-cool dust-to-gas ratio, $\log_{10}\kappa = -2.57 \pm 0.17$. In the second case, case (b), we will again make the low cool assumption, but instead of the standard α -enhancement assumption of $[\text{Fe}/\text{Si}] = -0.2$, we will assume $[\text{Fe}/\text{Si}] = 0.0$. Finally, in the last model, case (c), we will assume that the DLA is a ‘high cool’ DLA and has an ℓ_c equal to the median high cool DLA $\ell_c = 10^{-26.6} \text{ ergs s}^{-1} \text{ H}^{-1}$.

We present the results for the three cases in Table 5. It is clear from the resultant densities that either cases (a) or (b) are more likely to be correct. In case (c), there are no acceptable 1σ solutions, and the range of densities at the 2σ level ($n(\text{H I}) > 3800 \text{ cm}^{-3}$) seems unphysical. Densities this high are unlikely to be observed because they imply a very small cloud size that would be unlikely to cover the background quasar, i.e. here, the cloud size is estimated as $\ell \lesssim N(\text{H I})/n(\text{H I}) \lesssim 10^{21.5}/3800 = 8.3 \times 10^{17} \text{ cm} \lesssim 0.3 \text{ pc}$.

Following our assumption that the minimal depletion model is more likely to be correct, we conclude that case (a) is the best physical approximation for this system. If we now relax the constraint imposed by the C II* technique, and model a range of possible $J_\nu^{total, CI}$, we find that at the 2σ level, we can restrict the density to $n \geq 32 \text{ cm cm}^{-3}$, $T \leq 1585 \text{ K}$ and $J_\nu^{total} = 0.41 - 195 \times 10^{-19} \text{ ergs cm}^{-2} \text{ s}^{-1} \text{ Hz}^{-1} \text{ sr}^{-1}$, see Table 6.

4.3. *DLA 1331+17*

Here we discuss the analysis of component 1, at $z_{abs} = 1.77636$, the only component with all three CI fine structure lines detected. The Haardt-Madau background at

the redshift of this DLA is given by $J_\nu^{Bkd} = 2.53 \times 10^{-20} \text{ ergs cm}^{-2} \text{ s}^{-1} \text{ Hz}^{-1} \text{ sr}^{-1}$. To estimate the local stellar contribution to the UV field we utilized the C II* technique. While WPG03 report $\log N(\text{C II}^*) = 14.05 \pm 0.05 \text{ cm}^{-2}$ for this object, the C II* transition is likely blended with a Ly α forest line because its velocity profile is very different from that of the low ions, see Figure 6. Generally, the C II* velocity profile traces that of low ions such as Si II $\lambda 1808$. Therefore, we cannot exclude the possibility that the C II* transition is blended with a forest line, and we take the WPG03 value of $\log N(\text{C II}^*) = 14.05 \pm 0.05 \text{ cm}^{-2}$ as an upper limit. To obtain an estimate of the actual $N(\text{C II}^*)$, assuming that it is blended, we (Carswell 2007; private communication) fixed the shape of the velocity profile to that of Si II $\lambda 1808$ and normalized the C II* contribution by fitting the profile simultaneously with a coincident Ly α line. Summing over the C II* components results in an estimate of the true $N(\text{C II}^*)$ of $\log N(\text{C II}^*) \lesssim 13.56 \text{ cm}^{-2}$. With this value of C II* absorption, the C II* technique results in a star formation rate that produces a radiation field of $J_\nu^{local, C II^*} \approx 3.1 \times 10^{-19} \text{ ergs cm}^{-2} \text{ s}^{-1} \text{ Hz}^{-1} \text{ sr}^{-1}$. Therefore, the total input radiation field, that is, $J_\nu^{Bkd} + J_\nu^{local, C II^*}$, is $J_\nu^{total, C II^*} \approx 3.3 \times 10^{-19} \text{ ergs cm}^{-2} \text{ s}^{-1} \text{ Hz}^{-1} \text{ sr}^{-1}$. Finally, the CI fine structure data constrained by ionization equilibrium, gives 2σ results of $16 \lesssim T \lesssim 32 \text{ K}$, $91 \lesssim n(\text{H I}) \lesssim 363 \text{ cm}^{-3}$, and $3.36 \text{ cm}^{-3} \text{ K} \lesssim \log(P/k) \lesssim 3.86 \text{ cm}^{-3} \text{ K}$.

We can compare our results to those of Cui et al. (2005), who used CLOUDY to derive a best fit model to their H₂ data that resulted in a hydrogen number density $n(\text{H I}) \approx 0.2 \text{ cm}^{-3}$ and $T \approx 140 \text{ K}$ for the H₂ bearing cloud at $z_{abs} = 1.776553$. This cloud is clearly not in pressure equilibrium with the CI cloud of our analysis, component 1 at $z_{abs} = 1.77637$, i.e. while the temperature is somewhat higher, the density is more than two orders of magnitude lower, resulting in pressures of $P/k \approx 28 \text{ cm}^{-3} \text{ K}$ for the H₂ -bearing cloud. The CI -bearing cloud more closely resembles the CI -bearing clouds in the local ISM as found by Jenkins & Tripp (2007) and Jenkins & Tripp (2001). We discuss these similarities further in section 5.3.

Cui et al. (2005) determine a photoabsorption rate based on the population of H₂ in the J = 0 and J = 4 states, the latter of which is optically thin and therefore measures the intensity of radiation outside the cloud. Solving for this radiation field they derive $J_\nu(\lambda = 1000 \text{ \AA}) \approx 2.1 \times 10^{-3} J_{\nu, \odot}(\lambda = 1000 \text{ \AA})$, where $J_{\nu, \odot}(\lambda = 1000 \text{ \AA})$ is the UV intensity in the solar neighborhood at 1000 \AA and is, according to their paper, equal to $J_{\nu, \odot}(\lambda = 1000 \text{ \AA}) \approx 3.2 \times 10^{-20} \text{ ergs cm}^{-2} \text{ s}^{-1} \text{ Hz}^{-1} \text{ sr}^{-1}$. They do recognize that the radiation field as determined by the H₂ J states is ~ 3 orders of magnitude weaker than that determined by the C II* technique and comment that this is a discrepancy. More importantly however, this radiation field is ~ 3 orders of magnitude below the Haardt-Madau background, which sets a lower limit to the radiation field. It is difficult to understand at first why the molecular hydrogen excitation is not consistent with this minimum radiation field. A solution exists however, if the bulk of the H₂ gas resides in the narrow CI velocity component, i.e. component 2, and hence, has

been missed because of the effects of hidden saturation. Carswell et al. (2010) have completed an analysis of this narrow component and include a detailed interpretation of the H₂ data that is consistent with both the Haardt-Madau background and the local stellar field derived by CII*.

When we relax the constraint on the radiation field as determined by the CII* technique and allow the field to vary, as already discussed in section 3.3.1, we can constrain the radiation field to $J_\nu^{total,CI} \lesssim 1 \times 10^{-19}$ ergs cm⁻² s⁻¹ Hz⁻¹ sr⁻¹ (1σ). This limit on $J_\nu^{total,CI}$ is actually quite strong considering that the Haardt-Madau background is only ~ 1 order of magnitude lower than this value. Note that the lower limit on the allowed $J_\nu^{total,CI}$ is fixed by J_ν^{Bkd} . It is apparent from Figure 16 that the density is limited to the range, $11 \lesssim n(\text{H I}) \lesssim 44$ cm⁻³ while the temperature is constrained to be $79 \text{ K} \lesssim T \lesssim 794 \text{ K}$, and the pressure $3.5 \lesssim \log(P/k) \lesssim 4.04$ cm⁻³ K. We stress that these limits are derived independent of the results of the CII* technique, using *only* the CI fine structure data and the assumption of ionization equilibrium for a range of possible radiation fields. The 2σ results provide the less restrictive results $J_\nu^{total} \lesssim 8.6 \times 10^{-18}$ ergs cm⁻² s⁻¹ Hz⁻¹ sr⁻¹, $n(\text{H I}) \gtrsim 10$ cm⁻³, and $T \lesssim 794 \text{ K}$.

4.4. J2100–00

While insufficiently good quality data hinder a full analysis of DLA 2100–00, we attempted an analysis of component 1, by treating the upper limit on N(CI**) as a detection. The measured N(CII*) produces a $J_\nu^{local,CII^*} = 17 \times 10^{-19}$ ergs cm⁻² s⁻¹ Hz⁻¹ sr⁻¹, also an upper limit. The relatively large errors on the fine structure column densities do not produce very restrictive results. However, the VPFIT derived Doppler parameter of this component, $b = 0.2 \pm 0.3$ km s⁻¹, if real, places a strict upper limit on gas temperature of $T_{thermal} \lesssim 29 \text{ K}$, which is consistent with the results from the CI fine structure analysis. Unfortunately, the weakness of the CI line coupled with the low S/N of the data, makes a curve of growth analysis inconclusive. For the purposes of this paper however, it is the CI column densities that are important, and while they typically depend on the choice of Doppler parameter, we can obtain a sort of lower limit to the column density by fixing a relatively large Doppler parameter, i.e. $b = 7$ km s⁻¹. We measure $N(\text{CI}) = 12.12$ cm⁻², which is well-within the errors quoted in Table 2, and see that in this case, the CI column densities have little dependence on changes in b .

4.5. Q2231–00

While there are two CI components contained in the DLA at $z_{abs} \sim 2.066$, here we will focus only on component 2, which possess measurable CI fine structure lines. While not formally an upper limit, the detection of N(CI**) is relatively weak and has large error. For the purpose of this analysis we will treat this value as a detection.

We estimate the J_ν^{local,CII^*} from the measured N(CII*) with some confidence, even though it falls within the Lyman- α forest, because the velocity profile of CII* closely traces that of other low ions as expected. Using

this $J_\nu^{local,CII^*} \approx 24.7 \times 10^{-19}$ ergs cm⁻² s⁻¹ Hz⁻¹ sr⁻¹, we find $199 \text{ cm}^{-3} \lesssim n \lesssim 1513 \text{ cm}^{-3}$, and $13 \lesssim T \lesssim 25 \text{ K}$, see Table 5. Relaxing the constraint of J_ν^{local,CII^*} given by the CII* technique results in a lower limit on the density of $n(\text{H I}) \gtrsim 3 \text{ cm}^{-3}$ (2σ).

4.6. J2340–00

DLA 2340–00 is a relatively complex system requiring nine CI velocity components. Given the strong blending of transitions and the resultant uncertainty on upper limits, we do not analyze those components for which N(CI**) is not detected, namely, components 1 and 7. In addition, the column densities of component 6 have extremely large errors, making analysis pointless, as well as the unphysical condition of $N(\text{CI}^*) > N(\text{CI})$.

This DLA contains a relatively high total column density of molecular hydrogen, $\log N(\text{H}_2) = 18.20$ cm⁻², or $f = 0.014$. The neutral hydrogen column density, at $\log N(\text{H I}) = 20.35 \pm 0.15$ cm⁻², is close to the threshold defining a DLA ($\log N(\text{H I}) = 20.30$ cm⁻²), which supports the findings of Noterdaeme et al. (2008) that the probability of detecting H₂ does not strongly depend on N(H I). Furthermore, the low-ion velocity profile is large, with $\Delta v = 104$ km s⁻¹, and the cooling rate, as determined by CII* over the entire profile, at $\log \ell_c = -26.15$ ergs s⁻¹ H⁻¹, is among the highest of DLAs. Because of the complex nature of the CI, the H₂, and the low-ion profiles, all requiring multiple components, and because of heavy blending and saturation in some components of the low-ions, we were not able to obtain unique fits to all low ion components using VPFIT. Instead, we analyzed the CI data using two different model assumptions.

In the first case, we assume J_ν^{total} just slightly above the background, $J_\nu^{total} = 3.9 \times 10^{-20}$ ergs cm⁻² s⁻¹ Hz⁻¹ sr⁻¹. Because this is a lower limit to the radiation field, this analysis provides an upper limit on density (i.e. for all else being constant, if we increase the radiation field, the density required to collisionally excite the CI fine structure levels is decreased). The metallicity, dust-to-gas ratio and $\log \frac{CII}{CI}$ are determined by AODM over the entire profile with measured results given in Table 3. The densities and temperatures derived from the CI fine structure data are given in Table 5.

In an attempt to refine the model, in the second case, we used the AODM over three 'super-components' of the CII*, S II, Fe II, and other low-ion and resonance line transitions. The choice of super-components was motivated by visual inspection of the spectra that reveal three large velocity components separated in velocity space (albeit with each component containing smaller substructure). We arbitrarily chose $v = 0$ km s⁻¹ at $z_{abs} = 2.054151$, and defined the AODM super-components as follows: super-component (a) from $v = -30$ to 15 km s⁻¹, super-component (b) from $v = 15$ to 70 km s⁻¹, and super-component (c) from $v = 70$ to 120 km s⁻¹, see Figure 20. Super-components a, b, and c coincide with CI components (1, 2), (3, 4, 5, 6, 7) and (8, 9) respectively. We then applied the metallicity, dust-to-gas ratio, and N(CII*) measurement derived from the AODM 'super-component' to each associated CI component. Table 9 contains a summary of this analysis. Looking at each super-component, we find the following:

- *Super – component (a)*: We did not perform the

CII* analysis on super-component (a) because we measure a super-solar [Fe/S] and [Ni/S]. The absence of depletion detected for Fe and Ni implies that we cannot calculate the dust-to-gas ratio. If real, this super-solar (or nearly solar) value of Fe II would require a different and special star formation history. Given that we cannot calculate a dust-to-gas ratio or $J_{\nu}^{local,CII*}$, and the fact that the CI components 1 and 2 associated with super-component (a) contain the smallest amount CI, we did not perform further analysis.

•*Super – component (b)*: Super-component (b), which includes CI components 3, 4, 5, 6 and 7, contains the bulk of the gas. The CII* technique results in $J_{\nu}^{total,CII*} = 5.27 \times 10^{-18}$ ergs cm⁻² s⁻¹ Hz⁻¹ sr⁻¹. The combination of the large J_{ν}^{total} and the low $\frac{CII}{CI}$ are not compatible with the measurements of CI fine structure in components 3, 4, or 5 (6 and 7 are ruled out by upper limits).

•*Super – component (c)*: The CII* technique applied to super-component (c), which covers CI components 8 and 9, results in a $J_{\nu}^{total} = 1.1 \times 10^{-18}$ ergs cm⁻² s⁻¹ Hz⁻¹ sr⁻¹. A reasonable range of results for components 8 and 9 are summarized in Table 5.

If we relax the constraint of $J_{\nu}^{total,CII*}$ as measured by the CII* technique, we can determine limits for each component for a range of possible radiation fields. Results are given in Table 6. In all cases we can put a lower limit on the density of $n > 7$ cm⁻³. In all components except for component 2, the temperature can be constrained to be $T \lesssim 800$ K and the $J_{\nu}^{total,CI} \leq 27 \times 10^{-19}$ ergs cm⁻² s⁻¹ Hz⁻¹ sr⁻¹, is 2 orders of magnitude larger than the Haardt-Madau background and consistent with the J_{ν}^{total} derived by the CII* technique.

4.6.1. On the possible ionization of DLA 2340–00

Given the potential presence of Fe III $\lambda 1122$ and the fact that the column density of DLA 2340–00, at $\log N(\text{H I}) = 20.35$ cm⁻², is just above the DLA threshold of 2×10^{20} cm⁻², we considered the possibility of partial ionization of the gas. We used the AODM technique to measure Fe III/Fe II in the same three 'super-components' discussed above, covering CI components 1 and 2, components 3, 4, 5, 6 and 7 and components 8 and 9 respectively, see Figure 20. Because the Fe III profile does not trace that of the low ions (see Figure 20), we cannot rule out the possibility of blending with the Lyman α forest and therefore, we treat our Fe III measurements as upper limits that ultimately give no information about possible ionization.

Instead, we can rule out a high ionization factor based on the [Ar/S] measurement. Specifically, Prochaska et al. (2002) state that photoionization models in which $[\text{Ar I} / \text{S II}] > -0.2$ dex require that $x < 0.1$, in other words, require gas that is $> 90\%$ neutral. Using the Ar I $\lambda\lambda$ 1048, 1066 transitions, excluding blending in the super-component 3 of the $\lambda 1066$ transition (see Figure 20), we find $[\text{Ar/S}] > -0.2$ in all components (see Table 9), indicating that $x < 0.1$ and that the gas is $> 90\%$ neutral.

4.6.2. Molecular Hydrogen in DLA 2340–00

The total column density of molecular hydrogen, $\log N(\text{H}_2) = 18.20$ cm⁻², where $f = 0.014$, is large rel-

ative to most H₂ -bearing DLAs, where f is typically $f \sim 10^{-5}$. We have analyzed the H₂ using VPFIT. To allow for the best fit we have let the H₂ component redshifts and b values vary independently of the CI and low-ion components. We find that we require 6 H₂ components to achieve the best fit. In redshift space, these components lie remarkably close to the CI components 1, 2, 4, 6, 8 and 9, ($\Delta v = +1.4, +0.6, -2.8, +0.3, -0.4, +0.4$ km s⁻¹, respectively) and therefore we use this notation to refer to the H₂ components. Details of the H₂ measurements are given in Table 10 and example spectra in Figure 21. In Figure 22 we plot the excitation diagrams for each H₂ component and list the excitation temperature as determined by the J=0 and J=1 states. Additionally, we use the population of the J=4 state to determine the radiation field as described in Appendix 3. Details are given in Table 11.

While the radiation fields derived from the H₂ data are in general consistent with the CI constraints, it is interesting to note that the densities derived from the H₂ data alone, see Appendix 1 for details, while consistent with the CI limits, tend to be significantly higher than that required for CI. We summarize results for each component for which we could make comparisons between the different techniques:

•*Components 1& 2*: Excitation temperatures are in good agreement with constraints placed by the CI data, however the H₂ analysis was not completed because of the super-solar [Fe/S] and [Ni/S].

•*Component 4*: The H₂ derived $T = 276$ K is consistent with the 2σ CI range of $T = 40 - 794$ K. The density derived from H₂, $n(\text{H I}) \sim 1600$ cm⁻³ is not compatible with the CI limits. Finally, the H₂ derived $J_{\nu}^{total,H_2} = 2.25 \times 10^{-19}$ ergs cm⁻² s⁻¹ Hz⁻¹ sr⁻¹ is within range allowed by CI and much lower than that predicted by CII* ($J_{\nu}^{total,CII*} = 52.7 \times 10^{-19}$ ergs cm⁻² s⁻¹ Hz⁻¹ sr⁻¹).

•*Component 6*: Because we only obtained upper limits on the CI** state of CI component 6 we can not make direct comparisons in this case. We can however, compare with CI component 5. In this case, the H₂ derived $T = 587$ K is consistent with the 2σ CI limit $T \leq 1259$ K (or $T \leq 794$ depending on J_{ν}), and the H₂ derived $n(\text{H I}) = 10, 509$ cm⁻³ is also consistent with the lower limits placed by CI data. The radiation field derived from the H₂, $J_{\nu}^{total,H_2} = 18.8 \times 10^{-19}$ ergs cm⁻² s⁻¹ Hz⁻¹ sr⁻¹, is consistent with the limits placed by CI, however these are both much lower than the $J_{\nu}^{total,CII*}$ predicted by the CII* technique.

•*Component 8*: The H₂ derived $T = 475$ K is inconsistent with the 2σ CI limit, $T \leq 158$ K. The H₂ derived density, $n(\text{H I}) = 3595$ cm⁻³, is also incompatible with the range allowed by CI ($n(\text{H I}) = 12 - 209$ cm⁻³). However, the H₂ derived radiation field, $J_{\nu}^{total,H_2} \leq 5.13 \times 10^{-19}$ ergs cm⁻² s⁻¹ Hz⁻¹ sr⁻¹ is compatible with the limits set by CI, and similar to that predicted by the CII* technique, $J_{\nu}^{total,CII*} = 11 \times 10^{-19}$ ergs cm⁻² s⁻¹ Hz⁻¹ sr⁻¹.

•*Component 9*: The H₂ derived $T = 151$ K is consistent with the 2σ CI limit, $T \leq 398$ K. The H₂ derived density, $n(\text{H I}) = 377$ cm⁻³, is also nearly compatible with the range allowed by CI ($n(\text{H I}) = 28 - 363$ cm⁻³).

However, the H₂ derived radiation field, $J_\nu^{total, H_2} \leq 0.48 \times 10^{-19}$ ergs cm⁻² s⁻¹ Hz⁻¹ sr⁻¹, while compatible with the limits set by CI, is not compatible with that predicted by the C II* technique, $J_\nu^{total, C II^*} = 11 \times 10^{-19}$ ergs cm⁻² s⁻¹ Hz⁻¹ sr⁻¹.

A striking difference is seen in the densities derived from the CI and H₂ data. A similar difference has been reported in sightlines towards Q0013–004 and Q1232+082 (Hirashita & Ferrara 2005) and HE0515–00 (Reimers et al. 2003; Quast et al. 2002). They argue that if the density is this high, i.e. equal to the critical density, then the states should be thermalized and there would be no difference in the excitation temperature as determined by the J = 1 and J = 2 states. Given that the observed T₀₂ is always much greater than T₀₁, Hirashita & Ferrara (2005) propose, following the suggestion of Reimers et al. (2003), that a potential explanation may be that the H₂ formation rate (R_{dust}) may be larger than estimated, which would result from, for example, a smaller than estimated grain size. Therefore, if the formation rate is higher, you require a smaller density than that derived. On the other hand, for each component of DLA 2340–00 studied here, the T₀₂ is either less than or approximately the same as T₀₁, implying that the critical density cannot be ruled out.

5. DISCUSSION

We have used CI fine structure absorption in high resolution, high signal-to-noise data to study the physical conditions in DLAs at high redshift. Our work differs from previous studies of CI fine structure absorption because we did not assume a gas temperature in order to derive the density. Rather, we assume ionization equilibrium, which in conjunction with the CI fine structure data, allows us to constrain *both* the temperature and the density of the cloud. In addition, we use the C II* technique to infer the local radiation field due to stars and include its contribution to the CI fine structure excitation, thus providing a complete and fully self-consistent model of the gas. In most cases, the CI fine structure excitation is consistent with the $J_\nu^{local, C II^*}$, derived independently by the C II* technique.

5.1. Assessment of Systematic Errors

To draw meaningful comparisons between the CI results and those of the C II* technique we must first analyze our possible systematic errors. The primary source of error in the CI analysis stems from two sources – 1) measurement error of the fine structure column densities, including possible errors in the oscillator strengths (we report results for 2 σ errors, which should encompass these errors¹²), and 2) the assumption that in solar units the carbon abundance is equal to that of Si II (or S II) –0.2 dex in case of minimal depletion. The source of systematic errors in the C II* technique are more difficult to assess (see WGP03 for a complete discussion). We explore the possible effects of these errors in the following section and demonstrate that, even considering

¹² For example, tests run using Jenkins 2006 f-values for CI produced a Doppler parameter $\sim 15\%$ larger and column density ~ 0.3 dex smaller than the Morton 2003 values in the case of the curve of growth analysis of the narrow, cold component in DLA 0812+32 (Jorgenson et al. 2009).

these errors, the CI data appear to be probing gas of higher densities and pressures – likely small knots of gas within the larger DLA galaxies – than that probed by the ‘global’ C II* technique.

5.1.1. Comparison with C II* technique model

While it is difficult to assess the systematic errors involved in the C II* technique, some of the potential uncertainties have been removed since the work of WGP03. For example, the SMC dust model is now assumed to be correct because of the non-detection of the 2175Å dust feature that would have indicated Galactic dust, while the reddening curve resembles SMC rather than Galactic or LMC (Vladilo et al. 2008). Therefore, we focus on the two largest potential uncertainties: 1) the assumption of the equilibrium pressure, P_{eq} , and 2) the minimal versus maximal, depletion model (see discussion in section 2.3 of WGP03). The standard C II* technique involves solving the equations of thermal and ionization equilibrium as described in WGP03 and Wolfire et al. (1995). A unique solution is determined by assuming that the equilibrium pressure is equal to the geometric mean between P_{max} and P_{min} , $P_{eq} = P_{geo} = (P_{min}P_{max})^{1/2}$, where P_{min} and P_{max} are the minimum and maximum pressures of the function P(n) where n is gas density. This results in two stable solutions for a given star formation rate, one WNM and one CNM, and is the basis of the two-phase model. However, a two-phase medium can achieve equilibrium with a pressure ranging from P_{min} to P_{max} , and therefore, the assumption of P_{eq} equal to the geometric mean, while reasonable (see Wolfire et al. 2003 and WGP03 discussion), is still an unproven assumption. Following WGP03 we attempt to gain a sense of the possible systematic errors by allowing P_{eq} to vary between P_{min} and P_{max} . In Figure 23, we show the standard two-phase diagram, plotting in (a), $\log(P/k)$ versus density for various star formation rates per unit area (which is proportional to J_ν) which are constant along each P(n) curve, and which increase from bottom to top, and in (b) $\log(\ell_c)$ versus density for ℓ_c equilibrium solutions for those same star formation rates. The green dashed line in each plot indicates the P(n) solution for heating by background radiation alone (i.e. $\log \Sigma_{SFR} = -\infty$). The black horizontal line in (b) denotes the observed cooling rate of DLA 1331+17, $\log(\ell_c) \leq -27.14$ ergs s⁻¹ H⁻¹. Three vertical, black, dotted lines illustrate the location of the CNM stable points associated with, from left to right, P_{min} , $P_{geo} = (P_{min}P_{max})^{1/2}$, and P_{max} for the case of background radiation alone. The stable (ℓ_c , n) pairs for the grid of star formation rates are denoted by the three red lines in (b), where the three different pressure assumptions have been made – from left to right they are: dashed = P_{min} , dot-dashed = P_{geo} and dotted = P_{max} . Although not relevant for our current discussion, it is seen that P_{min} requires a higher star formation rate and lower density to achieve an equilibrium solution with a cooling rate equal to that observed. On the opposite extreme, P_{max} requires a higher density and lower star formation rate.

For the purposes of this paper, we are interested in the range of densities and temperatures that result from these different model assumption inputs to the C II* technique. In Figure 24, we plot the resultant $\log(P/k)$ ver-

sus density for our example case of DLA 1331+17. For the minimal depletion model, the case of $P_{eq} = P_{geo} = (P_{min}P_{max})^{1/2}$ is denoted by the asterisk. Lines connect to the P_{min} and P_{max} solutions, providing a sense for the potential systematic "error" involved in the assumption of where the equilibrium pressure resides. We have also plotted the results of the maximal depletion model, denoted by the diamond, with dashed lines connecting to the associated P_{min} and P_{max} solutions. To correctly compare this range of solutions to that of the CI data we must re-model the CI theoretical curves in each case because the change in the assumed P_{eq} results in a change of star formation rate, or J_{ν}^{local} , which is an input for the CI theoretical curves. We plot the 2σ results of the CI analysis for J_{ν}^{local} spanning that determined by P_{min} and P_{max} . We summarize the results of these two techniques for DLA 1331+17 in Table 12.

In Figure 25 we summarize the results of our CI sample and compare them to the CII*-derived and H₂-derived models of the same systems. We plot the best-fit CI solutions, as determined by χ^2 minimization, as circles, while the shaded regions denote the 2σ CI solutions. The CII* solutions are represented as diamonds. It is seen that the densities determined by the CII* technique are systematically lower than those determined by the CI data. As a result, the overall pressures are lower. The temperatures vary depending on model assumptions, but are in general agreement or higher than the CI results (see Table 12). We conclude that the CI gas is tracing a denser region of the DLA than that traced by the global CII* technique: essentially, the CI resides primarily in small, overdense knots. However, one problem with this picture is understanding how these two phases, the low pressure ambient medium and the higher pressure smaller 'clumps' of CI-bearing gas, remain in pressure equilibrium. We return to this issue in a following paper.

These comparisons also reveal a discrepancy between the $\frac{CII}{CI}$ derived by the CII* technique analysis and the observed $\frac{CII}{CI}$. In general, the observed $\frac{CII}{CI}$ ratio is approximately an order of magnitude smaller than that predicted by the CII* technique model (see Table 12). We avoid a detailed discussion here and refer the interested reader to WGP03, section 5.1, for a detailed discussion of the model inputs that affect $\frac{CII}{CI}$. We only briefly mention that we have tested the results with cosmic rays turned on and off, and there is not a large effect on the results for the star formation rates we are considering. However, this is not the case for large star formation rates, $J_{\nu}^{total} \sim 10^{-18}$ ergs cm⁻² s⁻¹ Hz⁻¹ sr⁻¹, for which the effect of cosmic rays becomes more important. Assuming that the CII* technique model is correct, we can understand this difference in terms of the new model in which the bulk of the measured CI is localized in small, dense clumps, $\approx 1 - 10$ pc, relative to the larger DLA (for estimates of the cloud size, see last column in Table 5). In this case, while the cloud is still optically thin and feels the same radiation field as the surrounding medium, the increased density, and hence, increased electron density, n_e , of the CI cloud work to lower $\frac{CII}{CI}$ because $\frac{CII}{CI}$ is inversely proportional to density for a fixed radiation field. In a sense, this conflict with the predictions of the 'global' CII* technique model, is an

expected result of the overdense-CI -region model.

5.1.2. Direct Estimate of Error on J_{ν}^{local}

While there are many assumptions and uncertainties in the CII* technique, we can make a direct estimate of the possible error on J_{ν}^{local} derived from the CII* technique by using the $z_{abs} = 1.9$ DLA 2206-19. In Wolfe et al. (2004), the FUV radiation field inferred from an image of a galaxy associated with this DLA (Warren et al. 2001) is compared with the radiation field inferred from the CII* technique and they are found to agree to within $\sim 50\%$. Therefore, we will assume that the error on J_{ν}^{local} is $\sim 50\%$.

5.1.3. Distribution of CII

Throughout this work we assume that the measured N(CII) can be directly applied to each CI cloud. However, assuming that there is no hidden saturation – which would actually increase the N(CII) – this is actually an upper limit to the amount of N(CII) associated with each CI cloud. The distribution of CII along the line of sight could be clumpy such that only a fraction of the measured N(CII) is associated with a given CI cloud. With respect to the analysis done in this paper, the effect of decreasing the amount of CII associated with the CI cloud causes an increase in the resultant volume density and a decrease in the temperature such that the pressure remains approximately constant. The increase in volume density with decreasing fraction of CII results in a decrease of the derived cloud size as shown in Figure 26.

5.2. Relation to 'high-cool' DLA population

With the exception of DLA 1331+17, all of the CI-bearing objects not only contain CII* (as compared with $\sim 50\%$ of the general DLA population) but also have cooling rates, ℓ_c , that place them firmly in the 'high-cool' range defined by Wolfe et al. (2008) (median 'high-cool' $\log \ell_c = -26.6$ ergs s⁻¹ H⁻¹). A literature search reveals that all previously published DLAs with positive detections of CI fall into the 'high-cool' population as well. While it is not clear how the bimodality discovered by Wolfe et al. (2008) is related to CI, this correlation – that almost all CI-bearing DLAs are also high-cool DLAs – could simply be a result of the higher metallicities and dust-to-gas ratios that are required to form and sustain, through dust shielding of UV radiation, measurable amounts of H₂ and CI. This trend, of higher metallicity DLAs being more likely to contain measurable H₂, has been observed previously by Petitjean et al. (2006). Additionally, the 'high-cool' DLAs, shown by Wolfe et al. (2008) to consist of primarily CNM, simply might be an environment more conducive to the presence of H₂ and CI.

5.3. Comparison with the local ISM

In this section we compare our CI-bearing clouds to the ISM of the local Universe, namely, the Milky Way and the Small and Large Magellanic Clouds (the SMC and LMC respectively). To draw these comparisons, we first determine the median n(H I), T, and P of our CI sample. Of course, this median is dependent upon which models we choose to include. Here, we include the models

for each DLA that are likely to be the most physically realistic, i.e. case (a), the low- ℓ_c , minimal depletion model for DLA 0812+32, $z_{abs}=2.06$, and the 'global' models for both DLA 0812+32, $z_{abs} = 2.62$ and DLA 2340-00. We chose the 'global' models as the most likely to be correct because of the inherent uncertainty in determining the distribution of both the N(H I) and the metals amongst the velocity components necessary for the component by component analysis. A summary of these models is shown in Figure 25. The resulting median values for this sample are: $\langle n(\text{H I}) \rangle = 69 \text{ cm}^{-3}$, $\langle T \rangle = 50 \text{ K}$, and $\langle \log(P/k) \rangle = 3.86 \text{ cm}^{-3} \text{ K}$, with standard deviations, $\sigma_{n(\text{H I})} = 134 \text{ cm}^{-3}$, $\sigma_T = 52 \text{ K}$, and $\sigma_{\log(P/k)} = 3.68 \text{ cm}^{-3} \text{ K}$.

In the Milky Way, Jenkins & Tripp (2001) used very high resolution ($R = 200,000$) STIS data to analyze C I fine structure populations and find a median $\log(P/k) = 3.35 \text{ cm}^{-3} \text{ K}$. This median pressure is similar to the pressures we derive in high redshift C I-bearing DLAs, where the median pressures derived are typically $\log(P/k) = 3 - 4 \text{ cm}^{-3} \text{ K}$. While this would seem to indicate that physical conditions similar to the Milky Way exist in high- z DLAs, we point out that in the case of the Milky Way, the high pressure is driven by the much higher heating rate ($\log \ell_c \sim -25 \text{ ergs s}^{-1} \text{ H}^{-1}$), a result of the higher dust-to-gas ratio (typically 30 times that of DLAs). In contrast, the heating rates in high redshift DLAs are generally 1-2 orders of magnitude smaller. Hence, the pressures derived in the C I-bearing clouds, while similar to those observed in the Milky Way, are not the result of the same physical conditions as those observed in the Milky Way. Jenkins & Tripp (2001) also observe a small proportion of the gas in many sightlines to be at very high pressures, $P/k > 10^5 \text{ cm}^{-3} \text{ K}$, which they speculate are caused by converging flows in a turbulent medium or in turbulent boundary layers: such pressures have not been detected in DLAs.

It is perhaps more meaningful to compare DLAs with the Large and Small Magellanic Clouds that, like DLAs, are known to have sub-Milky Way dust-to-gas ratios and metallicities. Tumlinson et al. (2002) performed a FUSE survey of H_2 along 70 sightlines to the Small and Large Magellanic Clouds. For all sightlines with $\log N(\text{H}_2) \geq 16.5 \text{ cm}^{-2}$ they find $\langle T_{01} \rangle = 82 \pm 21 \text{ K}$, whereas for all sightlines (including those at lower columns), they find $\langle T_{01} \rangle = 115 \text{ K}$. This can be compared with the Galactic average, $T = 77 \pm 17 \text{ K}$ (Savage et al. 1977). The temperatures found by the C I and H_2 data presented here are in broad agreement with these values. A noticeable exception to this agreement are the temperatures derived from the H_2 rotational states in DLA 2340-00. They are generally higher ($T_{ex}^{01} \approx 150 - 600 \text{ K}$) than those found in the SMC/LMC and in better agreement with the mean kinetic temperature of the gas, $T = 153 \pm 78 \text{ K}$, found by Srianand et al. (2005) in a sample of H_2 -bearing DLAs at high- z .

6. CONCLUSIONS

The goal of this paper is to present new detections of neutral carbon in high redshift DLAs and to present a new method for analyzing the C I fine structure lines. As done by several other authors, we utilize C I fine structure lines to determine densities, however, instead of as-

suming a temperature, our work constrained the allowed density and temperature combinations using only the column density of C I in the fine structure states and the assumption of ionization equilibrium. In a second paper, we will incorporate these physical conditions into a general model for C I-bearing DLAs. Our major conclusions are as follows:

1. The steady state analysis of C I fine structure populations along with the assumption of ionization equilibrium provides realistic constraints on both the volume density *and* temperature of high redshift DLAs. The C I data are in general consistent with the radiation fields, $J_\nu^{local, C II^*}$, derived from the C II* technique and provide further evidence of the presence of CNM in high redshift DLAs.
2. The densities and pressures of the C I - bearing gas are systematically higher than those of the 'global' DLA predicted by the C II* technique. We propose two physical scenarios that could be consistent with the data presented here. First, the C I could be tracing overdensities that are created by shocks, hence the C I exists in the post-shock cool gas. However, it seems likely that the post-shock gas would have a systemic velocity offset from the pre-shock gas. This is not observed. In fact, the general good agreement between the velocity centroids of the C I and other resonance lines argues against the shock idea. A second scenario is that the C I exists in higher density, higher-pressure edge of a photodissociation region, i.e. the edge of a molecular cloud. While the high optical depth through a classical molecular cloud would obscure a background quasar, the photodissociation region, or edge of the molecular, cloud could be optically thin enough to allow transmission of the background quasar light and would be consistent with the gas physics determined by the C I fine structure lines.
3. As noted by Srianand et al. (2005), all C I - bearing DLAs also contain C II* absorption. We find that, with only one exception, all C I objects for which C II* coverage is available (5 presented in this paper, 1 yet to be published, and 7 from the literature) contain strong C II* absorption, placing them in the category of 'high-cool' DLAs. This could be simply a consequence of the fact that C I -bearing DLAs generally host larger fractions of H_2 whose formation is encouraged by the higher than average metallicities and dust-to-gas ratios, consistent with the 'high-cool' population of DLAs.
4. High resolution studies of neutral carbon lines reveal narrow, sub-1km s^{-1} , cold and unresolved components. These components likely contain relatively large amounts of gas and are most likely cold, dense knots, perhaps photodissociation regions on the edges of star forming regions. This would explain the presence of C I, H_2 , and larger than average dust-to-gas ratios. To date, two such components have been published; in DLA 0812+32 with a temperature of $T \leq 78 \text{ K}$ (Jorgenson et al. 2009) and in DLA 1331+17 with $T \leq 218 \text{ K}$

(Carswell et al. 2010) and we presented an additional candidate in this paper. Such clouds may exist in all CI systems. Their non-detection in other CI systems does not rule out their existence due to the difficulty in detecting such small equivalent widths that are likely blended with other velocity components. It is possible that these narrow components are ubiquitous and contain significant amounts of gas that has been previously missed in lower resolution studies.

The authors wish to thank Bob Carswell for many useful discussions. R.A.J. acknowledges support from the STFC-funded Galaxy Formation and Evolution programme at the Institute of Astronomy, University of Cambridge. A.M.W., R.A.J., & J.X.P. acknowledge partial support by NSF grant AST-07-09235. The authors wish to recognize and acknowledge the very significant cultural role and reverence that the summit of Mauna Kea has always had within the indigenous Hawaiian community. We are most fortunate to have the opportunity to conduct observations from this mountain.

7. APPENDIX 1: MOLECULAR HYDROGEN

The purpose of this Appendix is to present an outline of the molecular hydrogen analysis performed in this work. While the focus of this work was the analysis of neutral carbon, DLAs that contain neutral carbon are likely to also contain detectable H_2 . This is because neutral carbon and molecular hydrogen are photoionized and photodissociated respectively, by photons of the same energies and therefore, they are usually found together. This is the case in several of the DLAs presented in this work, i.e. DLA 1331+17, DLA 0812+32, and DLA 2340-00. For DLA 2231-00 and the low- z DLA 0812+32, we did not have coverage of the H_2 region and therefore cannot determine anything about the presence of H_2 . Here we present an outline of the DLA H_2 analysis frequently performed in the literature, most recently by works such as Levshakov et al. (2002), Hirashita & Ferrara (2005), Cui et al. (2005), Noterdaeme et al. (2007a), and Noterdaeme et al. (2007b) and based upon work by Spitzer & Zweibel (1974), Jura (1975a) and Jura (1975b). Essentially, the measurement of H_2 in the different rotational J states allows for an independent estimation of the physical properties of the cloud such as density, temperature and the incident radiation field. While the H_2 analysis arguably contains several uncertainties and assumptions, it is nonetheless interesting to compare the results from these two independent methods, the H_2 analysis we present below and the CI fine structure analysis presented in this work.

First, we can estimate the kinetic temperature of the cloud using the column densities of H_2 in the $J=0$ and higher J rotational states. According to the Boltzmann distribution (see equation 8 in Levshakov et al. (2002)):

$$\frac{N(J)}{N(0)} = \frac{g(J)}{g(0)} e^{-\frac{B_v J(J+1)}{T_{ex}}} \quad (8)$$

where $B_v = 85.36$ K for the vibrational ground state and $g(J)$ is the degeneracy of level J, given by, for level $J = x$, $g_x = (2J_x + 1)(2I_x + 1)$ where $I = 0$ for even x and $I =$

1 for odd x (For states $J = 0-5$, $g = [1, 9, 5, 21, 9, 33]$). The excitation diagram is typically plotted as $\log(N_J / g_J)$ versus the relative energy between the level J and $J = 0$. The excitation temperature, defined in equation 8, is inversely proportional to the negative slope of the line connecting the excitation diagram points, i.e.

$$T_{ex}^{0J} = -B_v J(J+1) \frac{1}{\ln \frac{g_0 N_J}{g_J N_0}} \quad (9)$$

The typical assumption is that the kinetic temperature of the cloud can be estimated by the excitation temperature derived from the population of H_2 in the states $J = 0$ and $J = 1$, assuming that the $J = 1$ level is thermalized. Because the critical density of the low J states is relatively small, the population of the low J levels is generally dominated by collisional excitation and therefore it reflects the kinetic temperature of the gas when in local thermodynamical equilibrium. The higher J states ($J \geq 2$) are typically characterized by a higher T_{ex} , or flatter slope, which is explained by population mechanisms other than collisions.

The higher T_{ex} derived from the population of H_2 in the higher rotational J states was originally unexpected (Spitzer & Zweibel 1974). After observations by Spitzer and Chochran in the 1970s in which they observed the high excitation temperatures derived from the high J states, Spitzer & Zweibel (1974) proposed methods other than collisions that could populate the higher J states. They proposed two methods other than collisions: 1) the cascade down from upper vibrational levels following the absorption and reemission of Lyman and Werner band photons - i.e. the $J = 0$ molecule is excited to a higher vibrational state and then de-excites to a higher J state in the ground vibrational state (rather than staying in the original $J=0$ or $J=1$ state), or 2) the direct formation of H_2 in a higher state (i.e. the H_2 pops off the dust particle in an excited state and cascades to say $J = 4$). Since these processes are believed to dominate collisions, the typical practice is to neglect collisions and to consider only these two processes, as we show in the following analysis.

Assuming steady state and neglecting collisions, we use the two afore mentioned populating mechanisms and assume depopulation by spontaneous emission (true until the density is above 10^4), to write the following steady state equations for state $J = 4$ and $J = 5$ respectively (these are equations 2a and 2b from Jura (1975b)),

$$p_{4,0} \beta_0 n(H_2, J=0) + 0.19 R n(HI) n(H) = A_{4,2} n(H_2, J=4) \quad (10)$$

and

$$p_{5,0} \beta_1 n(H_2, J=1) + 0.44 R n(HI) n(H) = A_{5,3} n(H_2, J=5) \quad (11)$$

where p is the pumping coefficient or pumping efficiency (or by Jura, the redistribution probability) into the $J=4$ and $J=5$ levels from the $J=0$ and $J=1$ levels respectively, β is the photoabsorption rate, R is the H_2 molecule formation rate (on dust grains, also known as R_{dust}), $n(HI)$ is the neutral hydrogen number density, $n(H) \approx n(HI) + 2n(H_2)$, and A is the spontaneous transition probabilities. In other words, the first term is the UV excitation

and decay to higher J state, while term 2 represents the direct formation in the higher J state. The values of the constants are as follows: $A_{4,2} = 2.75 \times 10^{-9} \text{s}^{-1}$, $A_{5,3} = 9.9 \times 10^{-9} \text{s}^{-1}$ (Spitzer 1978), $p_{4,0} = 0.26$, $p_{5,1} = 0.12$ (Jura 1975b). Solving for β will allow us to estimate the UV field incident on the cloud, while β together with R will allow us to estimate the neutral hydrogen density.

In order to solve for β and to get rid of the $N(\text{H I})$ dependence in equation 10, we take advantage of the assumption of equilibrium between the formation and the destruction of H_2 (which is reasonable because the time scales of H_2 formation and destruction are well below a dynamical time), as follows,

$$Rn(\text{HI})n(\text{H}) = R_{diss}n(\text{H}_2) \quad (12)$$

If we substitute equation 12 into equation 10, and make the common assumption that 11% of photoabsorption leads to photodissociation (Jura 1974b),

$$R_{diss} = 0.11\beta \quad (13)$$

we obtain equilibrium equations that are independent of the neutral hydrogen column density N_{HI} ,

$$p_{4,0}\beta_0 \frac{N(\text{H}_2, J=0)}{N(\text{H}_2)} + 0.021\beta_0 = A_{42} \frac{N(\text{H}_2, J=4)}{N(\text{H}_2)} \quad (14)$$

and

$$p_{5,0}\beta_1 \frac{N(\text{H}_2, J=1)}{N(\text{H}_2)} + 0.049\beta_1 = A_{53} \frac{N(\text{H}_2, J=5)}{N(\text{H}_2)} \quad (15)$$

Using the measured H_2 column densities we can then solve for β , the photoabsorption rate of H_2 in each component. Note, that β_0 should equal β_1 .

Once we have solved for β we can determine the incident radiation field by using the relation between the radiation field and the photodissociation rate that it induces on the molecular hydrogen. Following Abel et al. (1997) and Hirashita & Ferrara (2005),

$$R_{diss} = (4\pi)1.1 \times 10^8 J_\nu^{LW} S_{shield} \delta^{-1} \quad (16)$$

where R_{diss} is the photodissociation rate ($= 0.11\beta$ as above), J_ν^{LW} (LW stands for Lyman-Werner) is the UV intensity at $h\nu = 12.87 \text{ eV}$ averaged over the solid angle (12.87 eV is the dominant energy at which the photodissociation happens). This can be compared with the J_ν that is typically calculated in the CII* technique at $\lambda = 1500\text{\AA}$, or 8.27 eV. S_{shield} accounts for shielding due to two effects: 1) dust shielding and 2) self-shielding. In order to solve for J_ν^{LW} we must determine the effects of shielding in equation 16. We estimate the shielding, following Hirashita & Ferrara (2005), as

$$S_{shield} = \left(\frac{N(\text{H}_2)}{10^{14} \text{cm}^{-2}} \right)^{-0.75} e^{-\sigma_d N_d} \quad (17)$$

where the first term expresses the self-shielding and the exponential term is the shielding due to dust. N_d , the column density of dust, is related to the HI column density by: $(4/3)\pi a^3 \delta N_d = 1.4 m_{\text{H}} N_{\text{HI}} D$, where 1.4 is the

correction for the helium content, and σ_d is the cross-section of a grain, $\sigma_d = \pi a^2$. $\sigma_d N_d = \tau_{UV}$ is the optical depth in dust and is expressed by Hirashita & Ferrara (2005) as,

$$\tau_{UV} = \frac{4.2 N_{\text{HI}} m_{\text{H}} D}{4a\delta} = 0.879 \left(\frac{a}{0.1 \mu\text{m}} \right)^{-1} \left(\frac{\delta}{2g \text{cm}^{-3}} \right)^{-1} \left(\frac{D}{10^{-2}} \right) \left(\frac{N_{\text{HI}}}{10^{21} \text{cm}^{-2}} \right) \quad (18)$$

where a is the radius of a grain, δ is the grain material density, and D is the dust-to-gas mass ratio. Hirashita & Ferrara (2005) assume the Galactic (Milky Way) dust-to-gas mass ratio to be $D_\odot = 0.01$. They define the normalized dust-to-gas ratio $\kappa = D/D_\odot$. Assuming $a=0.1$ and $\delta=2$, equation 18 can be written,

$$\tau_{UV} = 0.879\kappa \left(\frac{N_{\text{HI}}}{10^{21} \text{cm}^{-2}} \right) \quad (19)$$

see Cui et al. (2005) equation 7.

The first part of equation 17, the self-shielding of H_2 , is taken from an analytic approximation from Draine & Bertoldi (1996) and is valid for $N(\text{H}_2) > 10^{14} \text{cm}^{-2}$. We can therefore rewrite equation 17 as,

$$S_{shield} = \left(\frac{N(\text{H}_2)}{10^{14} \text{cm}^{-2}} \right)^{-0.75} \exp[-0.879\kappa \left(\frac{N_{\text{HI}}}{10^{21} \text{cm}^{-2}} \right)] \quad (20)$$

Therefore, given β and S_{shield} we can use equation 16 to solve for the ambient radiation field, J_ν^{LW} . Note that this is the total radiation field, or $J_\nu^{LW} = J_\nu^{total}$.

We can also use the measurements of $N(\text{H}_2)$ to estimate the volume density of H I. We define the molecular fraction, f_{H_2} as follows,

$$f_{\text{H}_2} = \frac{2n(\text{H}_2)}{n(\text{HI}) + 2n(\text{H}_2)} = \frac{2N(\text{H}_2)}{N(\text{HI}) + 2N(\text{H}_2)} \quad (21)$$

where we measure the $N(\text{H I})$ and the $N(\text{H}_2)$ directly. If we substitute 21 into 12 and remember that $n(\text{H}) \approx n(\text{H I}) + 2n(\text{H}_2)$, we can solve for the number density of hydrogen,

$$Rn(\text{HI}) = R_{diss} \frac{n(\text{H}_2)}{n(\text{HI}) + 2n(\text{H}_2)} = R_{diss} \frac{f_{\text{H}_2}}{2} \quad (22)$$

or

$$n(\text{HI}) = \frac{R_{diss} f_{\text{H}_2}}{R} \quad (23)$$

This is temperature dependent however, and we will use the detailed expression for R given by Hirashita & Ferrara (2005) (note, they call it R_{dust}),

$$R = 4.1 \times 10^{-17} S_d(T) \left(\frac{a}{0.1 \mu\text{m}} \right)^{-1} \left(\frac{D}{10^{-2}} \right) \left(\frac{T}{100\text{K}} \right)^{1/2} \left(\frac{\delta}{2g\text{cm}^{-3}} \right)^{-1} \quad (24)$$

where $S_d(T)$ is the sticking coefficient of hydrogen atoms onto dust and everything else was defined previously. The sticking coefficient is given by (Hollenbach & McKee (1979); Omukai (2000)

$$S_d(T) = [1 + 0.04(T + T_d)^{0.5} + 2 \times 10^{-3}T + 8 \times 10^{-6}T^2]^{-1} \times (1 + \exp[7.5 \times 10^2(1/75 - 1/T_d)])^{-1} \quad (25)$$

where T_d is the dust temperature and is given by

$$T_d = 12(\chi Q_{UV})^{1/6} \left(\frac{A}{3.2 \times 10^{-3} \text{cm}} \right)^{-1/6} \left(\frac{a}{0.1 \mu\text{m}} \right)^{-1/6} K \quad (26)$$

where A is a constant that depends on the optical properties of the dust grains. For silicate grains, $A = 1.34 \times 10^{-3}$ cm and for carbonaceous grains, $A = 3.20 \times 10^{-3}$ cm. Following Hirashita & Ferrara (2005) we assume $Q_{UV} = 1$ (Q_{UV} is the dimensionless absorption cross-section normalized by the geometrical cross-section), $A = 3.20 \times 10^{-3}$ cm and $a = 0.1 \mu\text{m}$, while χ , the normalized radiation field, was calculated previously from the H_2 levels ($\chi = J_\nu^{LW} / J_\nu^{LW}_\odot$ where $J_\nu^{LW}_\odot = 3.2 \times 10^{-20}$ ergs cm^{-2} s^{-1} Hz^{-1} sr^{-1}). Therefore, we can determine R as a function of T . In the present work, we assume that T is equal to the excitation temperature as derived from the $J=0$ and $J=1$ H_2 states. Finally, we use equation 23 to estimate the neutral hydrogen density. Note, this method of determining temperature, density and radiation field, is independent of the CI fine structure data.

REFERENCES

- Abel, N. P., Brogan, C. L., Ferland, G. J., O'Dell, C. R., Shaw, G., Troland, T. H., 2004 *ApJ*, 609, 247
- Abrahamsson, E., Krems, R.V. & Dalgarno, A. 2007, *ApJ*, 654,1171
- Anders, E. & Grevesse, N., 1989, *GeCoA*, 53, 197
- Carswell, R. F., Hilliard, R. L., Strittmatter, P. A., Taylor, D. J., & Weymann, R. J. 1975, *ApJ*, 196, 351
- Carswell, R. F., et al. MNRAS submitted
- Cui, J., Bechtold, J., Ge, J., Meyer, D. M. 2005, *ApJ*, 633, 649
- Curran, S. J., & Webb, J. K. 2006, *MNRAS*, 371, 356
- Dessauges-Zavadsky, M., Calura, F., Prochaska, J. X., D'Oorico, S., & Matteucci, F., 2004, *A & A*, 416, 79
- Draine, B. T., Bertoldi, F. 1996, *ApJ*, 468, 269
- Ge, J., Bechtold, J., & Black, J. 1997, *ApJ*, 474, 67
- Haardt, F. & Madau, P. 1996, *ApJ*, 461, 20
- Hirashita, H. & Ferrara, A. 2005, *MNRAS*, 356, 1529
- Hollenbach D. J., McKee C. F., 1979, *ApJS*, 41, 555
- Howk, J. C., Wolfe, A. M., Prochaska, J. X., 2005, *ApJ*, 622, L81
- Jenkins, E. B., & Shaya, E. J., 1979, *ApJ*, 231 55
- Jenkins, E. B., & Tripp, T. M. 2001, *ApJ*, 137, 297
- Jenkins, E. B., & Tripp, T. M. 2006, *ApJ*, 637, 548
- Jenkins, E. B., private communication
- Jenkins, E. B., & Tripp, T. M. 2007, *ASPC*, 365, 51
- Jura, M. 1974a, *ApJ*, 190, L33
- Jura, M. 1974b, *ApJ*, 191, 375
- Jura, M. 1975a, *ApJ*, 197, 575
- Jura, M. 1975b, *ApJ*, 197, 581
- Johnson, C.T., Burke, P.G., & Kingston, A.E. 1987, *J. Phys. B*, 20, 2553
- Jorgenson, R. A., Wolfe, A. M., Prochaska, J. X., & Carswell, R. F. 2009, *ApJ*, 704, 247
- Kanekar, N. & Chengalur, N. J. 2003, *A & A*, 399, 857
- Kanekar, N. & Chengalur, N. J. & Lane, W. M. 2007, *MNRAS*, 375, 1528
- Ledoux, C., Petitjean, P., Fynbo, J. P. U., Møller, P., & Srianand, R. 2006, *A & A*, 457, 71
- Ledoux, C., Petitjean, P., & Srianand, R. 2006, *ApJL*, 640, L25
- Lehner, N., Howk, J. C., Prochaska, J. X., & Wolfe, A. M. 2008, *ArXiv e-prints*, 807, arXiv:0807.0930
- Levshakov, S. A., Dessauges-Zavadsky, M., D'Ordorico, S., & Molaro, P., 2002, *ApJ*, 565, 696
- Narayanan, A., Misawa, T., Charlton, J. C., & Ganguly, R. 2006, *AJ*, 132, 2099
- Noterdaeme, P., Petitjean, P., Srianand, R., Ledoux, C. & Le Petit, F. 2007, *A & A*, 469, 425
- Noterdaeme, P., Ledoux, C., Petitjean, P., Le Petit, F., Srianand, R., & Smette, A. 2007, *A & A*, 474, 393
- Noterdaeme, P., Ledoux, C., Petitjean, P., & Srianand, R. 2008, *A & A*, 481, 327
- Mather, J. C., Fixsen, D. J., Shafer, R. A., Mosier, C., & Wilkinson, D. T., 1999, *ApJ*, 512, 511
- Meyer, D.M., York D.G., Black, J.H.,Chaffee, Jr., F.H., & Foltz, C.B.,1986, *ApJ*, 308L, 37M
- Morton, D. C. 2003, *ApJS*, 149, 205
- Murphy, M. T., & Liske, J. 2004, *MNRAS*, 354, L31
- Omukai K. 2000, *ApJ*, 534, 809
- Petitjean, P., Ledoux, C., Noterdaeme, P., & Srianand, R. 2006, *A & A*, 456, L9
- Prochaska, J. X., & Wolfe, A. M. 2009, *ApJ*, 696, 1543
- Prochaska, J. X., Chen, H.-W., & Bloom, J. S. 2006, *ApJ*, 648, 95
- Prochaska, J. X., Herbert-Fort, S., & Wolfe, A. M. 2005, *ApJ*, 635, 123
- Prochaska, J. X., Howk, J. C., Wolfe, A. M. 2003, *Nature*, 423, Issue 6935, pp. 57-59
- Prochaska, J. X., Howk, J. C., O'Meara, J. M., Tytler, D., Wolfe, A. M., Kirkman, D., Lubin, D., & Suzuki, N. 2002, *ApJ*, 571, 693
- Prochaska, J. X., Wolfe, A. M., 1999, *ApJ*, 121, 369.
- Prochaska, J. X. 1999, *ApJ*, 511, L71.
- Quast, R., Baade, R., & Reimers, D. 2002, *A & A*, 386, 796
- Reddy, N. A., & Steidel, C. C. 2009, *ApJ*, 692, 778
- Reimers, D., Baade, R., Quast, R., & Levshakov, S. A. 2003, *A & A*, 410, 785
- Roueff, E., & Le Bourlot, J., 1990, *A & A*, 236,515
- Savage, B. D., & Sembach, K. R. 1991, *ApJ*, 379, 245
- Savage, B. D., Bohlin, R. C., Drake, J. F., & Budich, W. 1977, *ApJ*, 216, 291
- Savaglio, S., & Fall, S. M. 2004, *ApJ*, 614, 293
- Schroder, K., Staemmler, V., Smith, M. D., Flower, D. R., & Jaquet, R., 1991, *JPhB*, 24, 2487S
- Silva, A. L., & Viegas, S. M., 2001, *CoPhC*, 136, 319S
- Songalia, A., Cowie, L. L., Vogt, S., Keane, M., Wolfe, A. M., Hu, E. M., Oren, A. L., Tytler, D. R. & Lanzetta, K. M. 1994, *Nature*, 371, 43
- Spitzer, L. J., *Physical Processes in the Interstellar Medium*, 1978
- Spitzer, L. J., & Zweibel, E. G. 1974, *ApJL*, 191, L127
- Srianand, R., Petitjean, P., Ledoux, C., Ferland, G., & Shaw, G. 2005, *MNRAS*, 362, 549
- Tumlinson, J., et al. 2010, *ApJL*, 718, L156
- Tumlinson, J., et al. 2002, *ApJ*, 566, 857
- Vladilo, G., Prochaska, J. X., & Wolfe, A. M. 2008, *A & A*, 478, 701
- Warren, S. J., Møller, P., Fall, S. M., & Jakobsen, P. 2001, *MNRAS*, 326, 759
- Wolfe, A. M., & Davis, M. M., *AJ*, 1979, 84, 699
- Wolfe, A.M. 1985, *Phil. Trans. Roy. Soc. Lon.*, 321, 503
- Wolfe, A.M., Turnshek, D.A., Smith, H.E., & Cohen, R.D. 1986, *ApJS*, 61, 249
- Wolfe, A. M., Lanzetta, K. M., Foltz, C. B., and Chaffee, F. H. 1995, *ApJ*, 454, 698
- Wolfe, A. M., Prochaska, J.X. & Gawiser, E. 2003, *ApJ*, 593, 215
- Wolfe, A. M., Gawiser, E., & Prochaska, J.X. 2003, *ApJ*, 593, 235
- Wolfe, A. M., Howk, J. C., Gawiser, E., Prochaska, J.X. & Lopez, S. 2004, *ApJ*, 615, 625
- Wolfe, A. M., Gawiser, E., & Prochaska, J.X. 2005, *ARAA*, 43, 861
- Wolfe, A. M., & Chen, H.-W. 2006, *ApJ*, 652, 981
- Wolfe, A. M., Prochaska, J. X., Jorgenson, R. A., & Rafelski, M. 2008, *ApJ*, 681, 881
- Wolfire, M. G., Hollenbach, D., McKee, C. F., Tielens, A. G. G. M., & Bakes, E. L. O. 1995, *ApJ*, 443, 152
- York, B. A., Kanekar, N., Ellison, S. L., & Pettini, M. 2007, *MNRAS*, 382, L53

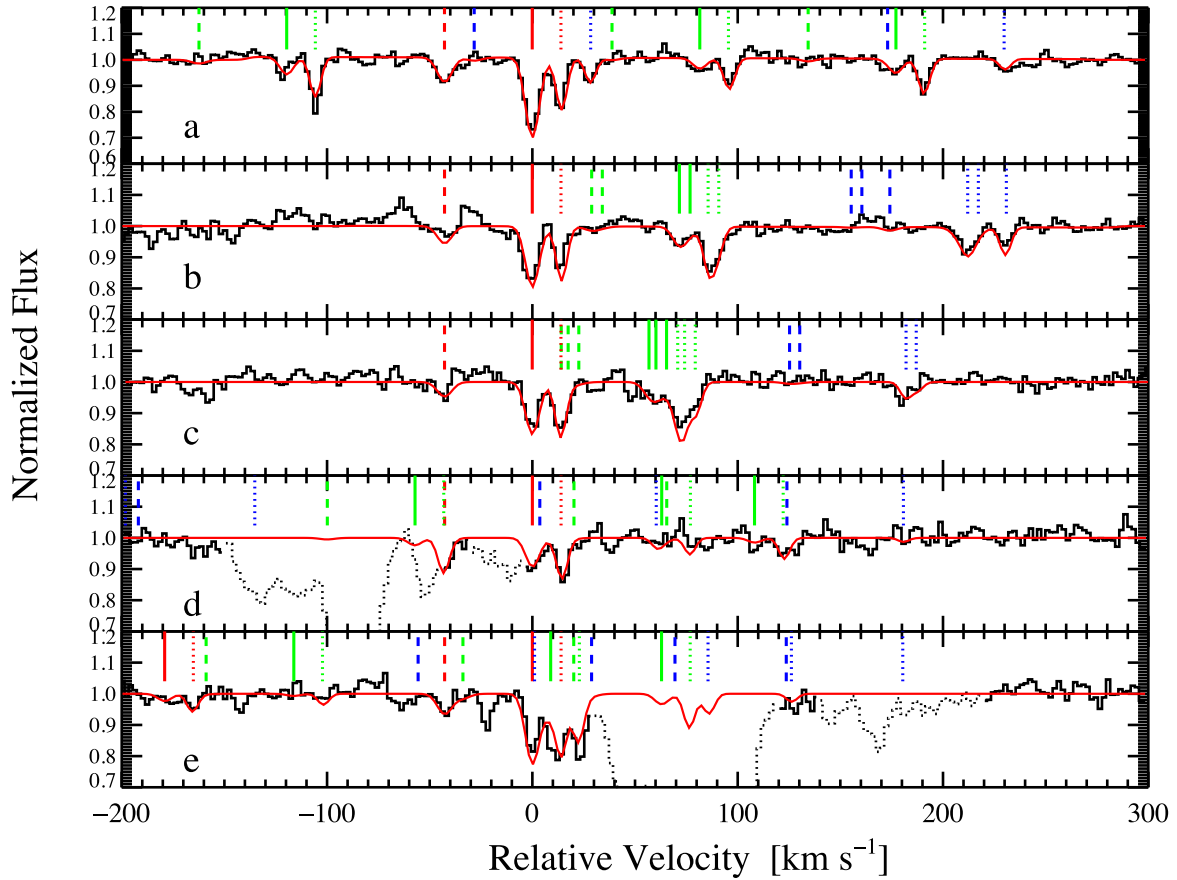


FIG. 1.— DLA 0812+32 CI velocity structure. Spectral regions covering the five CI multiplets used in the analysis of DLA 0812+32: The multiplets are a) 1656Å, b) 1560Å, c) 1328Å, d) 1280Å, and e) 1277Å. Black is the data, red is our fit. The different fine structure transitions are color coded: CI = red, CI* = green, CI** = blue, while the three velocity components are denoted by different linestyles: component 1 at $v \sim -43 \text{ km s}^{-1}$, or $z_{abs} = 2.625808$ is dashed, component 2 at $v = 0 \text{ km s}^{-1}$, or $z_{abs} = 2.6263247$ is solid, while component 3 at $v \sim +14 \text{ km s}^{-1}$, or $z_{abs} = 2.626491$ is dotted. Interloper lines are denoted by dotted black lines.

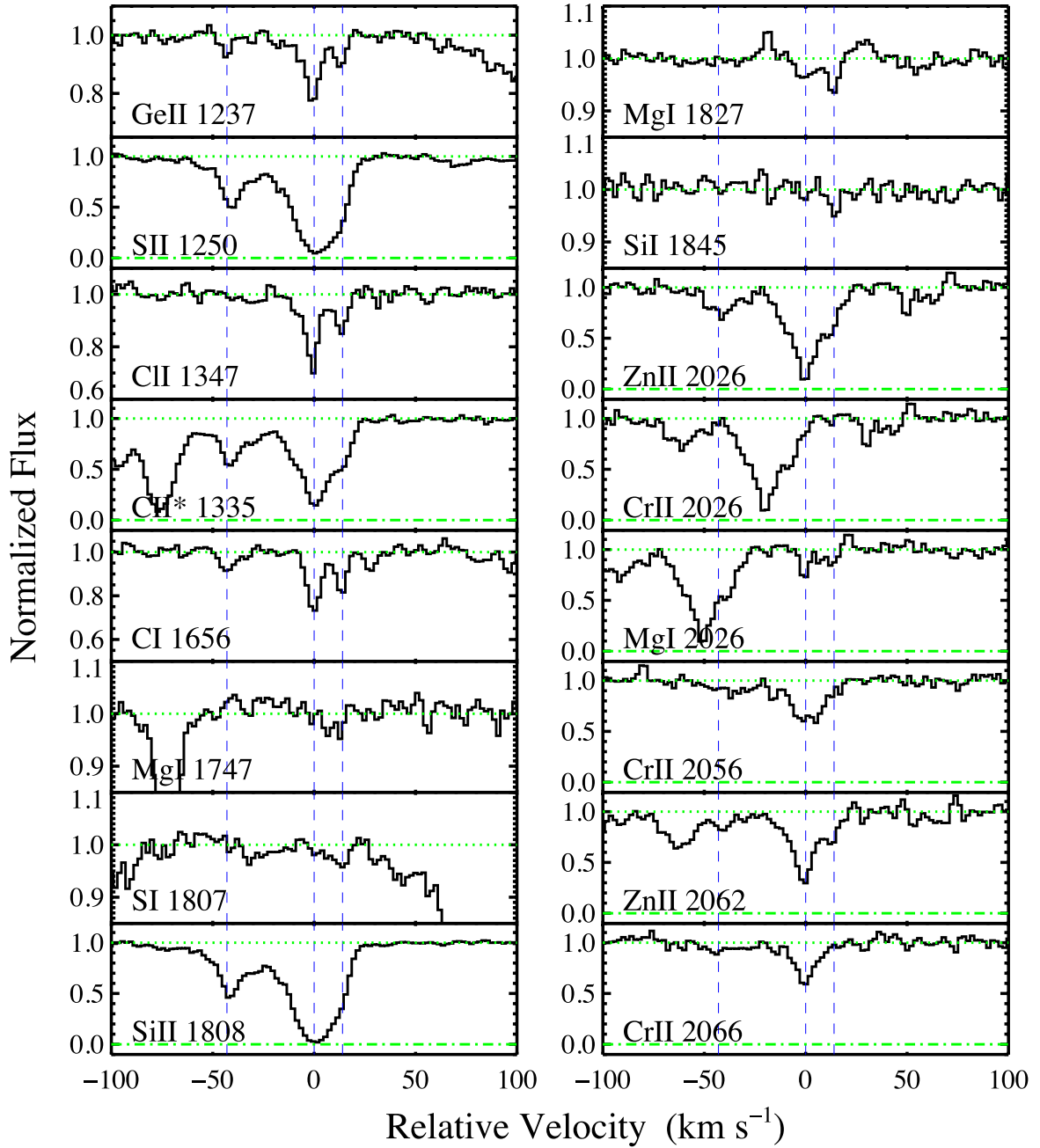


FIG. 2.— DLA 0812+32 low ions. Blue vertical line at $v = 0 \text{ km s}^{-1}$ marks component 2 at $z_{abs} = 2.6263247$, while the narrow Doppler parameter, cold component 3, is located at $+14 \text{ km s}^{-1}$.

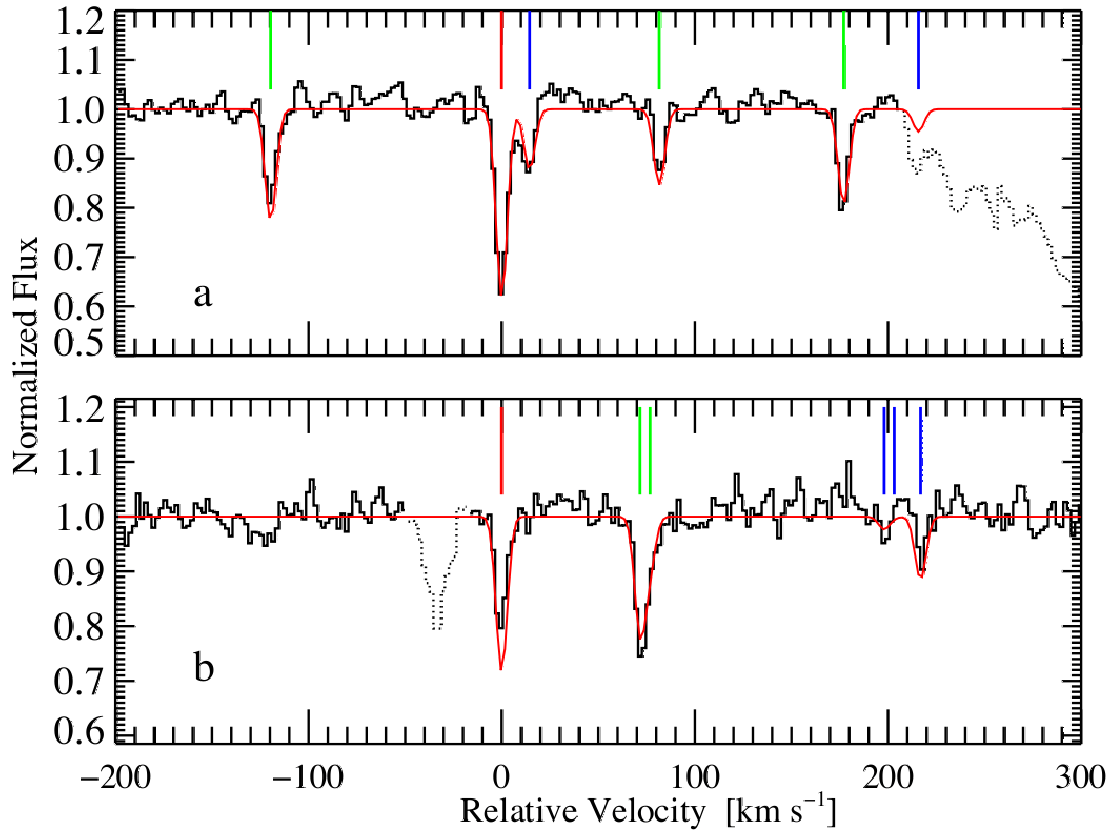


FIG. 3.— DLA 0812+32 $z_{abs}=2.06$ CI velocity structure. Notation is as in Figure 1. Only the 1656Å and 1560Å multiplets were used in the fit because of the serious blending with the Lyman α forest in lower wavelength multiplets. The single CI component is located at $v = 0 \text{ km s}^{-1}$, with $z_{abs} = 2.066780$.

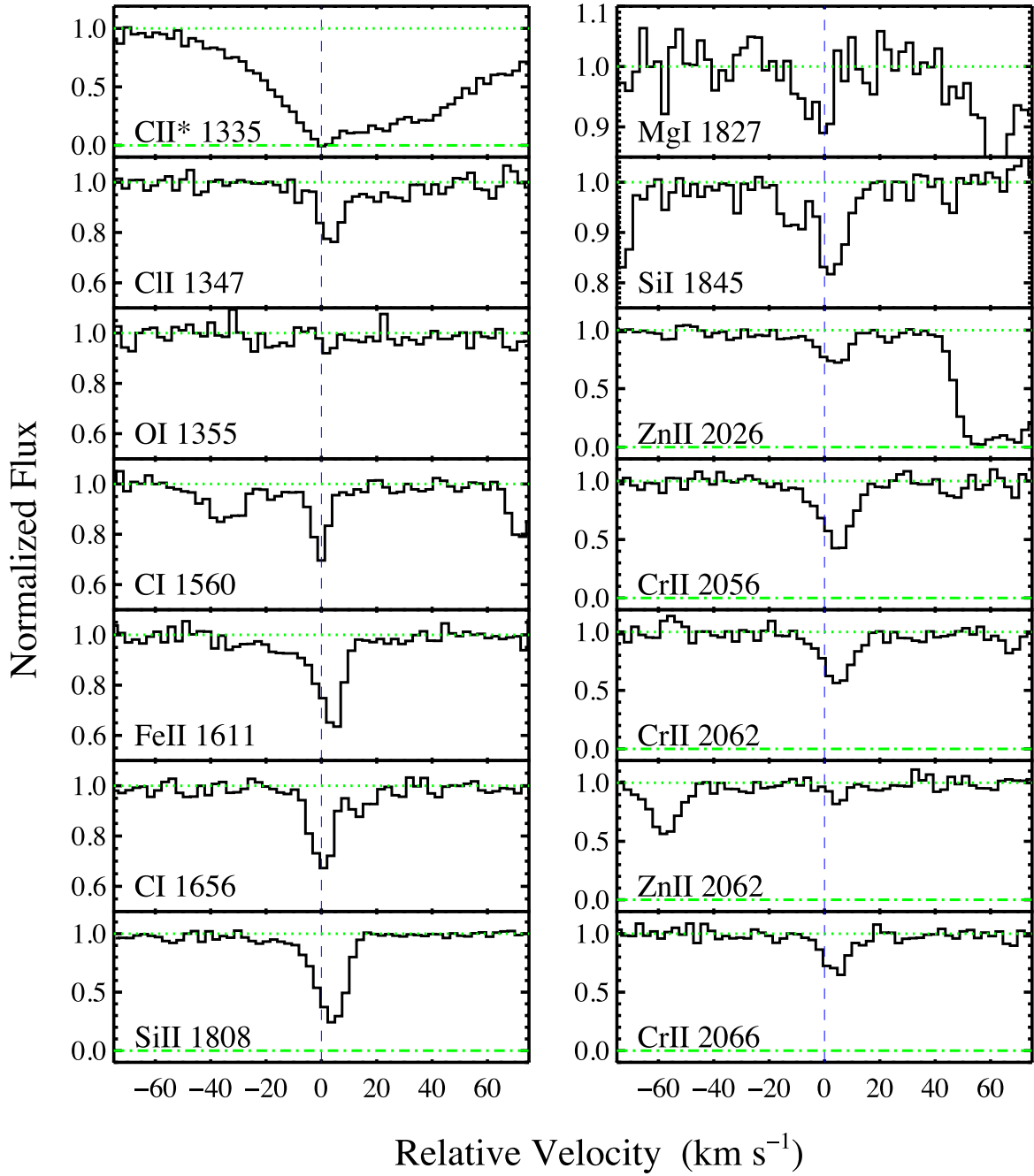


FIG. 4.— DLA 0812+32 $z_{abs}=2.066780$. Note the velocity offset between CI and the other low ions. Also note the blending of CII*.

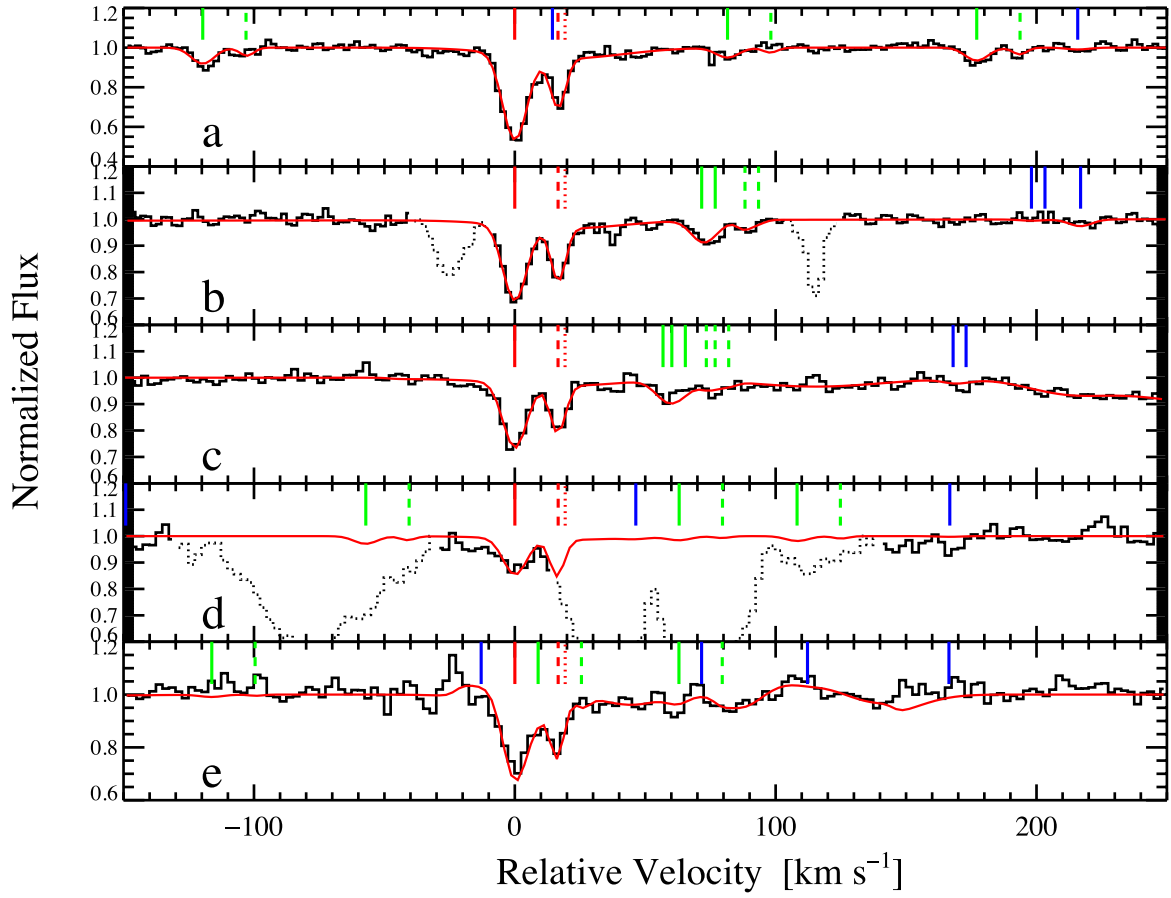


FIG. 5.— Spectral regions covering the five CI multiplets used in the analysis of DLA 1331+17. Notation is as in Figure 1. This system requires 3 CI components: component 1 at $v = 0 \text{ km s}^{-1}$, or $z_{abs} = 1.77637$ is solid, component 2 at $v \sim 17 \text{ km s}^{-1}$, or $z_{abs} = 1.77652$ is dashed, while component 3 at $v \sim 20 \text{ km s}^{-1}$, or $z_{abs} = 1.77659$ is dotted. Interloper lines are denoted by dotted black lines.

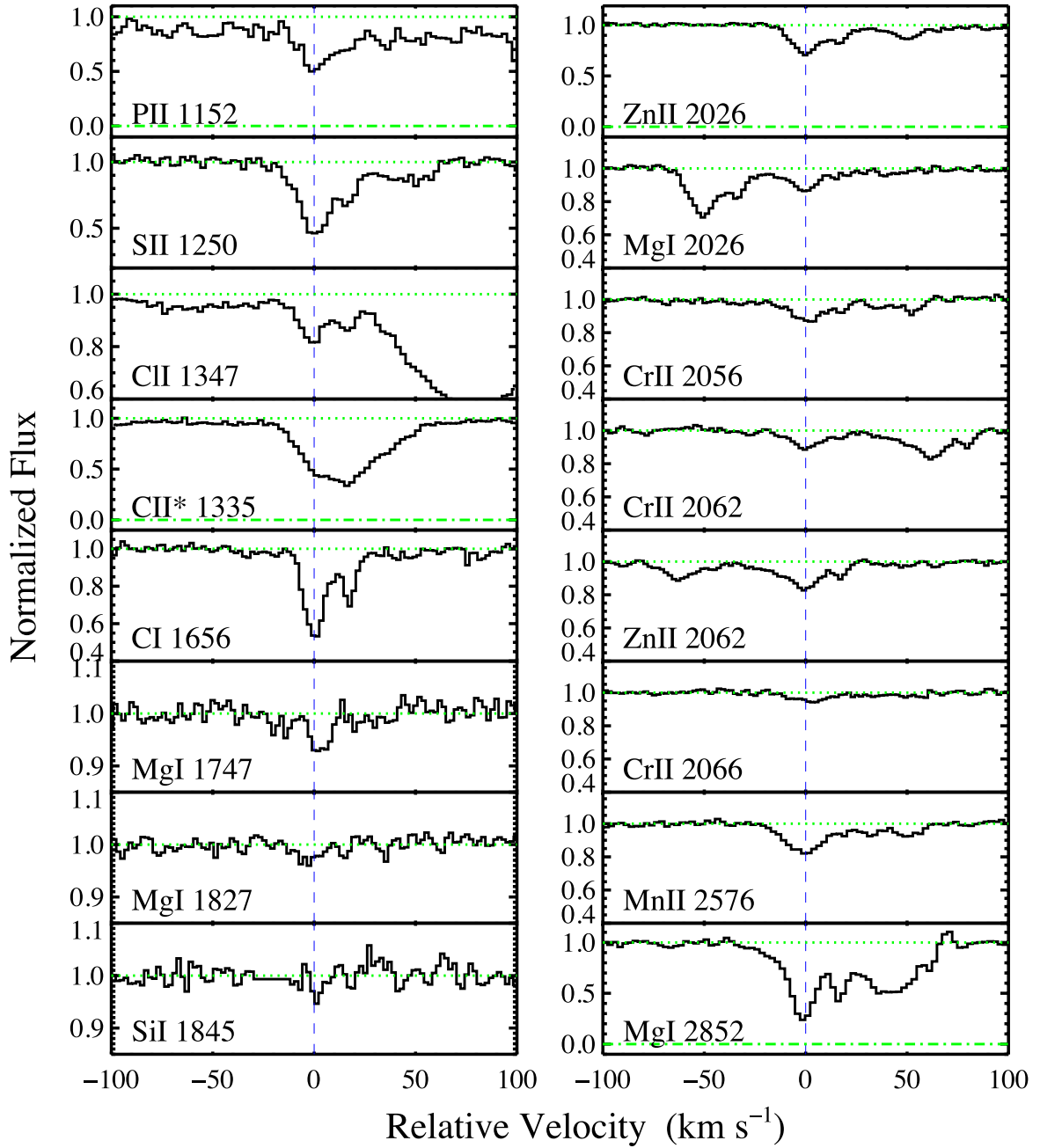


FIG. 6.— Resonance lines and low ions that trace the C I velocity structure of DLA 1331+17. $v = 0 \text{ km s}^{-1}$ located at component 1 at $z_{abs} = 1.77637$. Note that the C II* transitions is likely blended with a forest line due to its different velocity profile.

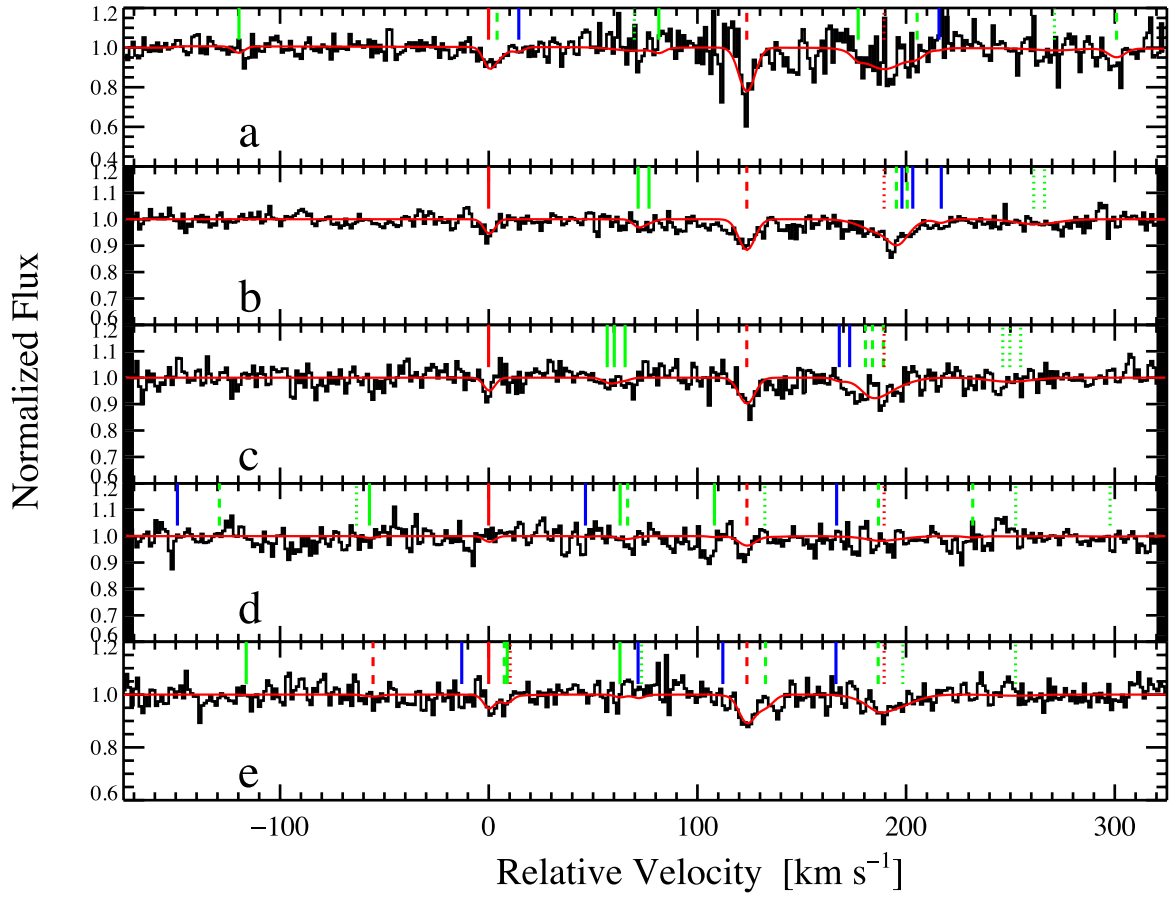


FIG. 7.— Spectra of DLA J2100–06 covering the 1656Å, 1560Å, 1328Å, 1280Å, and 1277Å multiplets. Notation as in Figure 1. The best fit requires three CI velocity components. The lower S/N in 1656Å multiplet (panel a) is due to its proximity to the order gap.

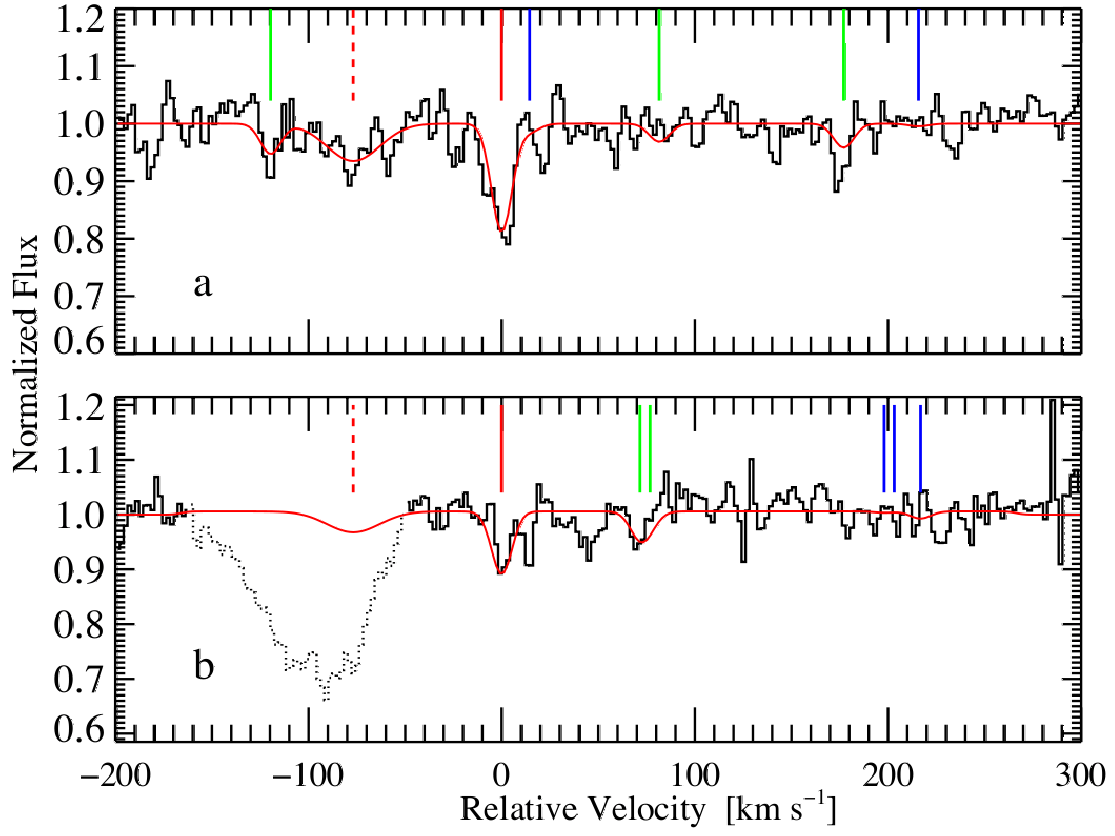


FIG. 8.— Spectra of DLA 2231–00 covering the 1656Å and 1560Å multiplets. Notation as in Figure 1. The best fit requires two C I velocity components: component 1 at $v = -77 \text{ km s}^{-1}$, or $z_{abs} = 2.06534$, with no measurable fine structure lines, and component 2 at $v = 0 \text{ km s}^{-1}$, or $z_{abs} = 2.066122$, with detected C I fine structure lines (however, $N(\text{C I}^{**})$ is technically an upper limit).

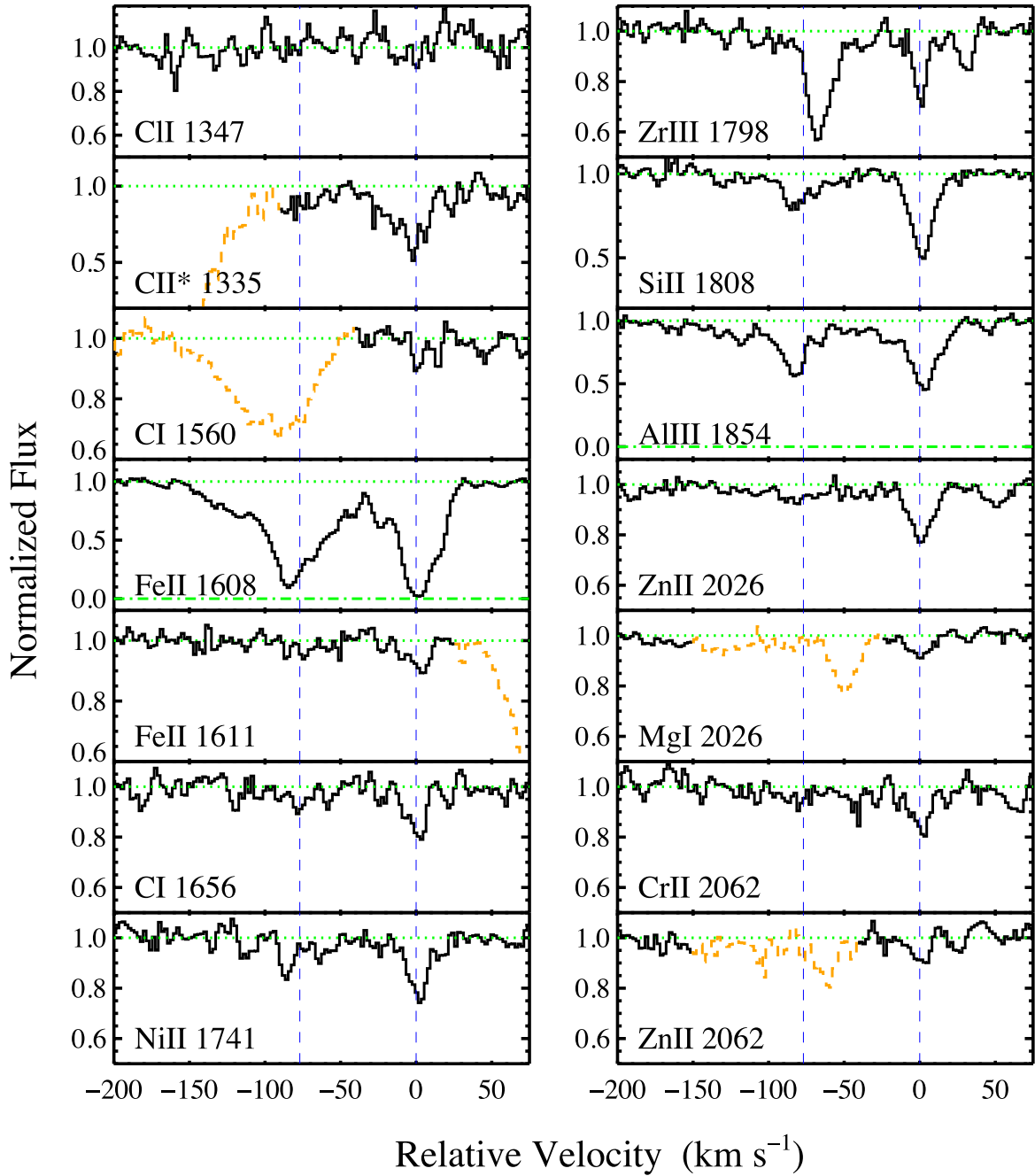


FIG. 9.— Spectra of DLA 2231-00 low ions. $v = 0 \text{ km s}^{-1}$ is located on component 2 at $z_{abs} = 2.066122$ and marked by a vertical dashed blue line. Component 1 is located at $v \approx -77 \text{ km s}^{-1}$.

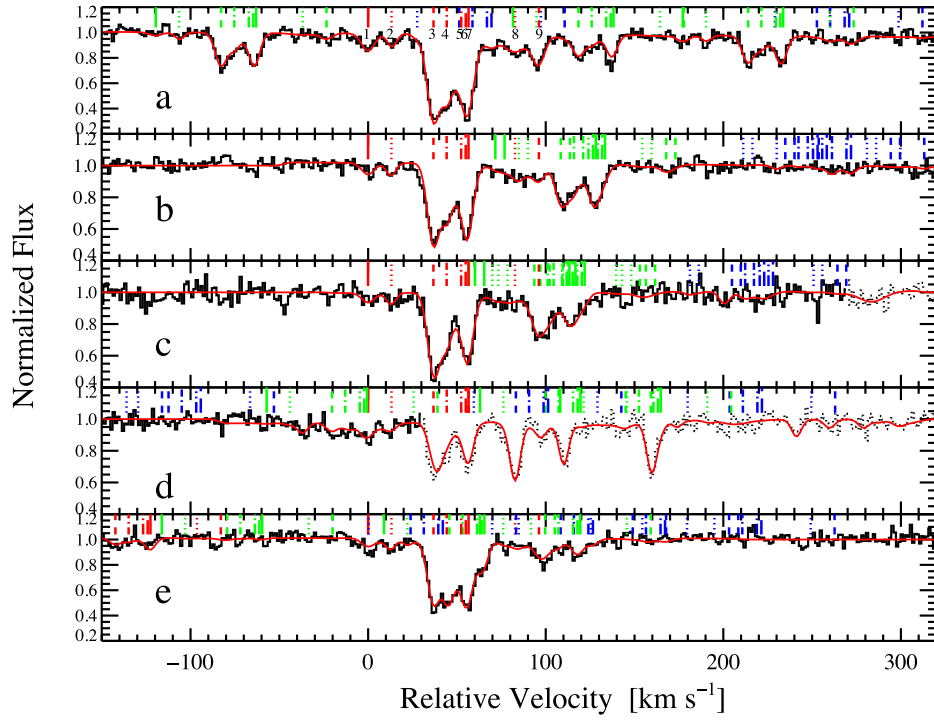


FIG. 10.— J2340 C I velocity profiles over five multiplets, a) 1656Å, b) 1560Å, c) 1328Å, d) 1280Å, e) 1277Å. Notation is as in Figure 1. The components are labeled in (a), as 1 – 9 from lowest to highest relative redshift (relative to the arbitrarily chosen $v = 0 \text{ km s}^{-1}$ at $z_{abs} = 2.054151$) and located at the following velocities: $v \sim 0 \text{ km s}^{-1}$, 13 km s^{-1} , 37 km s^{-1} , 44 km s^{-1} , 52 km s^{-1} , 55 km s^{-1} , 57 km s^{-1} , 83 km s^{-1} , and 96 km s^{-1} .

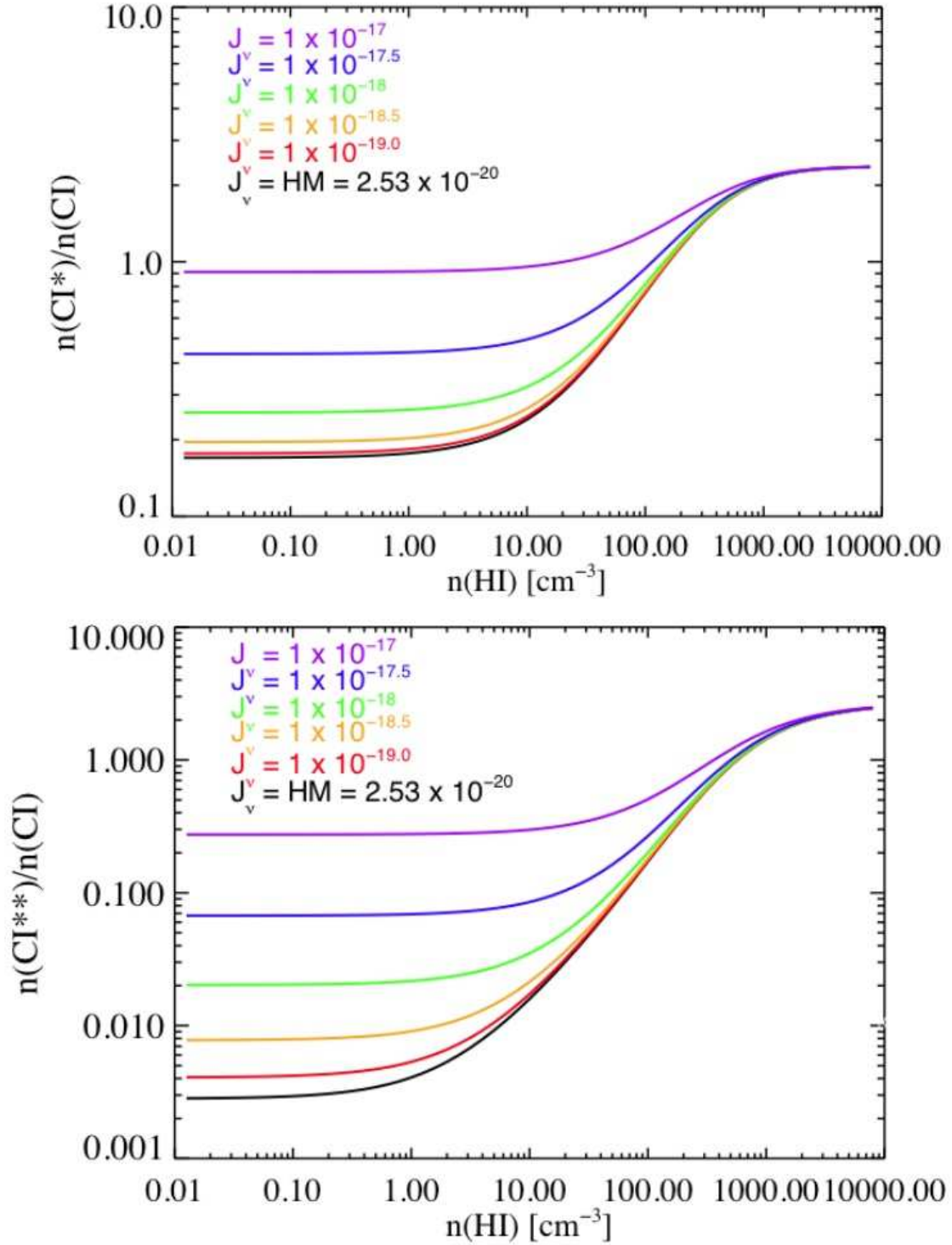


FIG. 11.— Excitation of the fine structure level CI^* (top) and CI^{**} (bottom) caused by increasing the strength of the radiation field. We plot the ratio $\frac{n(CI^*)}{n(CI)}$ and $\frac{n(CI^{**})}{n(CI)}$ and have included spontaneous radiative decay, excitation by the CMB at $z_{abs}=2$, and collisions with neutral hydrogen at a temperature of $T=100K$. HM is the value of the Haardt-Madau background at $z = 2$ and is therefore a minimum total radiation field. Note that the radiation field must be $\sim \geq 1 \times 10^{-18.5}$ ergs $cm^{-2} s^{-1} Hz^{-1} sr^{-1}$ in order to cause significant effects to the level populations of the CI fine structure states at low densities (i.e. when collisions are not the dominant mechanism).

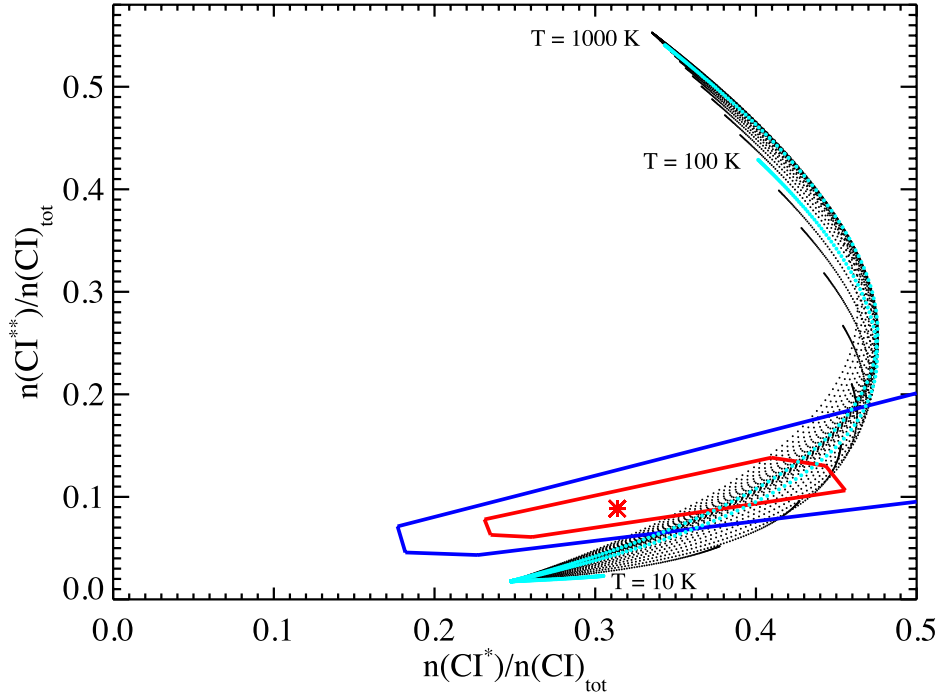


FIG. 12.— f_1 versus f_2 for component 3 of DLA 0812+32, where $f_1 = n(\text{CI}^*)/n(\text{CI})_{\text{tot}}$, $f_2 = n(\text{CI}^{**})/n(\text{CI})_{\text{tot}}$, and $n(\text{CI})_{\text{tot}} = n(\text{CI}) + n(\text{CI}^*) + n(\text{CI}^{**})$. The data point is marked by a red asterisk and the 1σ error polygon is marked in red, while the 2σ error polygon is blue. Theoretical tracks are indicated by black points and run from $T = 10 - 10,000$ K and $n(\text{H I}) = 10^{-3.5} - 10^{4.1} \text{ cm}^{-3}$. For clarity we have highlighted the tracks corresponding to $T = 10, 100$ and 1000 K in cyan.

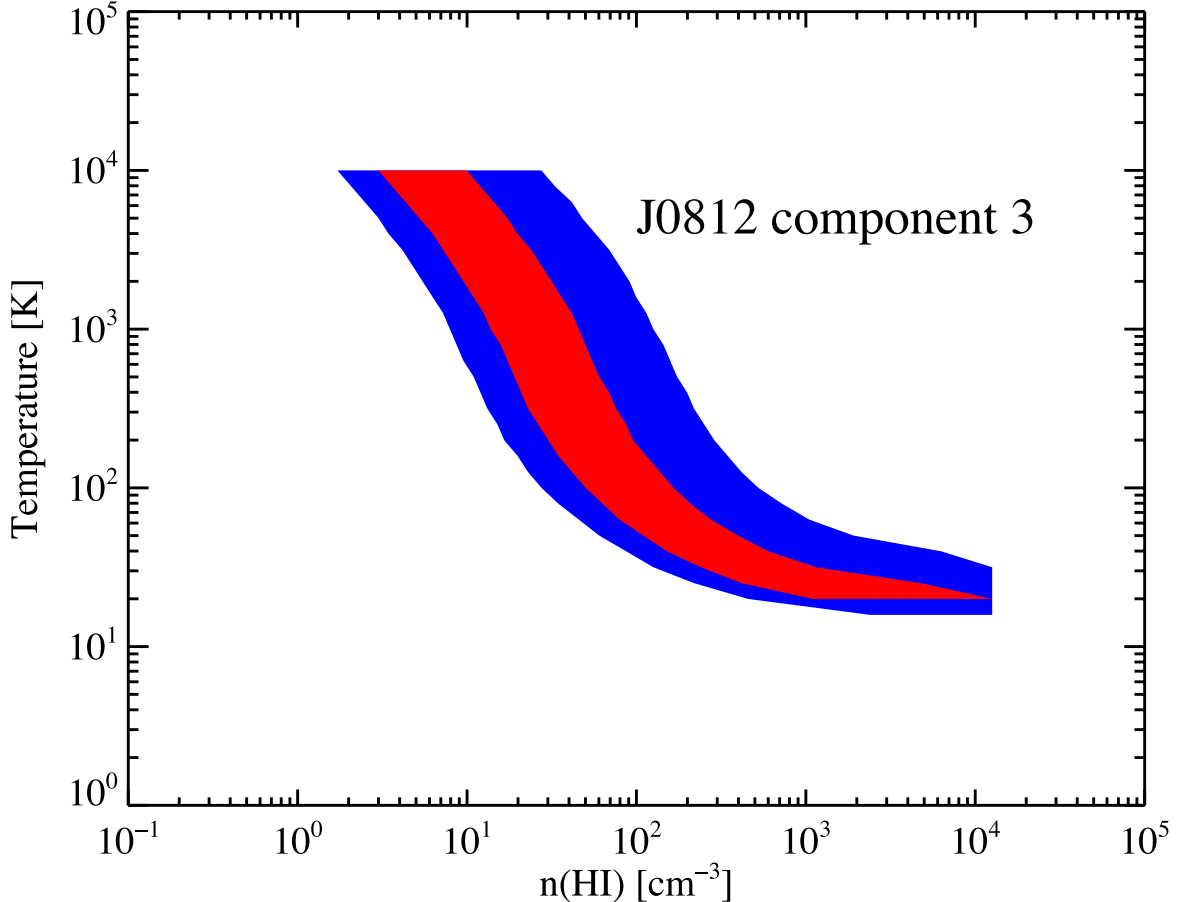


FIG. 13.— $n(\text{H I})$ versus temperature for the allowed solutions of DLA 0812+32 component 3 from the C I analysis. 1σ results are in red while 2σ is in blue.

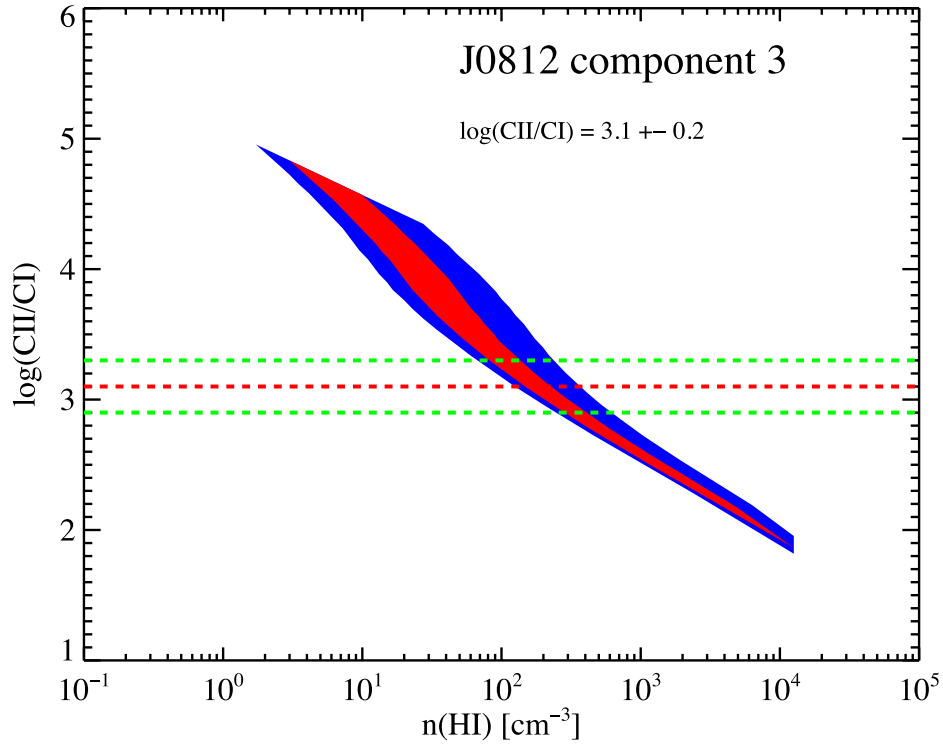


FIG. 14.— $n(\text{H I})$ versus $\frac{n(\text{C II})}{n(\text{C I})}$ for the allowed solutions of DLA 0812+32 component 3. The measured $\frac{n(\text{C II})}{n(\text{C I})}$ is indicated by the red dashed line with green dashed lines indicating the errors of ± 0.2 dex. 1σ results are in red while 2σ is in blue.

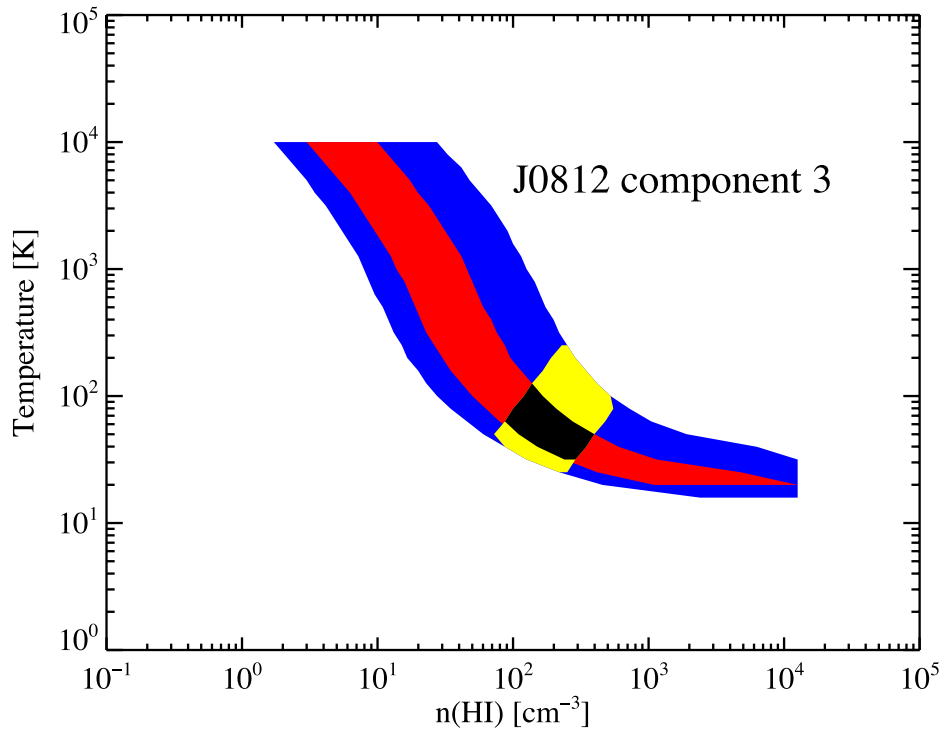


FIG. 15.— $n(\text{H I})$ versus temperature for the allowed solutions of DLA 0812+32 component 3. The final solutions, as constrained by $\frac{\text{C II}}{\text{C I}}$, are shown in black (1σ) and yellow (2σ).

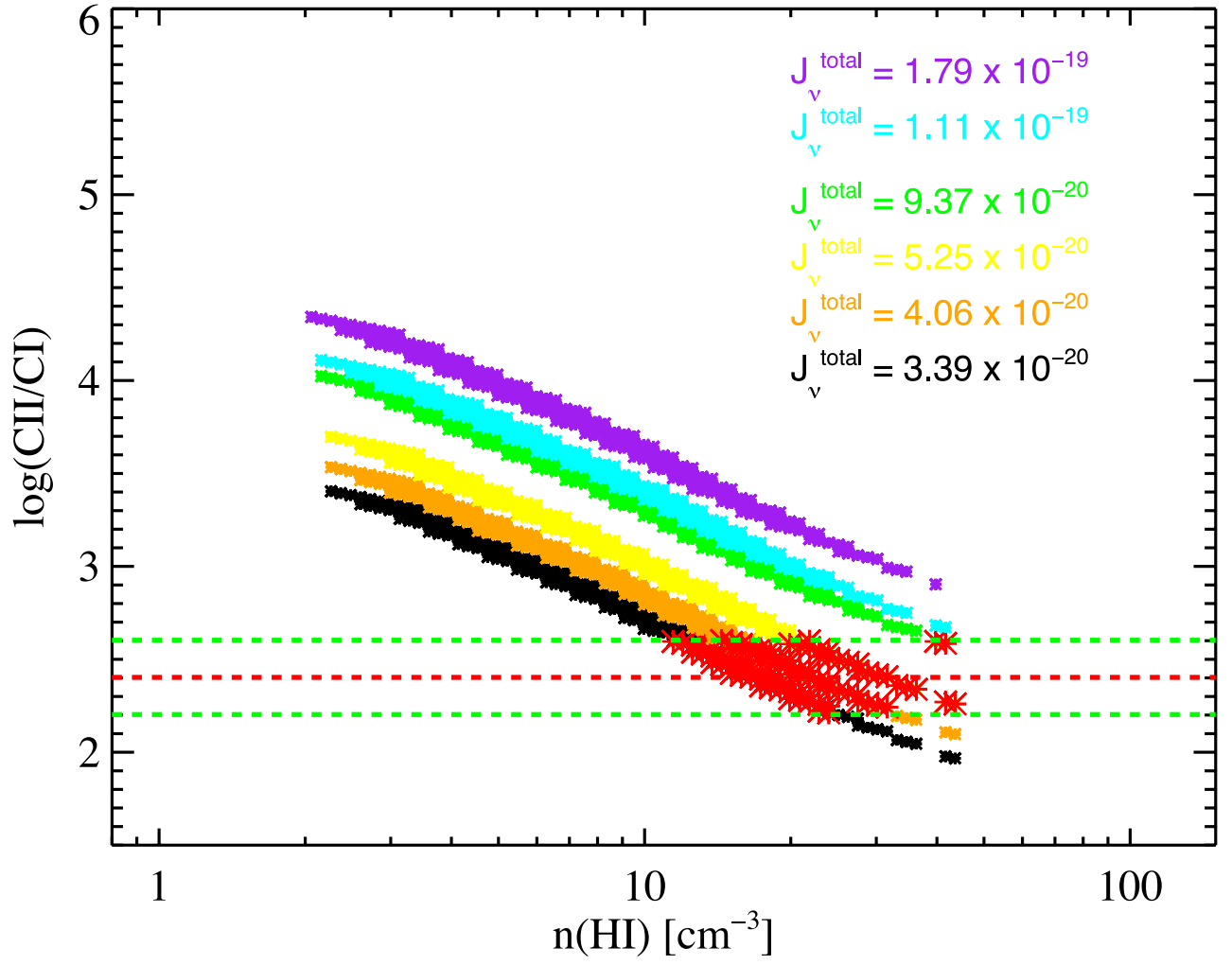


FIG. 16.— Example of a case, shown here for DLA 1331+17, component 1, where it is possible to constrain the radiation field using only the C I fine structure states and the assumption of ionization equilibrium. $\log(\frac{C II}{C I})$ versus $n(\text{H I})$ for a selection of J_ν values. Solutions falling within the allowed range of $\log(\frac{C II}{C I})$ are marked in red. It is seen that for $J_\nu^{total} \geq \sim 1 \times 10^{-19}$ ergs $\text{cm}^{-2} \text{s}^{-1} \text{Hz}^{-1} \text{sr}^{-1}$, there are no acceptable solutions. Note: This is for the 1σ C I solutions and the value of the Haardt-Madau background for this object is 2.53×10^{-20} ergs $\text{cm}^{-2} \text{s}^{-1} \text{Hz}^{-1} \text{sr}^{-1}$. It is also apparent that the range of allowed densities is constrained to be $10 \leq n \leq 50 \text{ cm}^{-3}$.

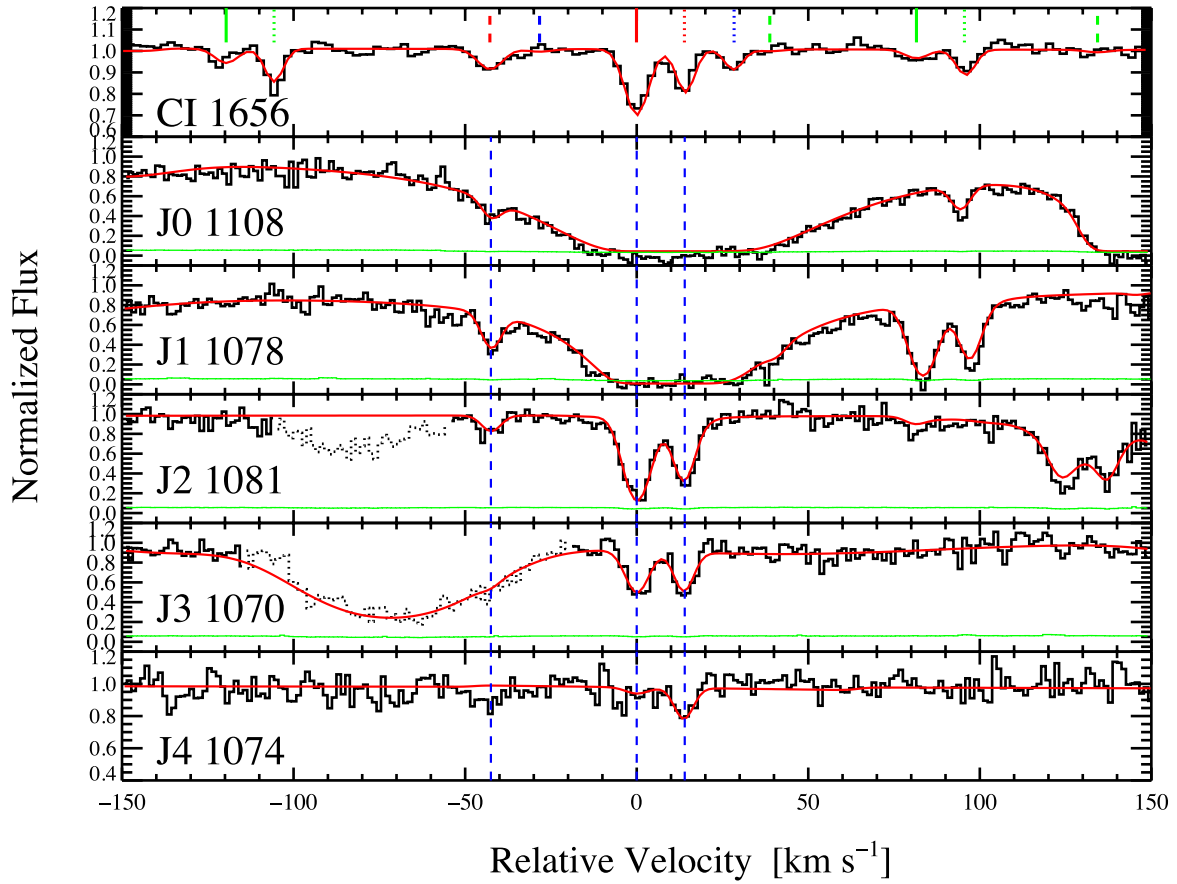
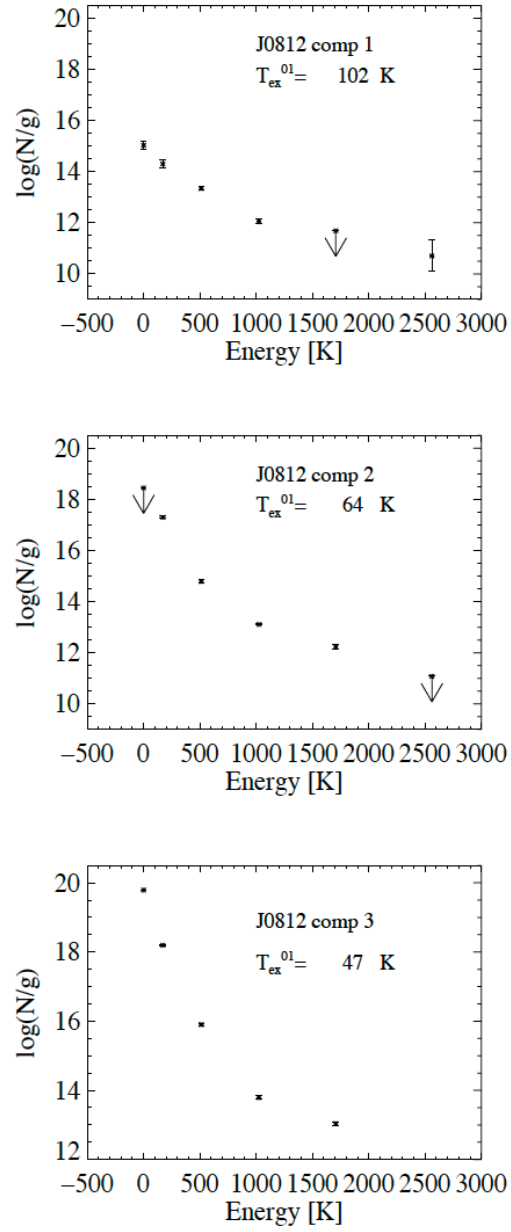


FIG. 17.— Examples of the H_2 absorption in DLA 0812+32. We show the relatively unblended sections here (blends are denoted by dotted lines) over several rotational J levels. Blue vertical dashed lines mark the three H_2 components, from left to right, components 1, 2, 3. The close association with the three CI components is clear.

FIG. 18.— H_2 excitation diagrams for the components of DLA 0812+32.

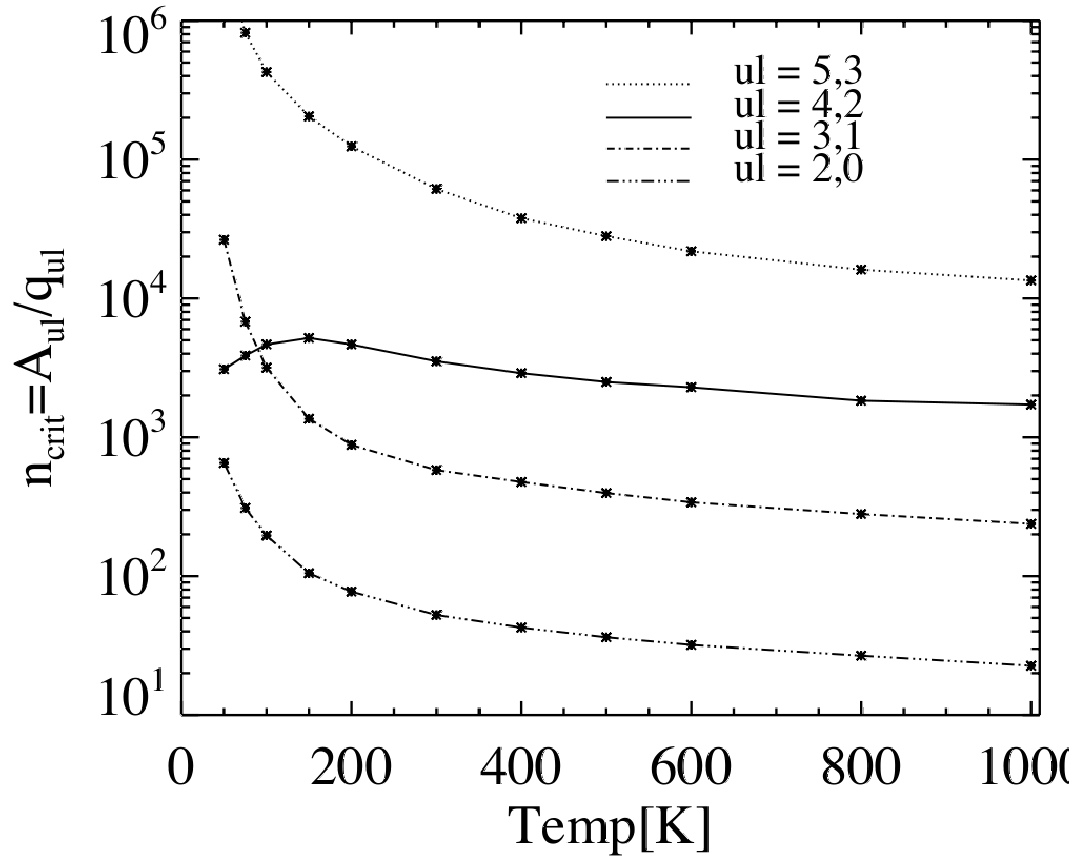


FIG. 19.— Critical densities as a function of temperature for the H_2 rotational J states. The subscripts u and l denote upper and lower respectively.

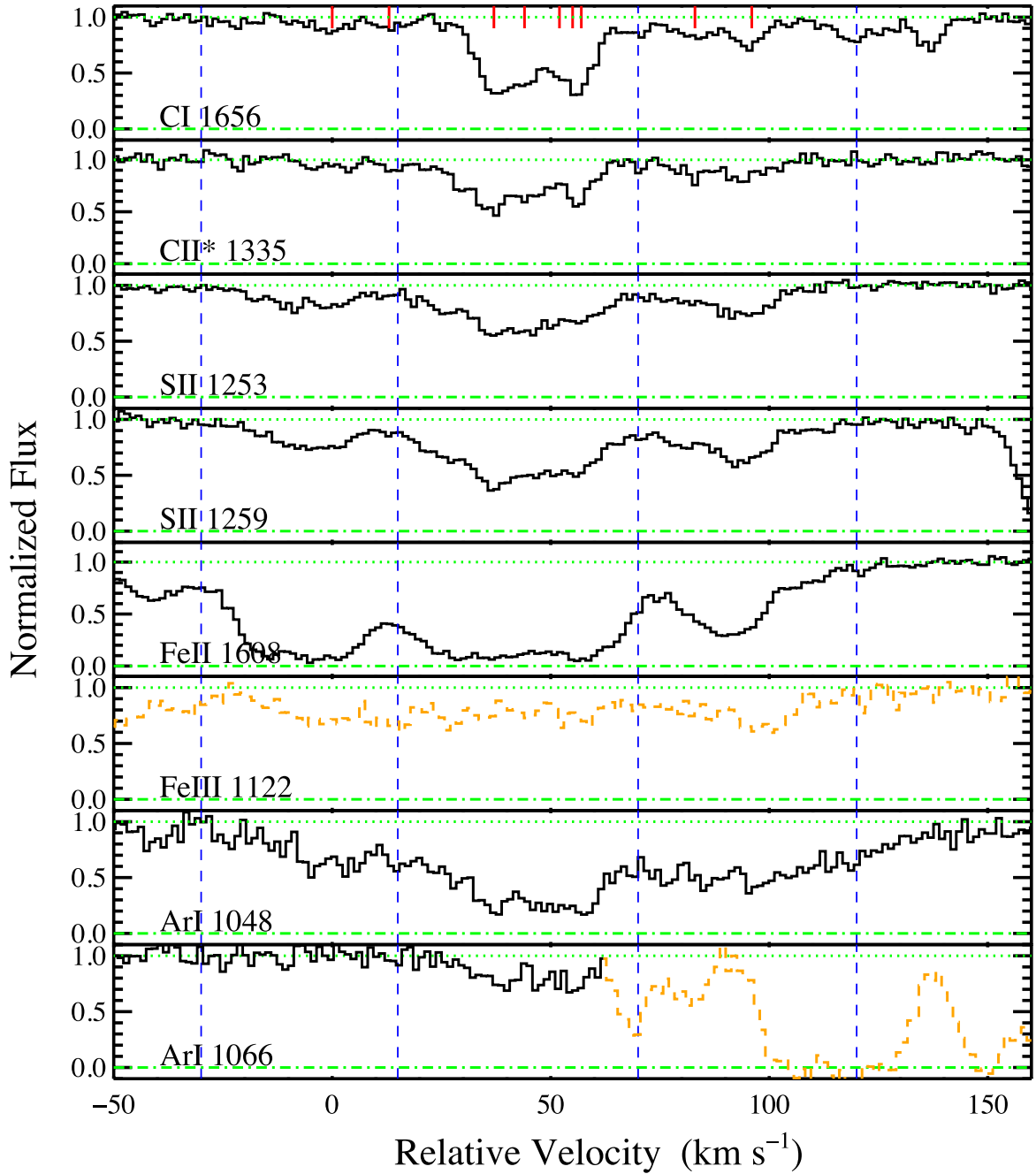


FIG. 20.— DLA 2340–00 low ions, Fe III and Ar I. Blends are indicated by orange dashed lines. The velocity space defining the three super-components a, b, and c are separated by vertical blue dashed lines. Relative to $v = 0$ at $z_{abs} = 2.054151$, super-component (a) is from $-30 - 15 \text{ km s}^{-1}$, super-component (b) from $15 - 70 \text{ km s}^{-1}$, and super-component (c) from $70 - 120 \text{ km s}^{-1}$. For reference, the 9 C I velocity components are indicated by red vertical tick marks.

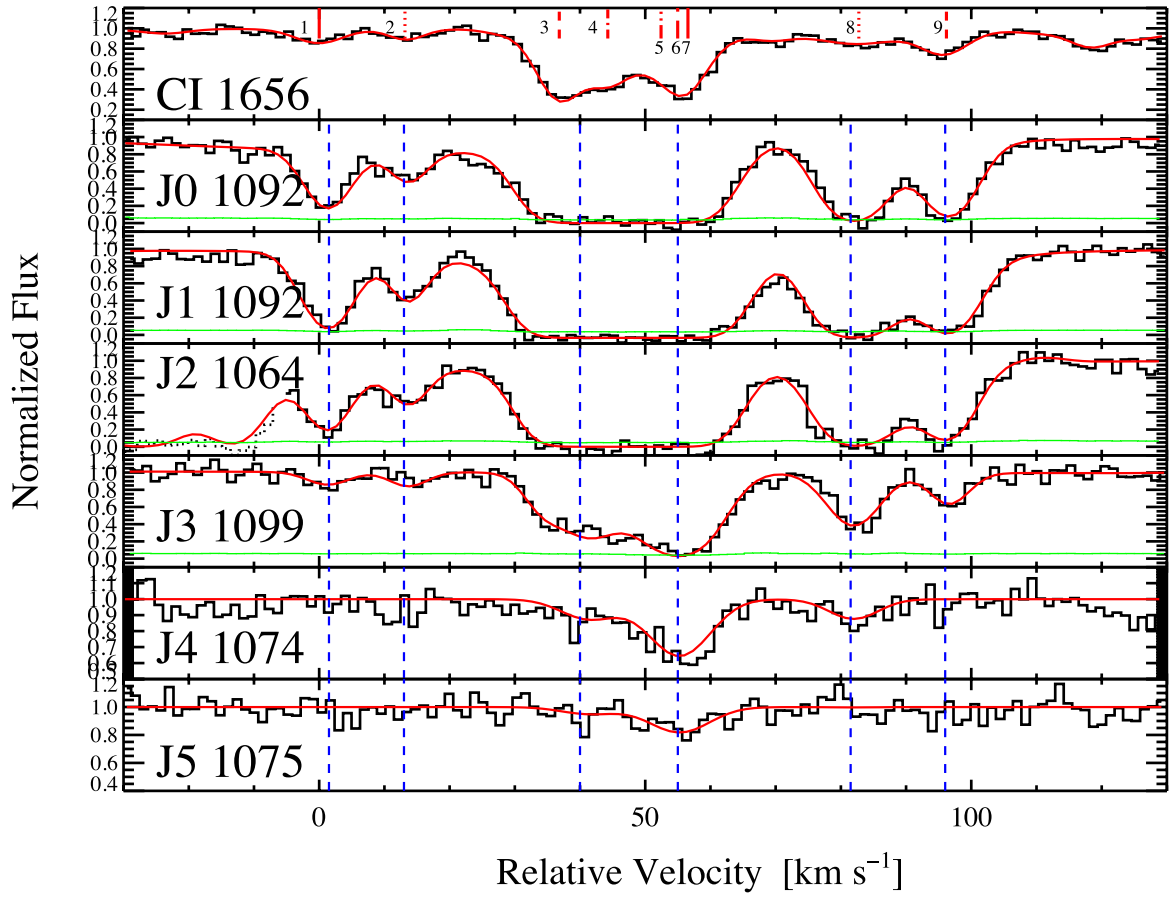
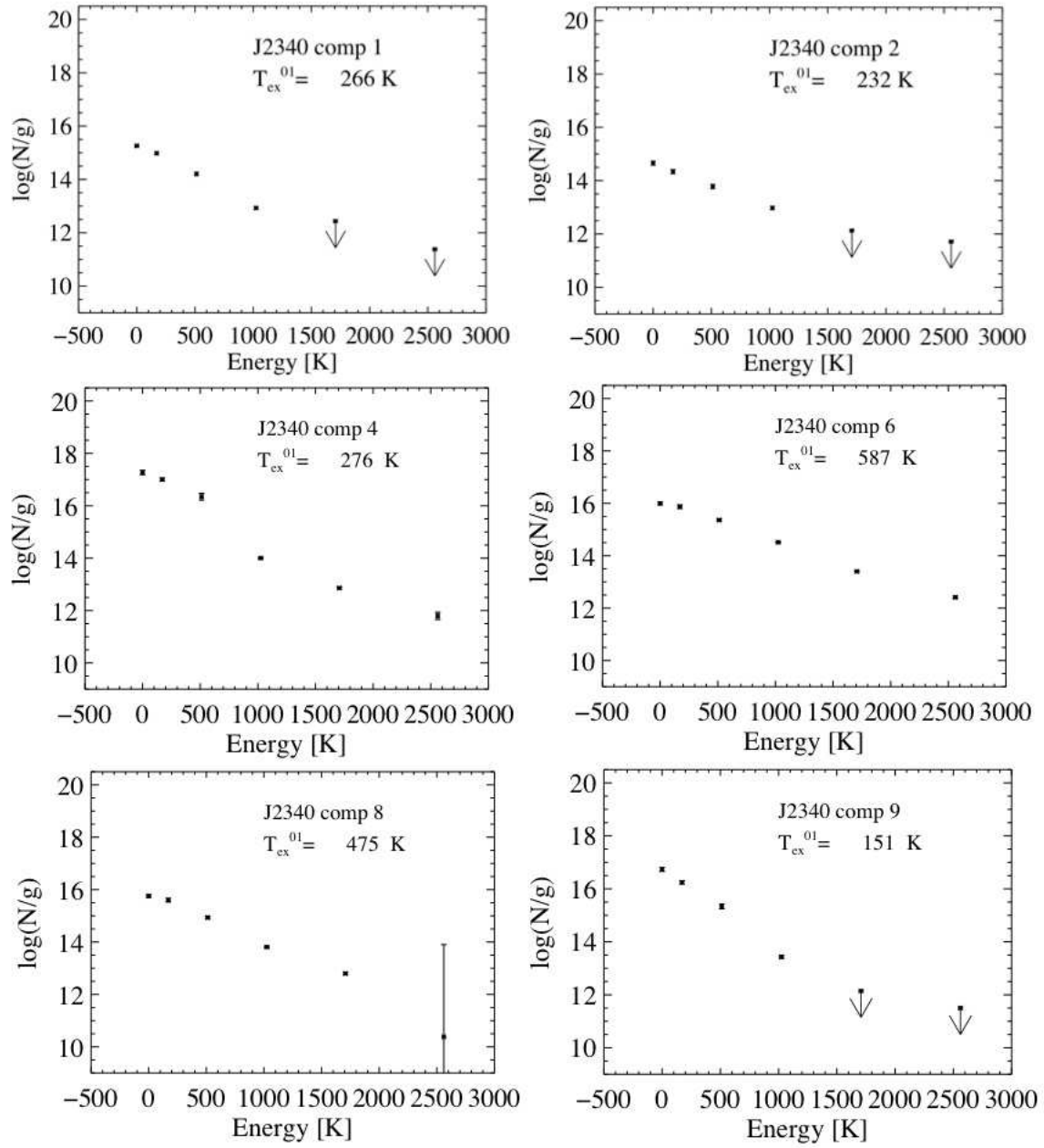


FIG. 21.— Examples of the H₂ absorption in DLA 2340–00. We show the relatively unblended sections here (blends are denoted by dotted lines) over several rotational J levels. Blue vertical dashed lines mark the six H₂ components we call components 1, 2, 4, 6, 8 and 9.

FIG. 22.— The H_2 excitation diagrams for the 6 components of DLA 2340 -00 that contain H_2 .

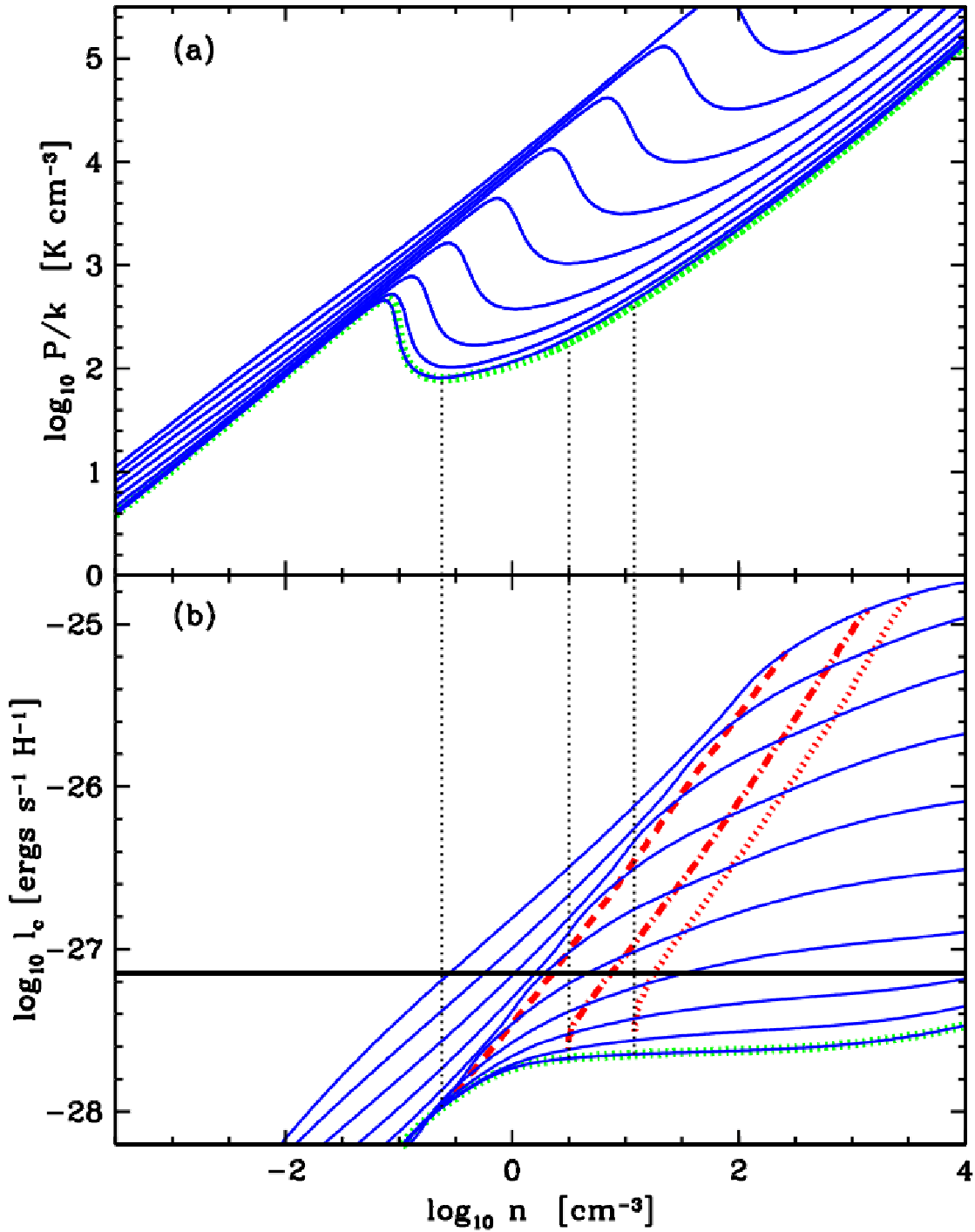


FIG. 23.— Pressure curves and star formation rate solutions for DLA 1331+17. The blue model curves for different star formation rates represent $\log \Sigma_{SFR} = -\infty, -4, -3.5, \dots, 0.0$. The CNM P_{min} , P_{eq} and P_{max} solutions are indicated by the red dashed lines. Vertical, black dotted lines illustrate the location of the CNM stable points associated with, from left to right, P_{min} , P_{geo} and P_{max} for the case of background radiation only.

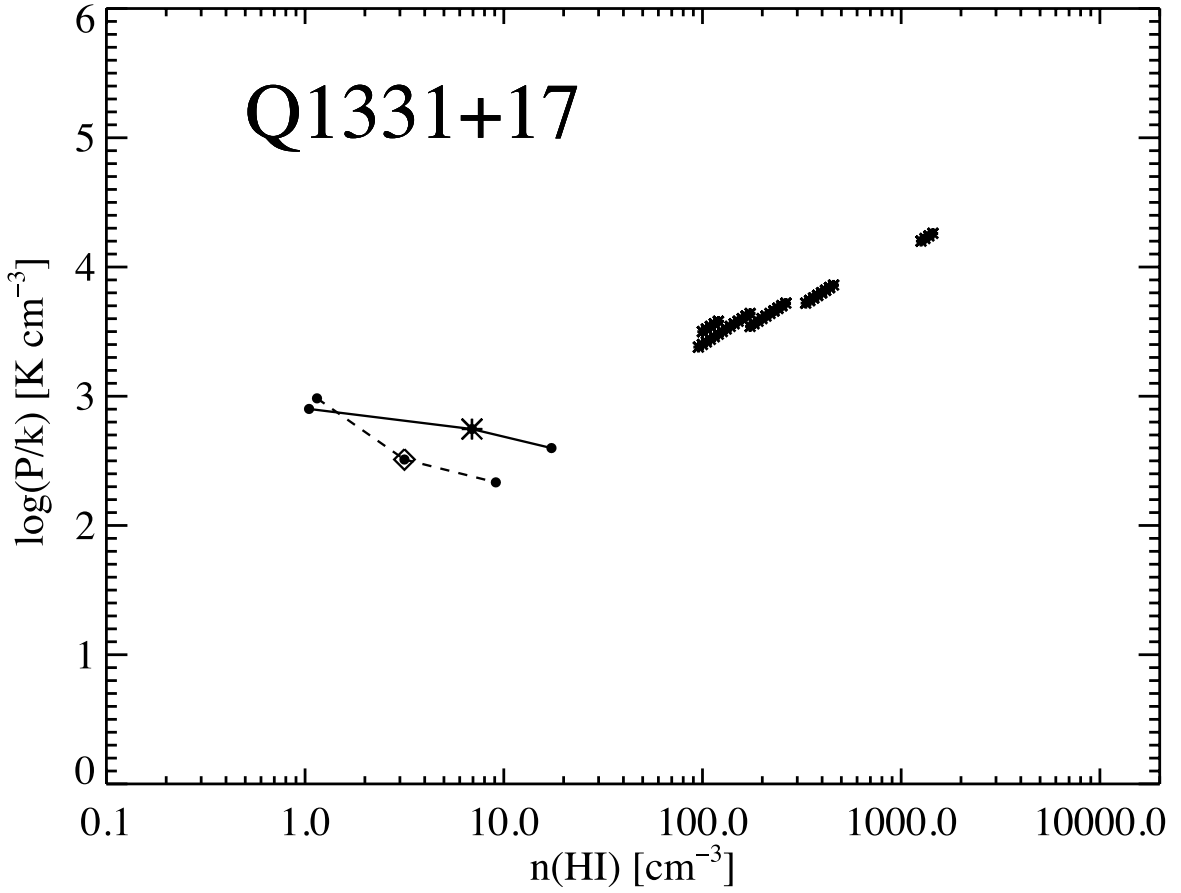


FIG. 24.— DLA 1331+17 2σ range of solutions for range of CII* technique solutions. The minimal depletion CII* solution is indicated by the asterik, with P_{min} and P_{max} denoted by points at the ends of attached lines, while the maximal depletion model is denoted by a diamond, and the P_{min} and P_{max} at the ends of dashed lines. For comparison, the full range of CI solutions are given as a grouping of points in the upper right. It is clear that these fall at higher pressures and densities than than the CII* results.

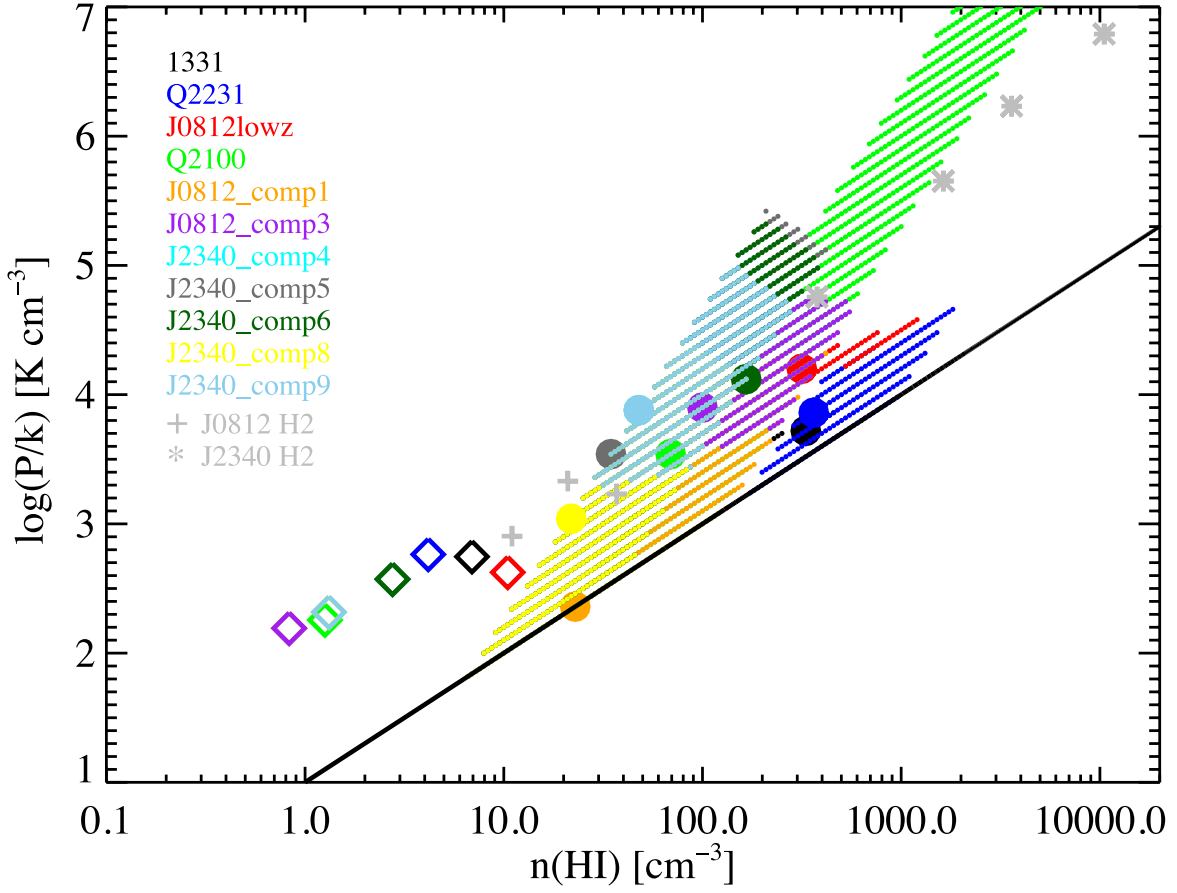


FIG. 25.— Summary of all DLAs, compared with the results of the CII* technique (diamonds). The 2σ CI results are the shaded regions, and the best-fit (minimized χ^2) for each is marked by a filled circle. It is clear that the CI results are consistently higher in density and therefore pressure. Note, some regions/solutions are overlapping. The H₂ derived pressures are denoted by light grey crosses and asterisks for components in DLA 0812+32 and DLA 2340–00 respectively. The solid black line denotes $T = 10$ K. The resulting median values for the CI sample are: $\langle n(\text{H I}) \rangle = 69 \text{ cm}^{-3}$, $\langle T \rangle = 50 \text{ K}$, and $\langle \log(P/k) \rangle = 3.86 \text{ cm}^{-3} \text{ K}$, with standard deviations, $\sigma_{n(\text{H I})} = 134 \text{ cm}^{-3}$, $\sigma_T = 52 \text{ K}$, and $\sigma_{\log(P/k)} = 3.68 \text{ cm}^{-3} \text{ K}$. This can be compared with the global CII* technique median values for the same DLAs: $\langle n(\text{H I}) \rangle = 2.8 \text{ cm}^{-3}$, $\langle T \rangle = 139 \text{ K}$, and $\langle \log(P/k) \rangle = 2.57 \text{ cm}^{-3} \text{ K}$, with standard deviations $\sigma_{n(\text{H I})} = 3.0 \text{ cm}^{-3}$, $\sigma_T = 43 \text{ K}$, and $\sigma_{\log(P/k)} = 0.22 \text{ cm}^{-3} \text{ K}$.

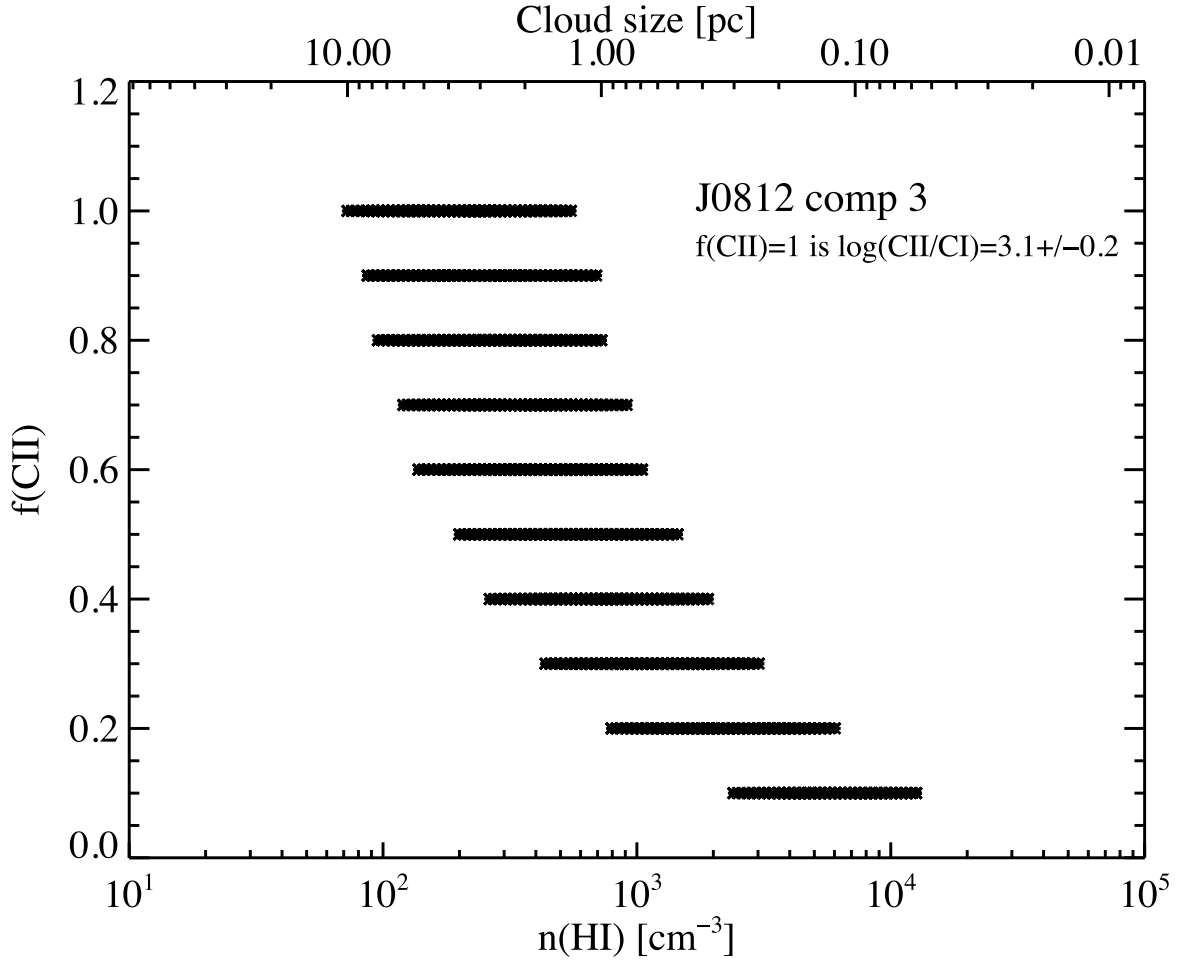


FIG. 26.— The resultant cloud size in pc (top axis) as a function of the fraction of C II, $f(\text{C II})$, associated with the C I cloud. Here, $f(\text{C II}) = 1$ means that 100% of the measured $N(\text{C II})$ is associated with the C I cloud. In this case, for DLA 0812+32, component 3, $\log(\frac{\text{C II}}{\text{C I}}) = 3.1 \pm 0.2$. As the fraction of associated C II decreases, the $n(\text{H I})$ increases and hence, the resultant cloud size decreases.

TABLE 1
 DETAILS OF OBSERVATIONS

Quasar	Telescope/Instrument	Date	Resolution FWHM [km s ⁻¹]	Total Exp. Time [s]
FJ0812+32	Keck/HIRES	Mar. 16/17, 2005	8.33	14400
FJ0812+32	Keck/HIRES	Jan. 12, 2008	6.25	7200
Q1331+17	Keck/HIRES	Jan. 10, 1994	6.25	3600
Q1331+17	VLT/UVES	Dec. 18, 2001	7.0	4500
J2100-06	Keck/HIRES	Sept. 18, 2007	6.25	10800
Q2231-00	Keck/HIRES	Jan. 11, 1995	8.33	5400
J2340-00	Keck/HIRES	Aug. 18/19, 2006	6.25	15000

 TABLE 2
 CI DATA

Quasar	cmp	z_{abs}	FWHM _{inst} ^a [km s ⁻¹]	b [km s ⁻¹]	logN(CI) [cm ⁻²]	logN(CI*) [cm ⁻²]	logN(CI**) [cm ⁻²]	T _{ex} ^{01b} [K]	(f1, f2) ^c
FJ0812+32	1	2.066780(7)	6.25/8.33	1.20 ± 0.14	12.96 ± 0.04	12.92 ± 0.02	12.35 ± 0.04	19.8	(0.43, 0.11)
FJ0812+32	1	2.625808(2)	6.25/8.33	3.25 ± 1.00	12.13 ± 0.05	11.68 ± 0.16	11.37 ± 0.270	11.1	(0.23, 0.11)
FJ0812+32	2	2.6263247(8)	...	2.57 ± 0.56	12.70 ± 0.02	12.32 ± 0.04	<12.39(1σ)	12.0	(0.22, 0.26) ^d
FJ0812+32	3	2.626491(1)	...	0.33 ^e ± 0.05	13.30 ± 0.23	13.02 ± 0.03	12.47 ± 0.05	13.5	(0.31, 0.09)
Q1331+17	1	1.7763702(9)	6.25/7.0	5.08 ± 0.24	13.08 ± 0.02	12.59 ± 0.02	11.90 ± 0.14	10.6	(0.23, 0.05)
Q1331+17	2	1.776524(1)	...	0.55 ± 0.13	13.06 ± 0.13	12.05 ± 0.07	<11.7	6.9 ^f	-
Q1331+17	3	1.77664(5)	...	24.45 ± 6.2	12.51 ± 0.11	<12.2	<12.25	<13.0	-
Q2100-06	1	3.089776(7)	6.25	0.20 ± 0.3	12.28 ± 0.21	12.01 ± 0.13	11.56 ± 0.28	13.7	(0.31, 0.11)
Q2100-06	2	3.091463(4)	...	3.89 ± 0.69	12.57 ± 0.03	12.31 ± 0.08	-	13.9	-
Q2100-06	3	3.09236(2)	...	12.77 ± 1.84	12.61 ± 0.05	12.16 ± 0.12	-	11.1	-
Q2231-00	1	2.06534(3)	8.33	19.08 ± 4.37	12.55 ± 0.08	-	-	-	-
Q2231-00	2	2.066122(5)	...	5.36 ± 1.17	12.65 ± 0.05	12.41 ± 0.09	11.60 ± 0.16	14.3	(0.35, 0.05)
J2340-00	1	2.054151(4)	6.25	3.36 ± 0.80	12.32 ± 0.04	11.96 ± 0.12	-	12.2	-
J2340-00	2	2.054285(3)	...	0.24 ± 0.12	12.54 ± 0.17	12.28 ± 0.09	11.84 ± 0.14	13.9	(0.32, 0.11)
J2340-00	3	2.054526(1)	...	2.55 ± 0.16	13.33 ± 0.02	12.98 ± 0.02	11.52 ± 0.33	12.4	(0.31, 0.01)
J2340-00	4	2.054602(3)	...	1.39 ± 0.70	12.97 ± 0.12	12.53 ± 0.12	12.12 ± 0.13	11.2	(0.24, 0.09)
J2340-00	5	2.05469(3)	...	7.01 ± 3.21	13.03 ± 0.08	12.46 ± 0.31	12.02 ± 0.34	9.8	(0.20, 0.07)
J2340-00	6	2.054711(9)	...	1.19 ± 2.31	12.54 ± 0.67	12.64 ± 0.36	11.96 ± 0.26	27.2	(0.50, 0.11)
J2340-00	7	2.054727(5)	...	0.61 ± 0.29	13.48 ± 0.10	12.59 ± 0.37	-	7.5	-
J2340-00	8	2.05499(1)	...	9.12 ± 2.11	12.56 ± 0.07	11.96 ± 0.16	11.70 ± 0.29	9.5	(0.18, 0.10)
J2340-00	9	2.055131(4)	...	2.92 ± 0.90	12.47 ± 0.07	12.15 ± 0.08	11.72 ± 0.16	12.9	(0.29, 0.11)
J2340-00	1	1.36027	6.25	1.58 ±	12.83 ± 0.07	12.28 ± 0.07	11.96 ± 0.14	10.0	(0.20, 0.10)
J2340-00	2	1.36049	...	1.03 ±	12.68 ± 0.08	11.78 ± 0.29	-	7.4	-
J2340-00	3	1.36061	...	9.75 ±	11.74 ± 0.27	12.42 ± 0.15	11.96 ± 0.26	... ^g	(0.64, 0.22)
J2340-00	4	1.36088	...	0.64 ±	13.23 ± 0.28	12.77 ± 0.08	11.81 ± 0.21	10.9	(0.25, 0.03)

^a Instrumental FWHM

^b T_{ex}⁰¹ is the excitation temperature derived from the CI and CI* states. This should be consistent with and generally is higher than T_{CMB}.

^c f1 and f2 as defined in the text

^d (f1, f2) derived using the upper limit on N(CI**)

^e Doppler parameter determined from the curve of growth method in Jorgenson et al. (2009)

^f T_{ex} < T_{CMB}. This unphysical result is likely due to measurement error. Indeed, accounting for the given error, T_{ex} = 8 K consistent with T_{CMB} = 7.6 K.

^g N(CI*) >> N(CI) which implies T_{ex} = -50 K.

TABLE 3
OTHER RELEVANT DLA DATA

Quasar	z_{abs}	$\log N(\text{H I})$ [cm^{-2}]	$\log N(\text{C II}^*)$ [cm^{-2}]	ℓ_c [$\text{ergs s}^{-1}\text{H}^{-1}$]	$[\text{M}/\text{H}]^a$	$[\text{Fe}/\text{H}]^b$	$\log N(\text{C I}^{tot})$	$\log (\frac{\text{C II}}{\text{C I}})^c$ [cm^{-2}]	Δv [km s^{-1}]
FJ0812+32	2.066780	21.50 ± 0.20	13.62^d	-27.4^d	-1.83 ± 0.20	-2.06 ± 0.02	13.30	2.57 ± 0.20	26
...	14.42^e	-26.6^e
FJ0812+32	2.62633	21.35 ± 0.10	14.30 ± 0.01	-26.56 ± 0.10	$-0.81^f \pm 0.10$	$-1.62^g \pm 0.10$	13.63	3.10 ± 0.20	70
Q1331+17	1.77636	21.14 ± 0.08	$<13.56^h$	<-27.16	-1.37 ± 0.01	-1.97 ± 0.01	13.56	2.40 ± 0.20	72
Q2100-06	3.09237	21.05 ± 0.15	14.09 ± 0.01	-26.48 ± 0.15	-0.73 ± 0.15	-1.20 ± 0.02	13.17	3.39 ± 0.02	187
Q2231-00	2.06615	20.56 ± 0.10	13.71 ± 0.04	-26.37 ± 0.11	-0.74 ± 0.16	-1.40 ± 0.07	13.04	2.88 ± 0.20	122
J2340-00	2.05452	20.35 ± 0.15	13.84 ± 0.04	-26.03 ± 0.15	-0.74 ± 0.16	-0.92 ± 0.03	14.09	1.86 ± 0.20	104

^a Logarithmic α -metal abundance with respect to solar, determined using Si II unless otherwise labeled

^b Logarithmic Fe abundance with respect to solar

^c N(CII) calculated assuming the "minimal depletion model" from Wolfe et al. (2004) where $[\text{C}/\text{H}] = [\text{Si}/\text{H}] - 0.2$. See text for details.

^d Assume low cool DLA with average low cool ℓ_c . (The measured upper limit on $\log N(\text{C II}^*) = 14.06 \text{ cm}^{-2}$, which includes blending)

^e Assume high cool DLA with average high cool ℓ_c

^f Global metallicity based on Zn II measurement.

^g Based on Cr II instead of Fe II

^h N(CII*) as determined by fitting constrained by Si II components. Blending means that this is still technically an upper limit.

TABLE 4
CII* TECHNIQUE SOLUTIONS

Quasar	z_{abs}	$J_{\nu}^{local\ a}$ / 1×10^{-19}	J_{ν}^{Bkdd} / 1×10^{-20}
FJ0812+32	2.06678	0.43 ^b	2.56
FJ0812+32	2.06678	3.46 ^c	2.56
FJ0812+32	2.06678	36.38 ^d	2.56
FJ0812+32 ^{global}	2.62633	7.17	2.45
FJ0812+32 ^{div} _{comp1}	2.62633	19.2	2.45
FJ0812+32 ^{div} _{comp2}	2.62633	6.3	2.45
FJ0812+32 ^{div} _{comp3}	2.62633	259.9	2.45
Q1331+17	1.77636	3.09	2.53
J2100-06	3.09237	17	2.33
Q2231-00	2.06615	24.7	2.56
J2340-00	2.05452	52.4 ^e , 10.8 ^f	2.56

^a Evaluated at 1500Å; Error is approximately $\pm 50\%$

^b C II* in forest. Assumed low $\ell_c = -27.4$ and $[\text{Fe}/\text{Si}] = 0.0$, the maximal depletion model

^c C II* in forest. Assumed low $\ell_c = -27.4$ and $[\text{Fe}/\text{Si}] = -0.2$, the minimal depletion model

^d C II* in forest. Assumed high $\ell_c = -26.6$ and $[\text{Fe}/\text{Si}] = -0.2$

^e J_{ν}^{local} determined for components 3, 4, 5

^f J_{ν}^{local} determined for components 6 & 7

TABLE 5
C I TECHNIQUE SOLUTIONS

DLA, comp.	J_ν^{total} $\times 10^{-19}$	$\log(\frac{C I}{C I})$	1σ (2σ) C I constraints			$\log(P/k)$ [cm ⁻³ K]	best χ^2 fit			ℓ^a [pc]
			n(H I) [cm ⁻³]	T [K]	n(H I) [cm ⁻³]		T [K]	$\log(P/k)$ [cm ⁻³ K]		
0812+32 $z_{abs}=2.06,1(a)$	3.72 ^b	2.57±0.2	302 – 1096(302 – 1202)	32 – 50(32 – 63)	4.18 – 4.54(4.10 – 4.58)	316	50	4.20	3.2	
0812+32 $z_{abs}=2.06,1(b)$	0.69 ^c	2.77±0.2	40 – 83(35 – 91)	251 – 1000(200 – 1259)	4.26 – 4.66(4.08 – 4.80)	79	251	4.30	13.0	
0812+32 $z_{abs}=2.06,1(c)$	36.64 ^d	2.57±0.2	– (3802 – 12589)	– (20 – 25)	– (4.88 – 5.40)	12589	20	5.40	0.1	
0812+32 $z_{abs}=2.62^{global},1$	7.4 11.0 ^e	3.10±0.2 3.10±0.2	72 – 120(23 – 417) 105 – 151(46 – 602)	32 – 50(10 – 126) 25 – 32(10 – 79)	3.48 – 3.58(2.36 – 4.34) 3.52 – 3.58(2.66 – 4.38)	76	40	3.49	9.5	
0812+32 $z_{abs}=2.62^{global},3$	3.8 ^f 7.4 11.0 ^e	3.10±0.2 3.10±0.2 3.10±0.2	50 – 138(13 – 275) 87 – 398(72 – 549) 138 – 602(105 – 912)	32 – 53(10 – 200) 32 – 126(25 – 251) 25 – 79(20 – 158)	3.50 – 3.64(2.12 – 4.42) 3.74 – 4.30(3.54 – 4.80) 3.74 – 4.38(3.52 – 4.76)	100	79	3.90	7.2	
0812+32 $z_{abs}=2.62^{div},1$	19.4 29.0 ^e 9.9 ^f	3.71±0.2 3.71±0.2 3.71±0.2	14 – 57(5 – 158) 8 – 66(8 – 209) 14 – 42(2 – 105)	25 – 79(10 – 126) 10 – 32(10 – 251) 63 – 316(10 – 1259)	2.86 – 3.32(1.66 – 4.60) 1.92 – 3.12(1.92 – 4.40) 3.32 – 3.80(1.22 – 4.86)	14	50	2.86	5.9	
0812+32 $z_{abs}=2.62^{div},3$	260 390.1 ^e 130.2 ^f	3.06±0.2 3.06±0.2 3.06±0.2	1513–12020(1513–12587) 2629–12587(2187–12587) 758–6024(758–8316)	10 – 20(10 – 32) 10 – 20(10 – 32) 10 – 20(10 – 40)	4.18 – 5.38(4.18 – 5.60) 4.42 – 5.40(4.34 – 5.60) 3.88 – 5.08(3.88 – 5.42)	3161	10	4.50	0.1	
1331+17,1	3.3 4.9 ^e 1.8 ^f	2.40±0.2 2.40±0.2 2.40±0.2	– (229 – 457) – (417 – 1738) – (100 – 398)	– (16 – 20) – (13 – 16) – (16 – 32)	– (3.66 – 3.86) – (3.82 – 4.34) – (3.40 – 3.80)	331	16	3.72	1.4	
2100–06,1	17.2 25.7 ^c 8.7 ^f	3.39±0.20 3.39±0.20 3.39±0.20	22 – 525(22 – 12587) 44 – 871(44 – 12587) 24 – 347(10 – 7584)	10 – 251(10 – 10000) 10 – 158(10 – 10000) 20 – 501(10 – 10000)	2.34 – 4.78(2.34 – 8.10) 2.64 – 4.74(2.64 – 8.10) 2.88 – 4.94(2.02 – 7.88)	69	50	3.54	5.3	
2231–00,2	25.0 37.3 ^e 12.6 ^f	2.88±0.2 2.88±0.2 2.88±0.2	199 – 1513(174 – 1819) 347 – 2630(347 – 3019) 151 – 758(79 – 832)	13 – 25(10 – 32) 10 – 20(10 – 25) 16 – 40(10 – 50)	3.40 – 4.48(3.24 – 4.66) 3.54 – 4.62(3.54 – 4.78) 3.54 – 4.28(2.90 – 4.42)	363	20	3.86	0.3	
2340–00,2	0.39 ^g	1.86±0.2	48 – 240(30 – 525)	63 – 501(40 – 1585)	3.84 – 4.80(3.38 – 5.68)	66	200	4.12	1.1	
2340–00,3	"	"	–	–	–	–	–	–	–	
2340–00,4	"	"	48 – 120(33 – 316)	63 – 158(40 – 794)	3.78 – 3.98(3.42 – 5.12)	48	158	3.88	1.5	
2340–00,5	"	"	22 – 120(7 – 417)	25 – 158(10 – 1259)	3.04 – 4.00(1.82 – 5.42)	35	100	3.54	2.1	
2340–00,8	"	"	35 – 91(7 – 166)	40 – 100(10 – 316)	3.44 – 3.62(1.82 – 4.40)	35	79	3.44	2.1	
2340–00,9	"	"	48 – 138(29 – 275)	63 – 200(32 – 631)	3.82 – 4.10(3.30 – 4.98)	48	158	3.88	1.5	
2340–00,2	– ^h	2.24±0.2	–	–	–	–	–	–	–	
2340–00,3	52.7	1.74±0.2	–	–	–	–	–	–	–	
2340–00,4	52.7	1.74±0.2	–	–	–	–	–	–	–	
2340–00,5	52.7	1.74±0.2	–	–	–	–	–	–	–	
2340–00,8	11.0 14.5 ^e 5.7 ^f	2.34±0.2 2.34±0.2 2.34±0.2	– (661 – 5011) – (1318 – 7943) – (219 – 1819)	– (10 – 20) – (10 – 20) – (10 – 32)	– (3.82 – 5.0) – (4.12 – 5.10) – (3.34 – 4.56)	661	10	3.82	0.03	
2340–00,9	11 14.5 ^e 5.7 ^f	2.34±0.2 2.34±0.2 2.34±0.2	– (912 – 6606) – (1513 – 12588) – (363 – 2884)	– (13 – 40) – (13 – 40) – (16 – 63)	– (4.12 – 5.32) – (4.28 – 5.60) – (3.80 – 5.06)	912	16	4.16	0.02	

^a This estimated cloud size, $\ell = N(\text{H I})/n(\text{H I})$, is technically an upper limit.

^b The most likely model: Minimal depletion model, low ℓ_c object with $[\text{Fe}/\text{Si}] = -0.2$

^c Maximal depletion model, assuming the low cool ℓ_c with $[\text{Fe}/\text{Si}] = 0.0$

^d Minimal depletion model, assuming the high cool ℓ_c with $[\text{Fe}/\text{Si}] = -0.2$

^e Includes +50% error on J_ν^{local}

^f Includes –50% error on J_ν^{local}

^g Minimum background assumption $J_\nu \sim$ Haardt-Madau for this object

^h Solar (or super-solar) Fe/H precludes calculation.

TABLE 6
CI TECHNIQUE SOLUTIONS: FULL J_ν^{total} GRID

DLA	comp.	$\log(\frac{CII}{CI})$	$n(\text{H I})(2\sigma)$ [cm^{-3}]	$T(2\sigma)$ [K]	$\log(P/k)(2\sigma)$ [cm^{-3}K]	$J_\nu^{total} / 1 \times 10^{-19}(2\sigma)$ a	Consistent? ^b
0812+32 $z_{abs}=2.06$	1	2.57±0.2	≥36 (≥32)	20–1258 (13–1585)	4.08–5.42 (4.0–5.50)	0.41–195 (0.41–275)	yes
0812+32 $z_{abs}=2.62^{global}$	1	3.10±0.2	≥6 (≥0.1)	≤4000(-)	3.04–5.10 (0.08– 5.70)	≤773 (≤773)	yes
0812+32 $z_{abs}=2.62^{global}$	3	3.10±0.2	≥9 (≥7)	≤6300(-)	3.30–5.40 (3.10– 5.60)	≤773 (≤773)	yes
0812+32 $z_{abs}=2.62^{div}$	1	3.71±0.2	2-57(0.002-4166)	- (-)	1.72–4.68 (≤5.34)	≤34 (≤1082)	yes
0812+32 $z_{abs}=2.62^{div}$	3	3.06±0.2	≥7 (≥6)	≤7943(-)	3.40–5.40 (3.18– 5.60)	≤923 (≤923)	yes
1331+17	1	2.40 ± 0.2	11–44 (10–12021)	79–794 (≤794)	3.50–4.04 (3.20–5.08)	0.34–0.94 (0.34–86)	yes
2100–06	1	3.39±0.20	≥2 (≥0.03)	–	2.14–5.60 (-)	–	
2231–00	2	2.88±0.2	≥6 (≥3)	≤6300 (≤7950)	3.40–5.30 (2.54–5.40)	≤751 (≤751)	yes
2340–00	2	1.86±0.2	≥48 (≥30)	20–500 (16–1585)	3.82–5.50 (3.38–5.90)	≤19 (≤21)	–
2340–00	3	"	≥132 (≥110)	13–32 (13–32)	3.62–5.20 (3.54–5.20)	0.92–67 (0.44–24)	no
2340–00	4	"	48–190 (≥33)	40–158 (16–794)	3.78–3.98 (3.42–5.68)	0.39–1.1 (0.39–21)	no
2340–00	5	"	≥22 (≥7)	13–158 (≤1259)	3.04–5.20 (1.82–5.80)	0.39–23.8 (0.39–26.7)	no
2340–00	8	"	35–120 (≥7)	32–100 (≤316)	3.44–3.62 (1.82–5.30)	0.39–0.92 (0.39–26.7)	yes
2340–00	9	"	47–316 (≥29)	32–200 (13–631)	3.82–4.10 (3.30–5.60)	0.39–1.4 (0.39–23.8)	yes
2340–00	2	2.24±0.2	≥24 (≥13)	20–1995 (13–6310)	3.82–5.50 (3.38–5.90)	0.39–53(0.39–66.7)	
2340–00	3	1.74±0.2	≥132 (≥110)	13–32 (13–32)	3.62–5.20 (3.54–5.20)	0.92–67 (0.39–24)	
2340–00	4	1.74±0.2	60–190 (≥44)	40–126 (16–501)	3.78–3.94 (3.44–5.68)	≤1.1 (≤21)	
2340–00	5	1.74±0.2	≥32 (≥12)	13–126 (≤794)	3.10–5.20 (2.06–5.80)	≤23.8 (≤26.7)	
2340–00	8	2.34±0.2	34–120 (≥7)	32–100 (≤316)	3.44–3.62 (1.82–5.30)	≤9.2 (≤26.7)	
2340–00	9	2.34±0.2	48–316 (≥29)	32–200 (13–631)	3.82–4.10 (3.30–5.60)	≤1.4 (≤23.8)	

^a [ergs cm^{-2} s^{-1} Hz^{-1} sr^{-1}]

^b Is the radiation field derived via the CII* technique consistent with the range allowed by the CI data?

TABLE 7
DUST TO GAS RATIO COMPONENT ANALYSIS OF DLA 0812+32

	comp. 1 $z_{abs}=2.625890$ $b = 18.99 \pm 1.91$ [km s ⁻¹]	comp. 2 $z_{abs}=2.626310$ $b = 6.23 \pm 0.35$ [km s ⁻¹]	comp. 3 $z_{abs}=2.626491$ $b = 0.33 \pm 0.05^a$ [km s ⁻¹]	comp. 4 $z_{abs}=2.626447$ $b = 5.6 \pm 3.3$ [km s ⁻¹]
N(Cr II) [cm ⁻²]	12.91 ± 0.04	13.15 ± 0.02	≤11.71 (1σ)	12.52 ± 0.07
N(Zn II) [cm ⁻²]	12.44 ± 0.04	12.96 ± 0.02	13.00 ^b	12.32 ± 0.24
N(C II*) [cm ⁻²]	13.56 ^c ± 0.2	13.69 ± 0.01	15.14 ± 0.17	13.08 ± 0.05
N(H I) ^d [cm ⁻²]	20.41	20.93	20.97	20.29
[Zn/H]	-0.58 ± 0.04	-0.58 ± 0.02	-0.58	-0.58 ± 0.24
[Cr/H]	-1.13 ± 0.04	-1.41 ± 0.02	≤-2.89	-1.40 ± 0.07
[Cr/Zn]	-0.55 ± 0.06	-0.83 ± 0.03	≤-2.31	-0.82 ± 0.12
κ^e	0.09	0.13	0.16	0.13
log ₁₀ κ	-1.04	-0.90	-0.78	-0.90
$\frac{CII}{CI}$	3.71 ± 0.2	3.56 ± 0.2	3.06 ± 0.2	-
$\frac{CII}{I_c}$	-26.37	-26.76	-25.35	-26.73
$J_\nu^{local} / 10^{-19} f$	19.2	6.3	259.9	2.5
f_{H_2}	2.34 × 10 ⁻⁵	9.0 × 10 ⁻³	0.14	...
β ₀ [s ⁻¹]	3.53 × 10 ⁻¹¹	6.74 × 10 ⁻¹⁴	1.53 × 10 ⁻¹⁴	...
β ₁ [s ⁻¹]	5.97 × 10 ⁻¹¹	8.96 × 10 ⁻¹⁴
S_{self}	0.08	3.6 × 10 ⁻⁴	3.9 × 10 ⁻⁵	...
S_{dust}	0.98	0.91	0.88	...
S_{total}	0.08	3.3 × 10 ⁻⁴	3.41 × 10 ⁻⁵	...
T ⁰¹ _{ex} [K]	102	64	47	...
$JLW_\nu / 10^{-19} c$	0.37	0.17	0.36	...
n(H I) ^g [cm ⁻³]	21	11	37	...

^a Doppler parameter fixed to match that of CI as determined by Jorgenson et al. (2009)

^b N(Zn II) fixed by upper limit on N(O I) assuming solar relative abundances. See text for details.

^c Summed over the two components required by VPFIT, as explained in the text.

^d N(H I) scaled to trace N(Zn II)

^e Dust to gas ratio relative to Milky Way, as defined in the text.

^f [ergs cm⁻² s⁻¹ Hz⁻¹ sr⁻¹]

^g Density derived from the H₂ as explained in the text.

TABLE 8
DLA 0812+32 MOLECULAR HYDROGEN

comp	ion	z_{abs}	$\sigma_{z_{abs}}$	b [km s ⁻¹]	σ_b	log N [cm ⁻²]	σ_{logN}	T_{0-J}^a [K]	
comp 1	H2J0	2.625812	0.000011	1.03	0.11	15.03	0.15	–	
	H2J1	”	”	”	”	15.26	0.15	102 ⁺¹ ₋₁	
	H2J2	”	”	”	”	14.04	0.06	132 ⁺⁷ ₋₆	
	H2J3	”	”	”	”	13.39	0.10	150 ⁺² ₋₂	
	H2J4	”	”	”	”	<12.64	–	222 ⁺¹⁰ ₋₉	
	H2J5	”	”	”	”	12.22	0.61	257 ⁺³¹ ₋₂₅	
	total N(H ₂) = log (total N(H ₂)) = $f^b \geq$	3.01 × 10 ¹⁵ 15.48 2.69 × 10 ⁻⁶							
comp 2	H2J0	2.626326	0.000001	2.67	0.09	<18.45 ^c	–	–	
	H2J1	”	”	”	”	18.25	0.04	64 ⁺²⁴ ₋₁₄	
	H2J2	”	”	”	”	15.49	0.06	61 ⁺⁴ ₋₄	
	H2J3	”	”	”	”	14.43	0.01	83 ⁺⁵ ₋₄	
	H2J4	”	”	”	”	13.18	0.10	119 ⁺⁴ ₋₄	
	H2J5	”	”	”	”	<12.60	–	151 ⁺⁶ ₋₆	
	total N(H ₂) < log (total N(H ₂)) < $f^b \geq$	4.61 × 10 ¹⁸ 18.66 4.1 × 10 ⁻³							
comp 3, model 1 ^d	H2J0	2.626491	0.000001	0.81 ^d	–	19.79	0.03	–	
	H2J1	”	”	”	”	19.15	0.03	47 ⁺¹ ₋₁	
	H2J2	”	”	”	”	16.60	0.03	57 ⁺¹ ₋₁	
	H2J3	”	”	”	”	15.11	0.05	74 ⁺¹ ₋₁	
	H2J4	”	”	”	”	13.99	0.04	110 ⁺¹ ₋₁	
	total N(H ₂) = log (total N(H ₂)) = $f^b \geq$	7.58 × 10 ¹⁹ 19.88 0.06							
	comp 3, model 2 ^e	H2J0	2.626494	0.000001	1.19 ^e	–	19.81	0.03	–
H2J1		”	”	”	”	19.13	0.03	45 ⁺¹ ₋₁	
H2J2		”	”	”	”	16.21	0.11	52 ⁺¹ ₋₂	
H2J3		”	”	”	”	14.88	0.07	71 ⁺¹ ₋₁	
H2J4		”	”	”	”	13.97	0.04	109 ⁺¹ ₋₁	
total N(H ₂) = log (total N(H ₂)) = $f^b \geq$		7.81 × 10 ¹⁹ 19.89 0.07							

^a Excitation temperature between rotational level J and J = 0.

^b Molecular fraction f calculated using $N(\text{H I})^{total} = 21.35 \text{ cm}^{-2}$, so that these values are technically lower limits.

^c We report the 2σ upper limit because blending with the stronger J=0 line of component 3 make the formal errors large.

^d Model 1: Doppler parameter tied to that of C I. Note that the J=0 and J=1 transitions are heavily saturated and therefore the resultant log N is determined by the damping wings and is insensitive to the choice of b.

^e Model 2: Doppler parameter determined by the J=3 state.

TABLE 9
AODM COMPONENT ANALYSIS OF DLA 2340–00

Super-Component Δv_{90} C I Component	a –30–15 km s ^{–1} (1, 2)	b 15–70 km s ^{–1} (3,4,5,6,7)	c 70–120 km s ^{–1} (8,9)
N(Fe II) [cm ^{–2}]	14.55 ± 0.05	14.63 ± 0.04	14.06 ± 0.01
N(S II) [cm ^{–2}]	14.17 ± 0.01	14.73 ± 0.01	14.31 ± 0.01
N(C II*) [cm ^{–2}]	12.53 ± 0.09	13.60 ± 0.01	12.99 ± 0.04
N(H I) ^a [cm ^{–2}]	19.58	20.13	19.72
[Fe/H]	–0.47 ± 0.05	–0.95 ± 0.04	–1.10 ± 0.01
[S/H]	–0.56 ± 0.01	–0.56 ± 0.01	–0.56 ± 0.01
[Fe/Met]	0.09 ± 0.05	–0.39 ± 0.04	–0.54 ± 0.01
κ^b	–0.06	0.06	0.09
log ₁₀ κ	–	–1.21	–1.03
N(C I) ^{total}	12.96	14.01	13.00
log $\frac{CII}{CI}$	2.24	1.74	2.34
l_c	–26.56	–26.05	–26.24
$J_\nu^{local} / 10^{-19c}$	– ^d	52.4	10.8
N(Fe III)[cm ^{–2}]	<13.87 ^e	< 13.94 ^e	<13.89 ^e
Fe III/Fe II ^f	<0.21	<0.21	<0.66
N(Ar I)[cm ^{–2}]	13.31	13.83	13.65
[Ar/S] ^g	0.12	0.08	0.32
N(Ni II) [cm ^{–2}]	13.21 ± 0.02	13.50 ± 0.01	13.14 ± 0.02
[Ni/H]	–0.55 ± 0.02	–0.82 ± 0.01	–0.79 ± 0.02
[N/Met]	0.01 ± 0.02	– 0.26 ± 0.01	– 0.23 ± 0.03
κ	–0.01	0.02	0.01
log κ	–	–1.67	– 1.97

^a N(H I) scaled to trace N(S II)

^b Dust to gas ratio relative to Milky Way, defined in the text. Here we have used S II instead of Si II.

^c [ergs cm^{–2} s^{–1} Hz^{–1} sr^{–1}]

^d We did not determine J_ν^{local} for this component because the super-solar Fe II measurement.

^e AODM measurements taken as upper limits because of possible blending with the forest.

^f Fe III/Fe II ~0.3 means partially ionized, HI/H = 0.5

^g If [Ar/S] > –0.2 then x <0.1 (but low Ar/S does not require x >>0).

TABLE 10
DLA 2340–00 MOLECULAR HYDROGEN

component ^a	ion	z_{abs}	$\sigma_{z_{abs}}$	b [km s ⁻¹]	σ_b	log N [cm ⁻²]	σ_{logN}	T_{0-J}^b [K]
comp 1								
	H2J0	2.054165	0.000001	2.31	0.07	15.262	0.040	–
	H2J1	2.054165	...	2.31	0.00	15.94	0.049	266 ⁺¹⁰ ₋₉
	H2J2	2.054165	...	2.31	0.00	14.904	0.065	211 ⁺⁵ ₋₅
	H2J3	2.054165	...	2.31	0.00	14.251	0.049	191 ⁺¹ ₋₁
	H2J4	2.054165	...	2.31	0.00	<13.39	–	262 ⁺⁴ ₋₄
	H2J5	2.054165	...	2.31	0.00	<12.90	–	287 ⁺³ ₋₃
	log (total N(H ₂)) =	16.06						
	f ^c =	1.03 × 10 ⁻⁴						
comp 2								
	H2J0	2.054291	0.000001	1.25	0.09	14.657	0.073	–
	H2J1	2.054291	...	1.25	0.00	15.292	0.079	232 ⁺⁴ ₋₄
	H2J2	2.054291	...	1.25	0.00	14.478	0.079	253 ⁺² ₋₂
	H2J3	2.054291	...	1.25	0.00	14.299	0.059	265 ⁺² ₋₂
	H2J4	2.054291	...	1.25	0.00	<13.08	–	293 ⁺⁹ ₋₈
	H2J5	2.054291	...	1.25	0.00	<13.23	–	378 ⁺¹⁰ ₋₉
	log (total N(H ₂)) =	15.47						
	f ^c =	2.63 × 10 ⁻⁵						
comp 4								
	H2J0	2.054573	0.000002	4.62	0.16	17.269	0.082	–
	H2J1	2.054573	...	4.62	0.00	17.955	0.054	276 ⁺³² ₋₂₆
	H2J2	2.054573	...	4.62	0.00	17.045	0.129	241 ⁺¹³ ₋₁₂
	H2J3	2.054573	...	4.62	0.00	15.326	0.028	136 ⁺² ₋₂
	H2J4	2.054573	...	4.62	0.00	13.812	0.041	168 ⁺² ₋₂
	H2J5	2.054573	...	4.62	0.00	13.317	0.139	203 ⁺² ₋₂
	log (total N(H ₂)) =	18.08						
	f ^c =	1.06 × 10 ⁻²						
comp 6								
	H2J0	2.054714	0.000001	5.06	0.11	15.997	0.047	–
	H2J1	2.054714	...	5.06	0.00	16.825	0.065	587 ⁺⁹⁹ ₋₇₄
	H2J2	2.054714	...	5.06	0.00	16.059	0.039	349 ⁺⁵ ₋₅
	H2J3	2.054714	...	5.06	0.00	15.836	0.019	300 ⁺⁶ ₋₆
	H2J4	2.054714	...	5.06	0.00	14.355	0.015	286 ⁺³ ₋₄
	H2J5	2.054714	...	5.06	0.00	13.932	0.040	310 ⁺¹ ₋₁
	log (total N(H ₂)) =	16.98						
	f ^c =	8.51 × 10 ⁻⁴						
comp 8								
	H2J0	2.054986	0.000001	3.64	0.10	15.76	0.042	–
	H2J1	2.054986	...	3.64	0.00	16.55	0.067	475 ⁺⁹³ ₋₆₇
	H2J2	2.054986	...	3.64	0.00	15.63	0.047	271 ⁺² ₋₂
	H2J3	2.054986	...	3.64	0.00	15.13	0.027	229 ⁺² ₋₂
	H2J4	2.054986	...	3.64	0.00	13.75	0.046	251 ⁺¹ ₋₁
	H2J5	2.054986	...	3.64	0.00	11.90	3.520	207 ⁺³⁸⁰ ₋₈₁
	log (total N(H ₂)) =	16.67						
	f ^c =	4.21 × 10 ⁻⁴						
comp 9								
	H2J0	2.055135	0.000001	1.80	0.07	16.735	0.074	–
	H2J1	2.055135	...	1.80	0.00	17.200	0.057	151 ⁺⁶ ₋₅
	H2J2	2.055135	...	1.80	0.00	16.035	0.088	159 ⁺² ₋₂
	H2J3	2.055135	...	1.80	0.00	14.753	0.049	135 ⁺¹ ₋₁
	H2J4	2.055135	...	1.80	0.00	<13.10	–	162 ⁺³ ₋₃
	H2J5	2.055135	...	1.80	0.00	<13.02	–	212 ⁺³ ₋₃
	log (total N(H ₂)) =	17.35						
	f ^c =	2.00 × 10 ⁻³						

^a Excitation temperature between rotational level J and J = 0.

^b Components are numbered by the closest z CI component

^c f calculated assuming logN(HI) = 20.35

TABLE 11
H₂ COMPONENT ANALYSIS OF DLA 2340–00 – USING AODM VALUES

Super-Component component	a 1 ^a	a 2 ^a	b 4	b 6	c 8	c 9
$f_{H_2}^b$	6.04×10^{-4}	1.55×10^{-4}	1.74×10^{-2}	1.41×10^{-3}	1.79×10^{-3}	8.47×10^{-3}
T_{ex}^{01} [K]	266	232	276	587	475	151
β_0 [s ⁻¹]	9.44×10^{-11}	1.84×10^{-10}	2.43×10^{-12}	1.36×10^{-10}	6.31×10^{-11}	1.84×10^{-12}
β_1 [s ⁻¹]	1.00×10^{-10}	8.42×10^{-10}	2.52×10^{-12}	1.44×10^{-10}	2.62×10^{-12}	5.89×10^{-12}
S_{self}	2.85×10^{-2}	7.92×10^{-2}	8.72×10^{-4}	5.83×10^{-3}	9.88×10^{-3}	3.07×10^{-3}
S_{dust}	– ^a	– ^a	0.993	0.993	0.996	0.996
S_{total}	–	–	8.66×10^{-4}	5.78×10^{-3}	9.84×10^{-3}	3.06×10^{-3}
$J_{\nu}^{LW}/10^{-19c}$	–	–	2.25	18.84	5.13	< 0.48
$n(\text{H I})^d$ [cm ⁻³]	–	–	1629	10509	3595	377

^a Super-solar Fe II measurement, therefore κ was not sensible

^b f is calculated using the $N(\text{H I})$ of the Super-Component, i.e. $N(\text{H I}) = 19.58$ for (1, 2), $N(\text{H I}) = 20.13$ for (3, 4, 5, 6, 7) and $N(\text{H I}) = 19.72$ for (8, 9).

^c [ergs cm⁻² s⁻¹ Hz⁻¹ sr⁻¹]

^d Density derived from the H₂ as explained in Appendix 3.

TABLE 12
COMPARISON OF CI^a AND CII* TECHNIQUE MODELS FOR DLA 1331+17

model	$J_{\nu}^{local}/10^{-19}$ [ergs cm ⁻² s ⁻¹ Hz ⁻¹ sr ⁻¹]	T [K]	n [cm ⁻³]	log(P/k) [cm ⁻³ K]	log($\frac{CII}{CI}$)
CII*, P_{eq}^b , min ^c	3.09	80.6	6.9	2.75	3.70
CI, P_{eq} , min	3.09	16–20	229–457	3.66–3.86	2.40
CII*, P_{max} , min	1.74	22.9	17.4	2.6	3.23
CI, P_{max} , min	1.74	20–32	95–263	3.38–3.72	2.40
CII*, P_{min} , min	4.90	761.5	1.0	2.88	4.51
CI, P_{min} , min	4.90	13–16	347–1445	3.74–4.26	2.40
CII*, P_{eq} , max ^d	1.64	102.4	3.2	2.52	3.69
CI, P_{eq} , max	1.64	25–63	42–158	3.22–3.60	2.60
CII*, P_{max} , max	0.65	23.6	9.1	2.33	3.04
CI, P_{max} , max	0.65	25–63	46–158	3.26–3.60	2.60
CII*, P_{min} , max	7.34	838.8	1.1	2.97	4.62
CI, P_{min} , max	7.34	13–16	263–1096	3.62–4.14	2.60

^a CI results are all 2σ

^b $P_{eq} = (P_{min} P_{max})^{1/2}$

^c Minimal Depletion Model

^d Maximal Depletion Model